12-10-2021

Catalytic light alkanes selective conversion through ammonia-assisted reforming

Siavash Fadaeerayeni
Mississippi State University, Siavash.fadaee@gmail.com

Recommended Citation

Fadaeerayeni, Siavash, "Catalytic light alkanes selective conversion through ammonia-assisted reforming" (2021). *Theses and Dissertations*. 5339.
https://scholarsjunction.msstate.edu/td/5339

Catalytic light alkanes selective conversion through ammonia-assisted reforming

By

Siavash Fadaeerayeni

Approved by:

Yizhi Xiang (Major Professor)
Hossein Toghiani
Neeraj Rai
Xin Cui
Dong Meng (Graduate Coordinator)
Jason M. Keith (Dean, Bagley College of Engineering)

A Dissertation
Submitted to the Faculty of
Mississippi State University
in Partial Fulfillment of the Requirements
for the Degree of Doctor of Philosophy
in Chemical Engineering
in the Chemical Engineering Department

Mississippi State, Mississippi

December 2021

Name: Siavash Fadaeerayeni

Date of Degree: December 10, 2021

Institution: Mississippi State University

Major Field: Chemical Engineering

Major Professors: Yizhi Xiang

Title of Study: Catalytic light alkanes selective conversion through ammonia-assisted reforming

Pages in Study: 163

Candidate for Degree of Doctor of Philosophy

The fact that hydrogen is a clean and versatile fuel offers an attractive carbon-free source of energy and leverages the U.S. economy toward long-term sustainable economic growth. At an industrial scale, hydrogen production is mostly relying on methane steam reforming producing stoichiometric amounts of carbon oxides (CO and CO_2), which imposes economic and environmental concerns. To mitigate the issue, we propose NH_3 assisted anaerobic reforming of natural gas liquids (ethane and propane) as an alternative approach to produce CO_x free hydrogen.

Here, in the first chapter, through comprehensive performance evaluation, characterization, and transient kinetic studies, it is shown that the atomically dispersed Re-oxo grafted into framework Al of the HZSM-5 zeolite are highly active and stable for the ammonia reforming of ethane and propane at temperatures comparable to steam reforming ≤ 650 °C.

In the second chapter, an alternative non- noble Ni/Ga intermetallic compound (IMC) with various Ni to Ga ratios is synthesized through the solvothermal synthesis by forming the oxalate MOF precursor. The result indicates that while Ni-rich samples form pure Ni_3Ga IMC with promising catalytic performance, the Ga rich catalyst consists of segregated phases of Ni/Ga IMC and Ga_2O_3 with ill-defined structure showing lower stability despite the high activity.

In chapter 3, a bifunctional Ni/Ga supported ZSM-5 is successfully developed in ethane aromatization. Influence of metal function in early-stage and steady-state activity and stability as well as structure reactivity relation was investigated applying comprehensive characterization, performance test, deactivation modeling, and transient studies. The results suggest that a tandem reaction mechanism between Ni_3Ga intermetallic compound, Ga cation, and Bronsted acid sites of zeolite is responsible for the superior performance of bimetallic catalysts compared to their monometallic counterpart.

In the last chapter, applying transient kinetic technique, the mechanism of ethane aromatization over Pt and Zn supported ZSM-5 model catalysts was precisely explored. The results reveal that despite mechanistic differences between these catalysts, ethane amortization on both catalysts follows a hydrocarbon pool mechanism.

Key words: Light alkane conversion, reforming, catalysis, Carbon-free H_2 production

DEDICATION

To my god, family, mentors, and friends.

ACKNOWLEDGEMENTS

I would like to thank my supervisor, Dr. Yizhi Xiang, for his continuous support and supervision throughout my Ph.D. I am also grateful for the thoughtful comment I received from committee members. Special thanks to Dr. Hossein Toghiani, for his support to access the facilities in his lab as well as other financial and non-financial assistance. I am also thankful for the financial support by Bagley College of Engineering at Mississippi State University and NICE America Research Inc. I would to also gratefully acknowledge the TEM and XRD work (supported by the National Science Foundation (no. MRI-1126743)) at the Institute for Imaging and Analytical Technologies (I2AT) at Mississippi State University. This research used resources of the Advanced Photon Source and the Center for Nanophase Materials Sciences, the U.S. Department of Energy (DOE) Office of Science User Facilities (under contract no. DE-AC02-06CH11357) operated for the DOE Office of Science by Argonne National Laboratory and Oak Ridge National Laboratory (ORNL), respectively. Work at ORNL was partly supported by DOE, Office of Science, Office of Basic Energy Sciences, Chemical Sciences, Geosciences, and Biosciences Division, Catalysis Science program.

TABLE OF CONTENTS

CHAPTER

LIST OF TABLES

LIST OF FIGURES

CHAPTER I

INTRODUCTION

The advanced knowledge of hydraulic fracturing reshapes the US energy market from traditional oil resources to shale gas, turning the US into the most cost-effective energy producer outside the middle east. Natural Gas Liquids (NGL) including ethane and propane are the main components of natural gas after methane, standing for more than 14 vol% in some of the US shale gas fields. This huge amount of available NGL generates a new boom for research both in academia and industry, aiming at improving the current technologies or discovering novel processes for the conversion of light alkanes.

Hydrogen could be generated from a variety of sources such as natural gas, coal, renewable or nuclear sources. It could be used as fuel to generate electricity/power for fuel cells, engines, and turbines or as a chemical feedstock used in petrochemical, electronics, metal production, ammonia, and methanol synthesis, food processing, and cosmetics industries [1]. Moreover, compared to traditionally used fossil fuel, the fact that hydrogen is a carbon-free fuel and has a high energy density (120-140 MJ/kg) makes it a more attractive and environmentally benign source of fuel [2, 3].

Although it is environmentally more attractive to produce H_2 from renewable sources, it seems that H_2 production continues to rely on fossil fuel in near future. In this regard, there are mainly four processes for natural gas reforming to H_2: steam reforming, dry reforming, autothermal reforming, and partial oxidation. As will be discussed below the choice of each of these processes depend on the feed compositions, target products, and reaction conditions.

1.1 Steam Methane Reforming (SMR)

SMR is a several-step process including steam methane reforming, water gas shift reaction, and methanation (see equation 1.1-1.4) which produce H_2 with a high yield (~74%).

$$CH_4+H_2O \rightarrow CO+3H_2 \text{ (Steam Methane Reforming)} \tag{1.1}$$

$$H_2O+ CO \rightarrow CO_2+H_2 \text{ (Water Gas Shift)} \tag{1.2}$$

$$CO_2+4H_2 \rightarrow CH_4+2H_2O \text{ (Methanation)} \tag{1.3}$$

$$CO+3H_2 \rightarrow CH_4+H_2O \text{ (Methanation)} \tag{1.4}$$

Due to the high endothermic nature of these reactions and to reduce the rate of coke formation, a typical SMR reactor works at a very high temperature (700-850 °C), pressure of 3–25 bars, and steam to carbon ratio of 3.5. Non-precious metals, mainly Ni, and precious metals including Pt and Rh-based catalysts are the most efficient catalysts for this process; however, owing to the high rate of deactivation which renders low mass and heat effectiveness, Ni-based catalyst is the most widely used for this process industrially.

This process is widely considered the most efficient and developed industrial process for H_2 production. According to the US Department of Energy (DOE)'s report in 2012, over 95% of hydrogen production, being responsible for almost 1% of total energy consumption in the U.S., relied on steam reforming of methane consumption, the most abundant component of natural gas.

1.2 Dry Methane Reforming (DMR)

In the DMR process, methane reacts with CO_2 to form H_2/CO with a ratio of 1/1 (according to equation 1.5).

$$CH_4+CO_2 \rightarrow 2CO+2H_2 \text{ (DMR)} \tag{1.5}$$

Owing to the high endothermicity of reaction which favors high temperature operation at 850 °C, DMR is considered as a highly energy-intensive reaction and is ideal for the process such as Fischer- Tropsch, where a low H_2/CO ratio in the product is favored. The main drawback for DMR is high rate of coke formation and fast catalyst deactivation due to metal sintering arising from low ratio of H/C in the feed and harsh reaction conditions. Also, the process necessitates a special design of catalyst as C-H bond preferably activates on the metal site with small size while CO activation may require defect or basic sites [4]. Nonetheless, for the common active catalysts, whether non-precious (Ni, Co) or precious metal-based catalysts (Ir, Pd, Pt, Rh, and Ru), the catalytic performance depends on trad-off between activity, selectivity, and stability.

1.3 Partial Oxidation of Methane (POX):

This process is an exothermic reaction, in which methane and oxygen react in presence of a catalyst to produce syngas with H_2/CO ratio of 2 (equation 1.6).

$$CH_4+0.5O_2 \rightarrow CO+2H_2 \tag{1.6}$$

While partial oxidation is more economically effective compare to steam and dry reforming due to lower amount of required thermal energy, it is still suffering from the requirement of high purity oxygen feed and safety considerations regarding the explosive reaction of methane and oxygen.

1.4 Autothermal Methane Reforming (ATR)

This process combines steam reforming and partial oxidation by utilizing methane, H_2O, and O_2 as the feed. The main advantage of this process is the heat required for SMR could be provided through partial oxidation reaction, hence making the process more energy-efficient.

The reforming of higher alkanes such as ethane, propane, butane is also studied in the literature [5-15]. More recently, dry reforming of higher alkanes has received considerable attention as a promising system for simultaneously utilizing the natural gas compounds and mitigating the climate issues associated with CO_2 emission. Moreover, compared to CO_2 reforming of methane, ethane dry reforming is thermodynamically feasible at relatively lower temperatures (~ 600 °C).

Regarding the reaction mechanism, the key step in reforming reaction is methane activation which needs metal function. The activity of various metals for methane activation obeys the following order:

Ru~Rh>Ni>Ir>Pt>Pd>Re>Fe~Co

It is noteworthy to mention that the difference in activity of Rhodium and Nickel is not significant. This is why most of industrial catalysts are made of nickel-supported heat-resistant supports such as MgO, Al_2O_3, ZrO_2, $MgAl_2O_4$, etc. In general, reforming reaction carry out according to the following mechanism. Initially, dissociative adsorption of methane on the catalyst surface provides surface carbon and hydrogen species which subsequently reacts with adsorbed oxidative agents. This oxidative agent may be originated from an OH group (resulting from surface hydroxyl groups of support or dissociative adsorption of water in case of steam reforming), surface oxygen radical (in case of partial oxidation), or a CO_2 adsorbed group (in case of dry reforming). This later could react with surface H radicals to form CO and H_2 via a formate like intermediate

[16]. Moreover, in the presence of oxygen reach compounds such as lanthanum, cerium oxide, etc., another redox like mechanism for activation of carbon and oxygen containing intermediates may be considered, in which for each cycle, surface/ lattice oxygens frequently consume to promotes the activation of carbon species and subsequently replenish through reducing the oxidative agent. The difference in the rate of carbon consumption and transformation is responsible for the accumulation of carbon-containing species on the surface. This balance in surface-bound species depends on various factors such as acidity and structure of support, chemical nature and crystalline structure of metal as well as interaction of support and metal. In the industrial process, the most active sites of Ni catalyst are first passivated with a small amount of Sulphur containing chemicals to reduce the surface rate of methane and CO_2 dissociation, hence inhibiting the rate of coke formation and destruction of Ni through formation of nickel tetracarbonyl species [17].

Overall, regardless of type of process and alkane used, these so-called aerobic processes are suffering from intensive consumption of thermal energy (except for autothermal reforming), fast rate of deactivation due to coke formation, and a high rate of undesired CO_2 formation. These latter necessitate further application of methanation reactor and coke regenerators which impose more environmental and economic disadvantages.

1.5 Ammonia Decomposition

As an alternative approach, CO_x free hydrogen could be also obtained via ammonia decomposition reaction, a reverse route of the Haber Bosch Process known for more than 100 years (equation 1.7). NH_3 as a hydrogen carrier is preferably used over pure hydrogen since ammonia has a narrower combustion rate in the air (16-25 %) compared to hydrogen (4-75 %) and its strong smell helps with identifying leakage. Furthermore, ammonia could be liquified at low pressure (8.6 bar at 20 ° C), making its transportation relatively easy [18].

$$NH_3 \rightarrow N_2 + 3H_2 \tag{1.7}$$

Ammonia decomposition reaction goes through successive N-H bond cleavage of initially adsorbed ammonia, providing hydrogen adatoms that could recombine to form a hydrogen molecule. Finally, N_2 could be formed via combinative desorption of N adatoms. It is claimed that at high temperatures (> 580 °C) the kinetic of NH_3 decomposition depends on the type of metal active site with N-H bond cleavage being a rate-determining step in case of Rh, Ir, Pd, Pt, and Cu, while nitrogen desorption controls the reaction rate in case of CO, Ni, and Fe. However, at low temperature irrespective of metal type, this latter is a kinetically limiting step. In summary, metal-binding energy is a critical factor in catalyst design since ammonia activation requires its adsorption on the surface, while strongly adsorbed N adatoms may poison the catalyst. Interestingly, the most active and industrially used catalyst for ammonia synthesize are not necessarily the best ones for the reverse reaction (ammonia decomposition) as reaction conditions and rate-determining steps may be different. So far, it is widely accepted that the most active catalysts for ammonia decomposition are Ru-based catalysts. The relatively lower activity of Iron-based catalysts compared to Ru-based catalysts could be realized via higher strength of Fe-N bond compared to Ru-N, which favor the formation of iron nitride species and poison the catalyst. The formation of iron nitride is a reversible reaction at high temperature; however, the reverse reaction route (iron nitride decomposition to form Iron) often accompanies the metal sintering and irreversible deactivation [19]. Other active metals for NH_3 decomposition are Pt, Pd, Co, and Ni-based catalyst, though there is not a clear conclusion about the order of activation for these catalysts due to inconsistency of result in literature, most likely resulting from various selected reaction conditions. It is also suggested that surface modification of metal by alloying with a second metal may tune the surface properties towards the optimal range of N_2 adsorption energy favorable for NH_3 decomposition. The choice of support also is determining as it is found that electronically conductive material with basic surface properties such as CNT is the most efficient supports for Ru-based catalysts [20].

It is noteworthy mentioning that although ammonia decomposition provides a CO_x free method for hydrogen production, currently H_2 is mainly produced from fossil fuels (its production release more than 400 Mt CO_2 each year), though ongoing research demonstrates its sustainable production via heat waste, renewable electricity, and bio mass, etc. [18, 19].

1.6 BMA & Shawinigan Processes

To deal with the drawbacks of oxidative alkane reforming and take advantage of NH_3 as an efficient hydrogen carrier, one interesting approach is NH_3 assisted anaerobic reforming of light alkanes, providing an attractive approach for producing CO_x free hydrogen using natural gas and NH_3.

This process for the first time has been utilized by Degussa company to convert methane to HCN applying the BMA process. In the BMA process, usually, due to high thermodynamic constraint, CH_4 converts to HCN in ultrahigh temperature of 1300 °C over Pt mesh catalysts. The industrial process produces HCN with 80-85% yield in 90 – 94% conversion of the methane [7].

$$CH_4 + NH_3 \rightarrow HCN + 3H_2 \quad \Delta H_{298} = 252\ \text{kJ/mol} \tag{1.8}$$

In this process, the NH_3 /CH_4 ratio needs to be adjusted between 1.01 and 1.08 to avoid the formation of undesired carbon black [4]. In addition, although some attempt is made to decrease the rate of coke formation by adding second metal such as Cu, Ag, Au, Pd and W to reduce soot [21], this process is still suffering from a high rate of NH_3 and CH_4 decomposition to coke and N_2 as well as high investment costs, both as an inevitable result of operation at an ultrahigh temperature [4]. Despite successful industrialization of the BMA process as a promising example of nonoxidative catalytic activation of CH_4, to the best of our knowledge, there is no survey of research for the catalytic activity of Pt-based catalysts for higher alkanes (equation 1.9), likely because of fast deactivation of catalyst as a result of carburization of the higher alkanes over Pt catalyst at ultra-high operating temperatures required for the reaction. The only reported catalytic process for NH_3 assisted reforming of higher alkanes over MoO_3/Al_2O_3 catalyst is unsuccessful work of Denton and Bishop, performed almost 70 years ago.

$$C_x H_{2x+2} + xNH_3 \rightarrow xHCN + (2x+1) H_2 \quad (x>1) \tag{1.9}$$

Nonetheless, there is a successful non-catalytic industrial process for ammonia-assisted non-oxidative activation of propane called Shawinigan process (Fluohmic process) developed by Shawinigan Chemicals (a division of Gulf Oil Canada) in 1960. In this process, C_3H_8 reacts with ammonia (N/C ratio slightly > 1) to produce HCN (equation 1.10) applying a fluidized bed reactor working under the atmospheric pressure and temperature above 1500 °C [5].

$$C_3H_8 + 3NH_3 \rightarrow 3HCN + 7H_2 \qquad \Delta H_{298}=634 \text{ kJmol} \tag{1.10}$$

In this non-catalytic process, 94% of hydrocarbons and 85% of ammonia are converted to products mainly consisting of 25% HCN and 72% H_2. Due to the high electrical energy required (6.5 kWh/ kg_{HCN}), this process is only attractive for the region with a low cost of electricity available [5]. Overall, both industrial processes for ammonia-assisted alkane activation (BMA and Shawinigan) are highly energy and carbon-intensive due to the required ultra-high temperature.

More recently there is several attempts to decrease the reaction temperatures as low as 400 °C for the ammonia-assisted transformation of CH_4 to HCN over Pt and Cu-based catalysts utilizing nonthermal plasma (NTP). It is suggested that NTP generate highly energetic electrons with a typical energy of 1-10 eV, quiet enough for activating reactants NH_3 and CH_4 into their fragments, i.e. NH_x and CH_x, which could undergo C-N bond coupling over metallic catalyst. However, despite high HCN selectivity (~ 80 %) at 25-30 % conversion, the energy efficiency of the plasma system, calculated based on the ratio of energy required for the reaction over input energy, is still far from being potentially considered for industrial application [22, 23].

Regarding the reaction mechanism at thermochemical condition, despite the fact that both of BMA and Shawinigan process has been known for more than 50 years, there are few reports of mechanistic studies at the laboratory under the condition similar to the industrial reactor, likely due to the difficulty of operating at such a harsh condition and safety issues associated with HCN toxicity, which needs special design of reactor and safety instruments.

Hassenberg et al. investigate the mechanism for the reaction of NH_3 and CH_4 over polycrystalline Rh catalyst using a reactor system attached to a UHV analyzer working at a temperature between 500 -1600 K. They found that NH_3 decomposition competes with HCN formation reactions. They also suggested that at the high temperature of the HCN reactor, homogenous gas phase reactions may also be significant, whereas surface reactions may provide the initial radicals for gas phase reactions. Due to the presence of cyanide as ligands in organometallic chemistry, they initially hypothesized CN bonded to transition metals (Rh) is more likely to be a precursor for HCN formation. However, in the absence of cyanogen (C_2N_2), methylamine (CH_3NH_2), and acetonitrile (CH_3CN), and also due to negligible surface coverage of H, and N compared to C, they suggest that intermediates involving the HCN formation should be NH and C species rather than CN, or CH_3 species [24]. Schwartz et. al performed an experimental study and DFT calculation on the performance of various M^+ (M: metal) mediated C-N bond coupling in the reaction of methane and ammonia. They claim that at high temperatures, active phase of solid catalyst may resemble a cationic structure. They found that while the activation of NH_3 by M^+ is less likely thermochemically, C-N bond linkage most likely initiates with the formation of metal carbene (MCH_2^+). They also concluded that the formation of metal carbenes only could be possible upon exposure of late 5d elements (Ta, W, Os, Ir, and Pt) to methane. However, WCH_2^+ and $IrCH_2$ are also active for methane oligomerization which promotes the formation of coke. Based on their analysis, Pt is the most promising catalyst due to its ability to activate methane rather than ammonia and the affinity of NH_3 over CH_4 to attack metal carbene species ($PtCH_2^+$) [25]. Horn et al. studied the effect of contribution from gas-phase reactions for the reaction of CH_4 and NH_3 over Pt catalyst applying a molecular beam mass spectroscopy working under the condition similar to the BMA process. The results indicate the presence of gas-phase methylenimine (CH_2NH) and methyleneamine (CH_3NH_2) molecules. They suggest a reaction pathway, according to which following C-N bond linkage on the Pt surface, HCN formation could be formed via two-step dehydrogenation on the surface or accordingly upon dynamic adsorption/desorption and transformation of CH_2NH and CH_3NH_2 intermediates in the gas phase [26].

Delagrange et al. utilized Temporal Analysis of Products (TAP) through pulse injection to perform a mechanistic study of HCN synthesis from methane and ammonia over Pt catalyst at 1173 K. The results have shown that at their operating temperature ammonia decomposition is a much slower process compared to methane decomposition, for which the most stable species are carbon C*. They suggested that the HCN synthesis most likely goes through the hydrogenation of C* or CN* intermediates[27].

Gomez Diaz also did a DFT calculation to unravel the difference in the mechanism of oxidative (Andrussow) and non-oxidative (BMA-Degussa) formation of HCN over Pt (111) surface. According to their finding in the absence of oxygen, the main reaction pathways involve the formation of partially hydrogenated compounds mostly NH_2+H_xC (x=0,1) following by dehydrogenation to HCN. They also proposed dehydrogenation of $HCNH_2$ intermediate as a rate-determining step (RDS). However, in an oxygen-rich environment, a new balance on the surface may result in switching the C-N formation mechanism to combination of hydrogen lean compounds such as HC+N or C+N [28].

Grabow et. al. applied a descriptor-based approach to reveal the mechanistic study for various metal catalysts in HCN formation from ammonia and methane. In their analysis, they studied nine various C-N coupling pathways between CH_x and NH_y (x,y=0,1,2) assuming for the CH_xNH_y intermediates the stability could be ordered according to the energy of CH_x and NH_y constitutes. Based on their findings, while CO, Ir, and Ni are the most active for HCN formation, they are at the same time highly active for ammonia decomposition leading to low HCN selectivity. In contrast, Pt was the only metal showing relatively high activity for HCN at a negligible rate of N_2 formation. This is due to the ability of Pt in early coupling of NH_y species with C on the surface which inhibits the formation of N adatoms as a precursor for N_2 formation. They conclude that on

Pt, dissociative adoption of NH_3 is the rate-determining step and C-NH_2 coupling is the most dominant mechanism for C-N bond formation. This decreases the formation of N adatoms, hence decreasing the selectivity to N_2 formation. Overall, they conclude NH_3 decomposition is a rate-determining step for both HCN and N_2 formation [29].

Nonetheless, despite several reported attempts, there is still no consensus regarding the mechanism of the reaction, especially whether C-N coupling initiates by combining partially dehydrogenated surface species such as NH_x and CH_x followed by dehydrogenation or via coupling of surface C and N species followed by hydrogenation to form HCN. It seems that tackling such a problem may be limited experimentally due to the complex nature of this reaction as well as the required high temperature which minimizes the concentration of surface species and necessitate shore residence time.

In summary, considering the drawback of aerobic reforming of light alkanes and taking advantage of NH_3 as a hydrogen career compound, this dissertation aims at developing a catalytic system for ammonia-assisted reforming of light alkanes such as ethane and propane. We aim at developing supported metal and mixed metal oxides with superior activity, stability, and selectivity for production of CO_x free hydrogen at the temperature as low as 600 to 700 °C, which is comparable with steam reforming.

To this end, in the first two chapters, we discuss developing a Nobel metal-supported ZSM-5 and non-Nobel intermetallic compounds, which shows remarkable performance in ammonia-assisted light alkane formation. In the two last chapters, we discuss the conversion of ethane in absence of NH_3 (ethane aromatization) over metal-supported ZSM-5 catalysts. Specifically, in chapter 3, we develop a non-Nobel-based intermetallic compound supported ZSM-5 catalyst with promising catalytic performance. In addition, in chapter 4, applying transient kinetic studies we shed light on the ethane aromatization mechanism over metal-supported ZSM-5 catalyst.

1.7 References

1. Nazir, H., et al., *Is the H_2 economy realizable in the foreseeable future? Part I: H_2 production methods.* International Journal of Hydrogen Energy, 2020. 45(27): p. 13777-13788.

2. Abdalla, A.M., et al., *Hydrogen production, storage, transportation and key challenges with applications: A review.* Energy Conversion and Management, 2018. 165: p. 602-627.

3. Chai, W.S., et al., *A review on ammonia, ammonia-hydrogen and ammonia-methane fuels.* Renewable and Sustainable Energy Reviews, 2021. 147.

4. Wang, C., et al., *Recent advances during CH_4 dry reforming for syngas production: A mini review.* International Journal of Hydrogen Energy, 2021. 46(7): p. 5852-5874.

5. Porosoff, M.D., et al., *Identifying Different Types of Catalysts for CO_2 Reduction by Ethane through Dry Reforming and Oxidative Dehydrogenation.* Angew Chem Int Ed Engl, 2015. 54(51): p. 15501-5.

6. Yan, B., et al., *Dry Reforming of Ethane and Butane with CO_2 over PtNi/CeO_2 Bimetallic Catalysts.* ACS Catalysis, 2016: p. 7283-7292.

7. Xie, Z., et al., *Effects of oxide supports on the CO_2 reforming of ethane over Pt-Ni bimetallic catalysts.* Applied Catalysis B: Environmental, 2019. 245: p. 376-388.

8. Kokka, A., et al., *Hydrogen production via steam reforming of propane over supported metal catalysts.* International Journal of Hydrogen Energy, 2020. 45(29): p. 14849-14866.

9. Song, Y., Y. He, and S. Laursen, *Controlling Selectivity and Stability in the Hydrocarbon Wet-Reforming Reaction Using Well-Defined Ni + Ga Intermetallic Compound Catalysts.* ACS Catalysis, 2020. 10(16): p. 8968-8980.

10. Keshavarz, A.R. and M. Soleimani, *Nano-sized Ni/$(CaO)_x$-(Al_2O_3) y catalysts for steam pre-reforming of ethane and propane in natural gas: The role of CaO/Al_2O_3 ratio to enhance conversion efficiency and resistance to coke formation.* Journal of Natural Gas Science and Engineering, 2017. 45: p. 1-10.

11. Karthikeyan, D., et al., *Effect of preparation methods on structure and catalytic activity of Ni loaded $Ce_x Zr_1{-}x O_2$ catalysts for hydrogen production via autothermal reforming of ethane.* Research on Chemical Intermediates, 2016. 43(5): p. 2817-2837.

12. Huang, X. and R. Reimert, *Kinetics of steam reforming of ethane on Ni/YSZ (yttria-stabilised zirconia) catalyst.* Fuel, 2013. 106: p. 380-387.

13. Graf, P.O., et al., *Comparative study of steam reforming of methane, ethane, and ethylene on Pt, Rh, and Pd supported on yttrium-stabilized zirconia.* Applied Catalysis A: General, 2007. 332(2): p. 310-317.

14. Olafsen, A., et al., *Light alkanes CO_2 reforming to synthesis gas over Ni-based catalysts.* Catalysis Today, 2006. 115(1-4): p. 179-185.

15. X. Wang, R.J.G., *A study of steam reforming of hydrocarbon fuels on Pd/ceria.* Applied Catalysis A: General, 2002. 224: p. 209-218.

16. Zhang, S., et al., *$Ni_xAl_1O_2$-δ mesoporous catalysts for dry reforming of methane: The special role of NiAl2O4 spinel phase and its reaction mechanism.* Applied Catalysis B: Environmental, 2021. 291.

17. Soloviev, S.O., I.V. Gubareni, and S.M. Orlyk, *Oxidative Reforming of Methane on Structured Nickel–Alumina Catalysts: a Review.* Theoretical and Experimental Chemistry, 2018. 54(5): p. 293-315.

18. Lucentini, I., et al., *Review of the Decomposition of Ammonia to Generate Hydrogen.* Industrial & Engineering Chemistry Research, 2021.

19. Bell, T.E. and L. Torrente-Murciano, *H_2 Production via Ammonia Decomposition Using Non-Noble Metal Catalysts: A Review.* Topics in Catalysis, 2016. 59(15-16): p. 1438-1457.

20. Lamb, K.E., M.D. Dolan, and D.F. Kennedy, *Ammonia for hydrogen storage; A review of catalytic ammonia decomposition and hydrogen separation and purification.* International Journal of Hydrogen Energy, 2019. 44(7): p. 3580-3593.

21. O. Roelen, C.V.m.b.H., (Oberhausen-Holten), DE 849548, 1938.

22. Guo, Z., et al., *Pt/TS-1 Catalyst Promoted C–N Coupling Reaction in CH_4–NH_3 Plasma for HCN Synthesis at Low Temperature.* ACS Catalysis, 2018. 8(11): p. 10219-10224.

23. Yanhui Yi, ⊥ Xin Wang,⊥ Amin Jafarzadeh,⊥ Li Wang, Pei Liu, Bowen He, Jinhui Yan, Rui Zhang, Hantian Zhang, Xi Liu, Hongchen Guo, Erik C. Neyts, and Annemie Bogaerts, *Plasma-Catalytic Ammonia Reforming of Methane over Cu-Based Catalysts for the Production of HCN and H_2 at Reduced Temperatur.* ACS Catal., 2021. 11: p. 1765-1773.

24. HASENBERG, D. and L.D. SCHMIDT, *HCN Synthesis from CH_4 and NH_3 on Clean Rhl.* JOURNAL OF CATALYSIS, 1985. 91: p. 116-131.

25. Diefenbach, M., *HCN Synthesis from Methane and Ammonia: Mechanisms of Pt^+-Mediated C-N Coupling.* J. AM. CHEM. SOC., 1999. 121: p. 10614-10625.

26. Horn, R., et al., *Gas phase contributions to the catalytic formation of HCN from $CH_4$and NH_3over Pt: An in situ study by molecular beam mass spectrometry with threshold ionization.* Phys. Chem. Chem. Phys., 2004. 6(18): p. 4514-4521.

27. Delagrange, S. and Y. Schuurman, *HCN synthesis from methane and ammonia over platinum.* Catalysis Today, 2007. 121(3-4): p. 204-209.

28. Gómez-Díaz, J. and N. López, *Mechanistic Switch between Oxidative (Andrussow) and Nonoxidative (Degussa) Formation of HCN on Pt(111) by Density Functional Theory*. The Journal of Physical Chemistry C, 2011. 115(13): p. 5667-5674.

29. Grabow, L.C., et al., *Descriptor-based analysis applied to HCN synthesis from* NH_3 *and CH4.* Angew Chem Int Ed Engl, 2011. 50(20): p. 4601-5.

CHAPTER II

AMMONIA ASSISTED LIGHT ALKANE ANTI-COKE REFORMING ON ISOLATED RE OXO IN ZEOLITE

This chapter is adapted from a recently submitted article to ACS Catalysis journal: Siavash Fadaeerayeni, Erik Sarnello, Zhenghong Bao, Xiao Jiang, Raymond R. Unocic, Lingzhe Fang, Zili Wu, Tao Li, Yizhi Xiang, Ammonia assisted light alkanes anti-coke reforming on isolated Re oxo in zeolites, 2021(under revision).

2.1 Introduction

Hydrogen is a clean energy carrier[1]. It is expected to play a pivotal role in a clean, secure, and affordable energy future and is currently enjoying unprecedented political and business momentum worldwide. Although hydrogen can be produced from diverse resources based on renewable energy, it still relies on fossil hydrocarbons presently and in the near term [2]. Hydrogen from the steam reforming of hydrocarbons produces stoichiometric amounts of carbon oxides (CO and CO_2), which imposes additional costs for CO transformation and CO_2 sequestration. Carbon monoxide from the steam reforming was converted into CO_2 and H_2 through two-stage water-gas-shift reactions. A methanation reactor was used to remove the residue CO when ultra-high purity hydrogen is needed for the polymer electrolyte membrane fuel cells (PEMFCs). Therefore, the low-cost production of CO_x free hydrogen from hydrocarbon resource is critical for fuel cell applications in the near-term.

Alternatively, CO_x free H_2 can be produced from NH_3 decomposition [3]. Ammonia (vapor pressure ~0.86 MPa), from renewable energy through electrosynthesis [4] or animal waste via anaerobic digestion, [5] has been considered as a dispatchable carbon-free hydrogen carrier [6]. To mitigate the carbon oxide challenges during the conventional steam reforming and takes the advantage of NH_3 as the H_2 carrier, here, we proposed NH_3 assisted anaerobic reforming of natural gas liquids (ethane and propane) as a near-term path for onsite/distributed CO_x free H_2 production (Eqs. 2.1 and 2.2, see Fig. 2.1 for the thermodynamics). Noteworthily, ethane and propane (vapor pressure ~3.8 and 0.85 MPa) are the most abundant (~2 billion barrels/yr) hydrocarbons available besides methane. They contain 18.2-20 wt% of hydrogen and can be transported in liquid form like NH_3. The ammonia reforming of light alkanes co-produces stoichiometric amounts of HCN, which can be easily separated from H_2 through adsorption using the existing industrial technology employed by the Andrussow process, [7] and can be converted through hydrolysis for NH_3 recycling and co-produce CO (Eq. 2.3) [8-10] or HCOOH (Eq. 2.4) [11-12]. Additionally, hydrogen cyanide and metal cyanides are value-added chemicals that have been widely used in gold mining, metals hardening, electroplating, as well as the chemical syntheses of adiponitrile, methyl methacrylate, and cyanuric chloride, etc.[13]. The current market size of HCN is up to \$2.46 billion and is expected to grow with a CAGR of 1.8% from 2021 to 2025.

$$C_2H_6 + 2\ NH_3 \rightarrow 2\ HCN + 5\ H_2 \qquad \Delta H = 89.4\ kJ/mol_{H2} \tag{2.1}$$

$$C_3H_8 + 3\ NH_3 \rightarrow 3\ HCN + 7\ H_2 \qquad \Delta H = 94.8\ kJ/mol_{H2} \tag{2.2}$$

$$HCN + H_2O \rightarrow NH_3 + CO \qquad \Delta H = -5.8\ kJ/mol \tag{2.3}$$

$$NaCN + 2H_2O \rightarrow HCOONa + NH_3 \qquad \Delta H = -49.3\ kJ/mol \tag{2.4}$$

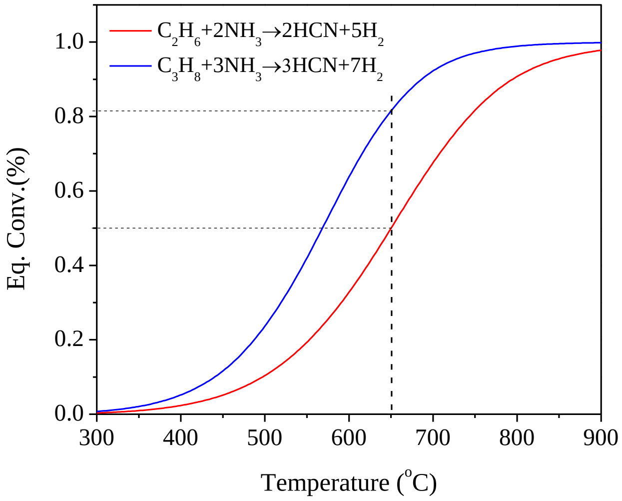

Figure 2.1 Thermodynamic analysis of ethane and propane ammonia reforming

calculated with HSC Chemistry 6.0). The equilibrium conversion was calculated based on the reaction stoichiometric shown in the figure under atmospheric pressure.

While the ammonia reforming of light alkanes is well known for industrial HCN production, reactivity remains the key challenge in contrast to conventional steam reforming in terms of H_2 production. For example, the ammonia/methane reforming, known as Bläusaure aus Methan und Ammoniak (BMA) process, was performed over the platinum catalyst at temperatures ≥1200 ºC [14]. Additionally, the ammonia reforming of C_{3+} alkanes (propane and iso-/n-butane) based on the BMA process requires a stoichiometric amount of H_2 co-feed (for C-C cleavage through hydrogenolysis) according to the early patent filed by Degussa Aktiengesellschaft.15 Besides the catalytic driven BMA process, the ammonia/propane reforming (or thermal cracking) can also be realized through the noncatalytic Shawinigan process, [13] which requires even higher temperatures of ≥1500 ºC. Despite the successful industrial application of the BMA and Shawinigan processes for HCN production, they are carbon- and energy-intensive, and the heat supply to control the high reaction temperature for such highly endothermic processes is difficult, making them unattractive to the industry [16]. To the best of our knowledge, the ammonia reforming of light alkanes at relatively low temperatures based on thermocatalysis has not been fully realized according to the only attempt made by Denton and Bishop about 70 years ago [17]. Although plasma-catalytic ammonia reforming of methane can be realized at 400 ºC over Cu/silicalite-1 catalyst, the energy efficiency is only around 6% [18]. Here, we show that the atomically dispersed Re-oxo grafted into AlO_4^- of the HZSM-5 zeolite are highly active and coke resistant for the thermocatalytic ammonia reforming of ethane and propane at the relevant temperatures (≤ 650 °C) as the conventional steam/dry reforming.

2.2 Experimental

2.2.1 Catalyst Preparation

The NH_4-ZSM-5 zeolite (specific area 400 m^2/g, $SiO_2/Al_2O_3 = 80$) was purchased from Alfa Aesar and converted to H-form by calcination at 550 °C for 4 h under the flow of air. Re supported HZSM-5 catalysts are prepared using impregnation method. For the samples with a Re concentration lower than 82 μmol/g, incipient wetness impregnation was used. In a typical synthesis procedure, according to the target concentration, weighted grams of ammonium perrhenate (NH_4ReO_4, > 99% purity, Sigma-Aldrich) was dissolved in DI water to make a solution necessary to fill the pore volume of HZSM-5 support and then was added to the support, dropwise. In the case of the samples with higher Re concentrations, the catalysts were prepared by wet impregnation. Typically, an appropriate amount of ammonium perrhenate was dissolved in DI water to make a solution equal to 5 times of support's pore volume. Then the precursor solution was added to HZSM-5 support and the resulting slurry was evaporated under the vacuum using a rotary evaporator. The as-prepared samples were dried at 70 °C overnight. The obtained NH_4ReO_4/HZSM-5 samples were activated through solid-state ion exchange under 20 % O_2 in Ar at 500 °C for 10 h. The activated sample ($[ReO_3]^+\cdot[ZSM\text{-}5]^-$) is very sensitive to moisture and should be kept in a desiccator.

In the case of supported silica samples, the synthesis procedure was the same as H-ZSM-5 supported catalysts, except we used silica (Davisil Grade 636) as the support. For 2% Ni supported HZSM-5 (SiO_2/Al_2O_3 = 80) catalyst, the sample was synthesized by incipient wetness impregnation using Nickel (II) nitrate hexahydrate ($Ni(NO_3)_2\cdot 6H_2O$, > 98.5%, Sigma-Aldrich) precursor and according to the same procedure as described for the Re sample.

Silica sand (used as a dilutant for the catalytic test) was purchased from Sigma-Aldrich and pretreated according to the following procedure. First, 40 g of silica sand was soaked in 100 ml of Nitric Acid solution (HNO_3, 70%, Sigma-Aldrich) overnight. Then, the acid solution was removed, and silica sand was washed with distilled water 3 times, followed by drying at 120 °C overnight and calcination at 650 °C for 5 h.

2.2.2 Catalytic Performance Evaluation

The catalytic performance of the prepared samples was evaluated in a home-built set-up connected to an online Agilent 5973 mass spectrometer (MS). For each test, the desired amount of catalyst (mixed with 1 g silica sand) was loaded into a quartz reactor with a volume of 2 ml (i.d., $\Phi = 1/2''$). Before catalytic testing, the sample was pretreated in Ar (40 ml/min) at 650 °C (ramp rate: 10 °C/min) 1 h. Then the spectra of Ar and the feed (by-pass) consisting of C_2H_6 (10 ml/min), Ar (10 ml/min), and NH_3 (20 ml/min) were collected for mass spectrometer calibration and used as a reference for the calculation of catalytic performance. The reactions were performed at 650°C under atmospheric pressure at a gas hourly space velocity (GHSV) of 6600 to 133000 h^{-1}. The reactor effluent was measured by an online Agilent 5973 mass spectrometer (equipped with MS Sensor 2.0 software, Diablo Analytical, Inc.).

Selected samples after the reaction were characterized by temperature-Programed Oxidation (TPO) to quantify the amounts of coke deposition. The TPO was performed in-situ in the same reactor by increasing the reactor temperature from 50-650 °C (ramp rate: 10 °C/min) in 20% O_2 in Ar (40 ml/min). The molar specific outlet flow of CO_2 during the TPO was quantified based on the calibration of MS using a mixture of 2.5 % CO_2 in Ar.

2.2.3 Chemical Transient Kinetics

The chemical transient kinetics experiment was performed at 600 °C over 200 mg Re/HZSM-5 (Re/Al = 0.2) catalyst. In addition to the reactants mixture mentioned above (C_2H_6 (10 ml/min), Ar (10 ml/min), and NH_3 (20 ml/min)), 3 ml/min Ne was used as an external standard to precisely measure the changes of the volumetric flow rate due to the reaction. The early-stage transient was realized through abruptly switching of the influent gas from inert (Ar at 40 ml/min) to C_2H_6/NH_3/Ar (10/20/10 ml/min). The back-transient was obtained by switching the influent gas from C_2H_6/NH_3/Ar back to inert (Ar). The spectra of outlet gas during the transient experiments were collected continuously (every 1 second) with the same online Agilent 5973 mass Spectrometer and quantified using the method described below.

2.2.4 Quantification with Mass Spectrometer

To do quantitative analysis for each component**,** different mass to charge ratios, such as m/z = 16, m/z = 17, m/z = 18, m/z = 20, m/z = 26, m/z = 27, m/z = 28, m/z = 30, m/z = 40, m/z = 41, m/z = 44, m/z = 78, m/z =92 and m/z = 106, were recorded online. The measured m/z signal ($I_{m/z}$) for I_{17}, I_{18}, I_{30}, I_{40}, I_{41}, I_{44}, I_{78}, I_{92}, and I_{106} can be assigned to ammonia, water, ethane, argon, acetonitrile, carbon dioxide, benzene, toluene, and xylene, respectively. In the case of nitrogen, methane, neon, ethylene, and hydrogen cyanide, the calculation is somehow more complicated as there is a contribution from other signals. In the case of I_{CH4}, I_{N2}, and I_{Ne}, the deconvoluted signals were calculated after subtracting the contribution from NH_3 to m/z = 16, C_2H_6 to m/z = 28, and Ar to m/z = 20 using the bypass signals. Finally, the I_{C2H4} and I_{HCN} were obtained via deconvolution of C_2H_4, HCN, and C_2H_6 signals using matrix.

The partial pressure of each component was calculated based on deconvoluted m/z signal ($I_{m/z}$) using an external calibration. Finally, mole flowrate (mol/s) could be obtained from the ideal gas equation ($\mathrm{P_i v_{tot} = F_i RT}$), where P_i is the partial pressure of selected molecules (Pa), v_{tot} is the total volumetric flow rate (ml/min), F_i is the mole flow rate (mol/min), R is the molar gas constant (J/mol/K), and T is the temperature (K). The molar flow of H_2 was calculated from its co-products, N_2, CH_3CN, and HCN, based on the reaction stoichiometric coefficient.

Mass (r_i) and mole (R_i) specific activity of different products were calculated based on:

$$r_i = \frac{F_i}{m_{Cat}} \tag{2.5}$$

$$R_i = \frac{r_i}{C_{Re}} \tag{2.6}$$

where m_{cat}, F_i, and C_{Re} are the mass of catalyst, the flow rate of species i, and Re concentration in the catalyst.

The carbon-based selectivity of each product was calculated based on:

$$\mathrm{S_i} = \frac{\mathrm{F_{i,\ out}} \times n}{\left(\mathrm{F_{ethane,\ in}} - \mathrm{F_{ethane,\ out}}\right) \times 2} \times 100\% \tag{2.7}$$

where the n represents the carbon number in the molecular of the product i. The reliability of the calibration and calculation was indicated by the small deviation of the total carbon balance.

$$\Delta \mathrm{C} = \left| \frac{\sum C_{in} - \sum C_{out}}{\sum C_{in}} \right| \leq 5\% \tag{2.8}$$

2.2.5 Catalyst Characterization

X-ray Absorption Spectroscopy (XAS): The X-ray absorption near edge structure (XANES) and extended X-ray absorption fine structure (EXAFS) measurements were recorded at beamline 12-BM-B in Advanced Photon Source at Argonne National Laboratory. Data were acquired in fluorescence mode using a 13-element germanium detector set at 90º angle from the incoming beam; the sample was set at a 45º angle to the incoming beam and detector. Powder samples were pressed to a disk and sealed in Kapton® tape before being attached to the sample stage. Spectra were recorded at the Re L_I (12527 eV) and L_{III} (10535 eV) edges. The XAS data were normalized and analyzed by Athena software.

Raman: Raman spectroscopy of samples was performed at Oak Ridge National Laboratory using a multiwavelength Raman system. A 325 nm laser was used as the excitation beam and scattered spectra were recorded at room temperature using a customized ellipsoidal mirror equipped with a fiber optics bundle to direct the scattering to the spectrograph stage of a triple Raman spectrometer (Princeton Instruments Acton Trivista 555). To remove the laser irradiation, an edge filter (Semrock) was utilized in front of the UV-vis fiber optic bundle (Princeton Instruments). The ultimate signals were collected using a UV-enhanced liquid N_2-cooled CCD detector (Princeton Instrument).

Inductive Couple Plasma (ICP): Actual Re loading was measured using an inductively coupled plasma mass spectrophotometer (ICP-MS), Perkin Elmer SCIEX -ELAN DRC II. Typically, the sample was first dissolved in 1 mL hydrofluoric acid (HF, 48%, Sigma Aldrich) and the solution was soaked with 2 ml of distilled water. Then, 1 ml of perchloric acid ($HCLO_4$, 70%, Sigma Aldrich) was added to the Teflon beakers and heated to 80 °C till the solution starts to smoke. Finally, hydrochloric acid (HCL, 37%, Sigma Aldrich) was added to the solution dropwise till the residue was completely dissolved. The resulting solution was diluted with DI water in a scaled beaker to make the target concentration.

Transmission Electron Microscopy (TEM): Transmission electron microscopy (TEM) images and STEM-EDX chemical mapping of the activated catalysts were obtained using a JEOL 2100TEM (operating at 200 kV). A portion of the high-angle annular dark-field STEM imaging and EDX was performed using a JEOL NeoARM operating at 200 kV.

Hydrogen Temperature-Programmed Reduction (H_2-TPR): H_2-TPR was recorded in the aforementioned home-built set-up and H_2O (m/z = 18) signal was monitored using the same online Agilent 5973 mass spectrometer. Specifically, the sample was first pretreated at 500 °C (ramp rate: 10 °C/min) for 1 h under the flow of 20% O_2 in Ar (40 ml/min) to remove the moisture. Finally, the H_2-TPR was performed by increasing the temperature of the samples from 200 - 750 °C (ramp rate: 10 °C/min) under 10% H_2 in Ar (40 ml/min). The H_2-TPR of CuO was also performed to calibrate the intensity of H_2O on the MS, which was used to quantify the reducibility of the ReOx during the H_2-TPR and transient kinetics.

2.3 Results

2.3.1 Catalyst Screening

To develop an active, selective, and stable catalyst, first, we would like to discuss the catalytic performance of various metal-supported ZSM-5 catalysts in ammonia-assisted ethane reforming which has been studied in our group.

The thermodynamic equilibrium curve of competing reactions (equation 2.9-12) is shown in fig. 2.2. As it is obvious from this figure in the temperature range of 500-600 °C, dehydrogenation and acetonitrile formation reaction pathways are more thermodynamically favorable compared to HCN formation. At higher temperatures (600-700 °C), HCN formation is thermodynamically competing with dehydrogenation and CH_3CN formation. However, within the entire temperature range, hydrogenation is thermodynamically much more favorable than HCN, C_2H_4, and CH_3CN formation. Therefore, it is important to design a catalyst that kinetically inhibits the undesired hydrogenolysis reaction. It is also noteworthy to mention that although reaction R2 and R3 also produce H_2 and value-added by-products of C_2H_4 and CH_3CN, in terms of H_2 production rate, the R1 reaction is more desired as it produced a higher amount of stochiometric H_2 (5 moles H_2/ mol C_2H_6 consumed) compared to two other reactions.

$$\text{R1: } C_2H_6+2NH_3 \rightarrow 2HCN+5H_2 \tag{2.9}$$

$$\text{R2: } C_2H_6+NH_3 \rightarrow CH_3CN+3H_2 \tag{2.10}$$

$$\text{R3: } C_2H_6 \rightarrow C_2H_4+H_2 \tag{2.11}$$

$$\text{R4: } C_2H_6+H_2 \rightarrow 2CH_4 \tag{2.12}$$

$$\text{R5: } 2NH_3 \rightarrow 3H_2+N_2 \tag{2.13}$$

Catalytic performance of various metal-supported metal catalysts in ethane ammonia reforming is shown in fig. 2.3. From this data, it is obvious that Pt, Ni, and Re are the most active catalysts for HCN formation. However, despite its high activity in C-N bond linkage, Pt is also highly active for hydrogenolysis and CH_4 formation (R4). On the other hand, Ni sample has shown fast deactivation with time on stream compared to Re supported catalyst showing considerable stability. Therefore, Re was adopted as the most promising metal for this reaction.

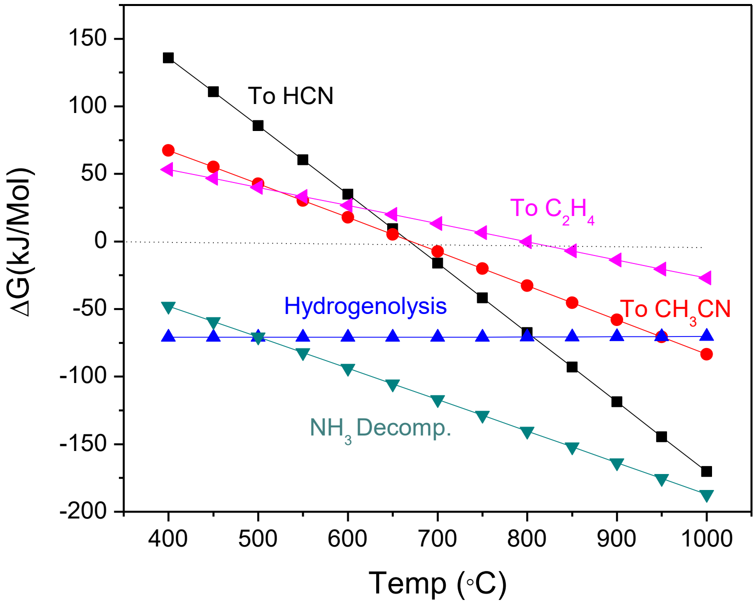

Figure 2.2 Thermodynamic equilibrium curves of competing reactions (R1-R5) in ammonia assisted reforming of ethane.

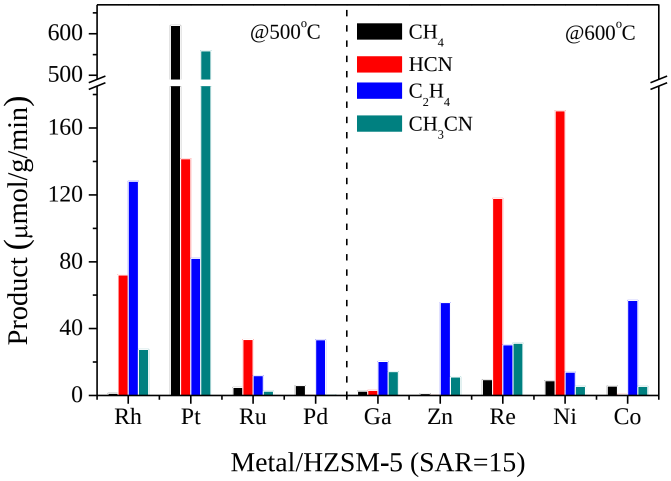

Figure 2.3 Summary of performance test for various metal-supported ZSM-5 catalysts.

We further investigate the effect of various supports rather than ZSM-5 in the catalyst performance of this reaction. Three Re catalyst supported on ZSM-5, Al_2O_3, and SiO_2 was tested for ammonia assisted ethane reforming. the results have shown in fig. 2.4. As it could be seen, while Re supported ZSM-5 and Al_2O_3catalysts show comparable selectivity for HCN formation (78-83%); in the case of silica supported catalyst the selectivity to HCN decreases to 63% in the expense of an increase in C_2H_4 selectivity. Nonetheless, despite high selectivity for C-N linkage for all these support (>70%), in terms of activity and long-term stability supported ZSM-5 catalyst outperforms two other supports. This might be due to the formation of the more stable Re species on ZSM-5 support compared to other supports.

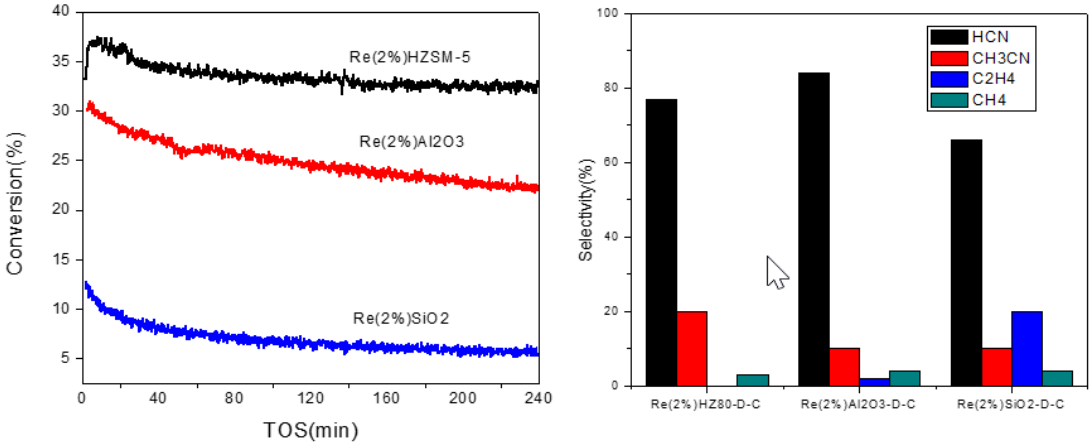

Figure 2.4 Catalytic performance of Re (2 wt%) supported ZSM-5, Al_2O_3, and SiO_2 in NH_3 ethane reforming

So far, we choose Re as the active metal and ZSM-5 as the optimum support for this reaction. Next, we will discuss the optimum acidity for the ZSM-5 support. In this regard, performance of Re supported ZSM-5 with three acidity or Si/Al_2 ratios (SAR) including 30, 80, and 280 was tested in NH_3 assisted ethane reforming. The results are shown in fig. 2.5 indicates that within the entire range of SAR studied here, the catalyst with a Si/Al ratio of 80 shows superior performance for HCN formation at comparable stability. A possible explanation could be the presence of different Re sites in ZSM-5 with various acidities. It is suggested that while for ZSM-5 with moderate/low acidity, presence of mono Re site is favorable with increasing the support's acidity there is more likely to form Re dimeric sites due to the high proximity of H protons (as the anchoring site for Re) in high acidic supports (see fig. 2.6.). On the other hand, we anticipate that the difference in the strength of Bronsted acid sites in supports with different SAR may be responsible for lower activity of ZSM-5 with low acidity (SAR= 280) compared to the optimum one (SAR=80). However, to prove the accuracy of this hypothesis, further characterization is required.

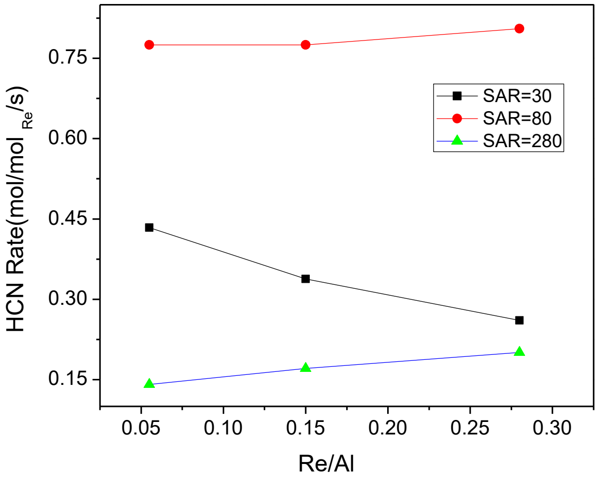

Figure 2.5 Effect of ZSM-5 acidity in Re supported ZSM-5 catalyst for NH_3 assisted ethane reforming.

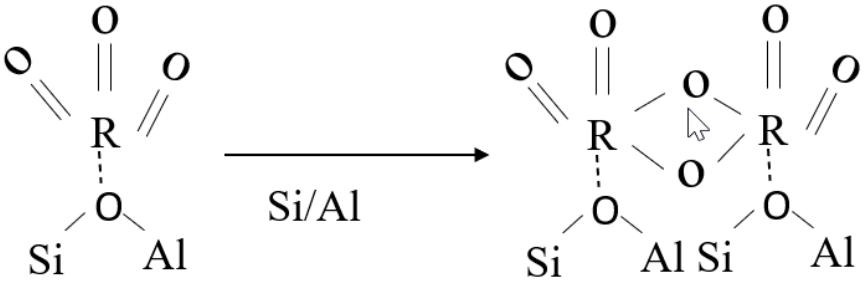

Figure 2.6 Change in the nature of Re species with increasing the ZSM-5 acidity

Another important factor that significantly affects the catalytic performance is the effect of the activation environment. As it is shown in figure 2.7, starting from NH_4ReO_4 as the rhenium precursor, its thermal activation under different environments results in the formation of various active sites. In a reductive environment, we end up getting metallic Re species evidenced with the greyish color of the activated sample as well as releasing NH_3 and H_2O, while in an inert atmosphere this NH_4ReO_4 species converts to blackish ReO_2 and forms by-products of N_2 and H_2O. Interestingly under the thermal heating in oxidative condition, NH_4ReO_4 first transforms to Re_2O_7 at temperatures above 300 °C. Re_2O_7 is a volatile compound and with further increasing the temperature evaporates and exchanges with Bronsted acid sites of zeolites to form Re oxo single site. The results of the performance test for Re (2 wt%) supported ZSM-5 (SAR=80) in the various atmosphere has shown that sample activated in O_2 has higher activity for HCN and H_2 formation compared to those prepared in a reductive and inert atmosphere. Therefore, for the rest of this chapter, we continue to reveal the structure reactivity relation for Re supported ZSM-5 catalyst with SAR of 80 activated under the oxidative condition.

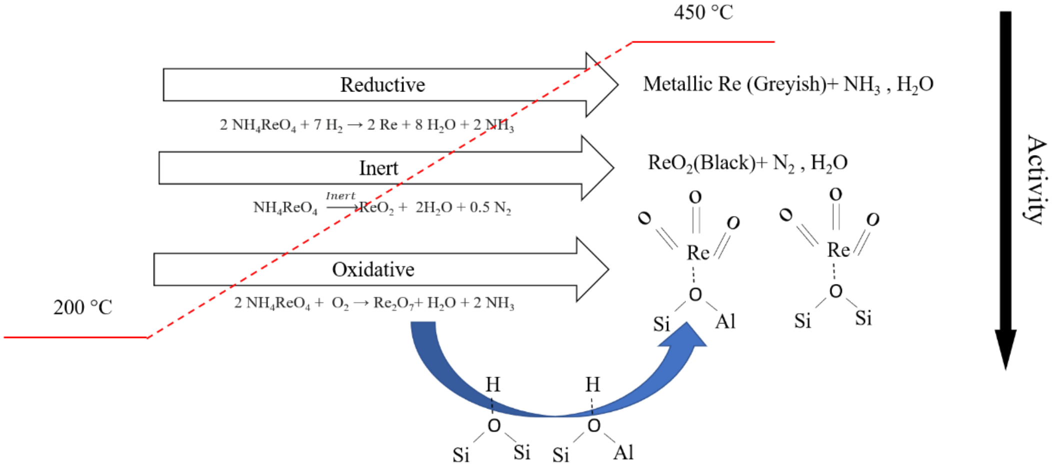

Figure 2.7 Change in the Re structure under the heating at different atmosphere

2.3.2 Catalytic Performance

The catalytic tests were performed at 650 ºC (the catalyst is active at temperatures ≥ 550 ºC, as it is shown in Fig. 2.8) with a partial pressure ratio of C_2H_6:NH_3:Ar = 0.25:0.5:0.25 atm. The catalytic data in Fig. 2.9 and 2.10 show the influence of Re loading on the ammonia/ethane reforming over the Re/HZSM-5 catalyst. Fig. 2.9 shows the mass-specific activities of the primary products (H_2, HCN, and N_2), side-product (CH_3CN), and by-product (CH_4). The activities of H_2, HCN, and N_2 increase linearly with increasing Re concentration (see Table 2.1) from 0 to 186 $\mu mol_{Re}/g_{cat}$. A further increase of the Re concentration to 329 $\mu mol_{Re}/g_{cat}$ increases the mass-specific activity of H_2 up to 55 mmol/g_{cat}/min. However, the activities deviate negatively from the linear relation for the catalysts with lower Re concentration. The strict linear dependence of the activities on the Re concentration strongly suggests that only one type of active site was formed for the catalysts with low Re loadings. Additionally, the intercept of such linear relations is approximately zero, suggesting that the active site is related to the Re species and independent of the Brønsted acidity. Nonetheless, different types of Re sites were formed at higher loading (vide infra), which resulted in the negative deviation of the activities from the original linear relationships.

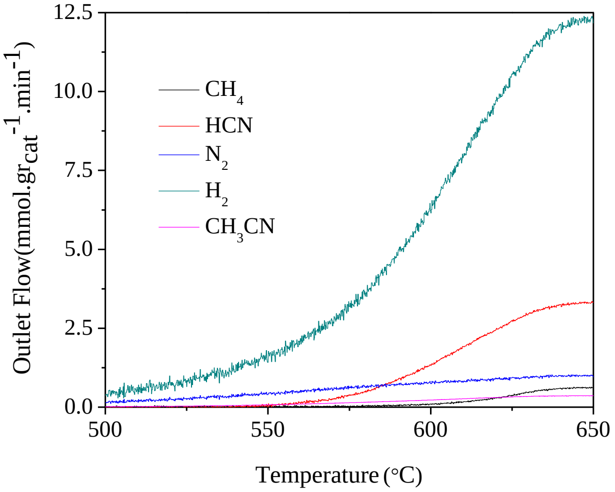

Figure 2.8 Temperature programmed surface reaction (TPSR) of ammonia ethane reforming over Re/HZSM-5 (Re/Al_f = 0.8).

The reaction conditions: partial pressure ratio of C_2H_6:NH_3:Ar = 0.25:0.5:0.25 atm, GHSV = 13300 h^{-1}.

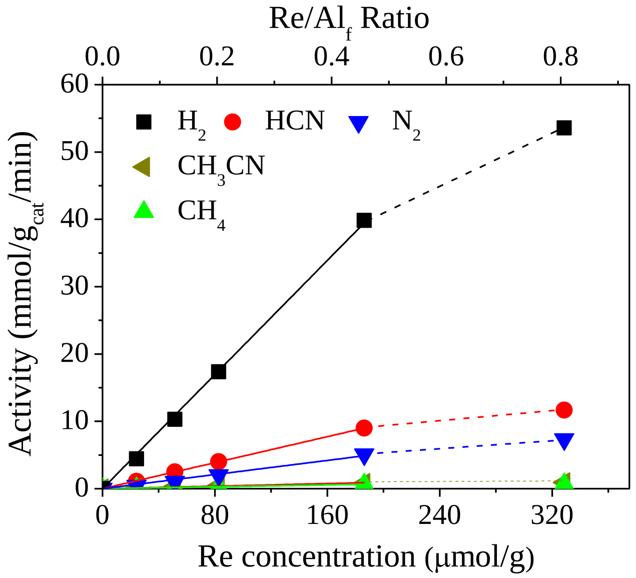

Figure 2.9 Influence of Re concentration on reaction rate

Table 2.1 Compilation of mole-specific activity data for Re-HZSM-5 catalyst with various Re concentrations in ammonia reforming of ethane.

Re concentration (μmol/g)	Re/Al ratio	Activity (mmol/g_{cat}/min)				
		H_2	HCN	N_2	CH_3CN	CH_4
0	0	0	0	0	0	0
24.2	0.06	4.4	1.1	0.4	0.15	0.065
51.6	0.13	10.3	2.5	1.0	0.35	0.19
82.7	0.20	17.4	4	2.0	0.5	0.3
186.4	0.46	39.8	9	5.1	0.8	0.64
328.7	0.80	53.6	11.7	7.3	0.9	0.67

The reaction conditions: T=650 °C, partial pressure ratio of C_2H_6:NH_3:Ar = 0.25:0.5:0.25 atm, GHSV = 6600-133000 h^{-1}.

The linear dependence of the mass-specific activity on the Re concentration also suggests the constant mole-specific activity (turnover frequency). As shown in Fig. 2.10, the mole-specific activities of H_2, HCN, and N_2 are 201, 47.6, and 22 min^{-1}, respectively. Noteworthily, the specific activity is 5.8 min^{-1} for side-product CH_3CN and is only 3.3 min^{-1} for the by-product CH_4. The carbon-based selectivity of HCN is around 75%, which is almost independent of the Re concentration (see Fig. 2.11). Additionally, the selectivity of CH_3CN is < 20% and slightly increases with decreasing Re concentrations, while the selectivity of the by-product CH_4 is around 5% and slightly decreased with decreasing Re concentrations.

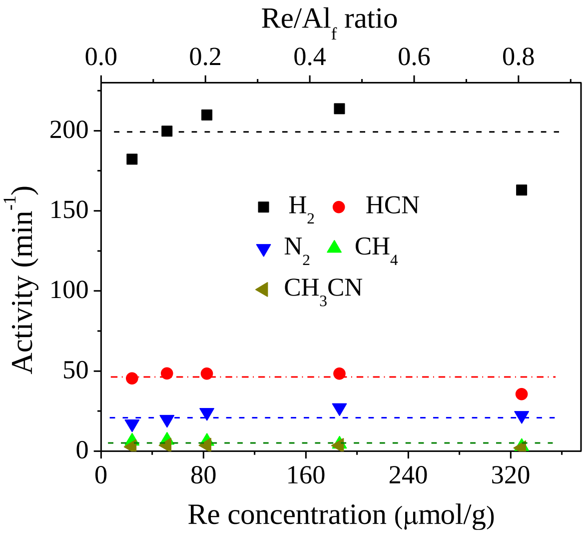

Figure 2.10 Influence of Re concentration on normalized activity

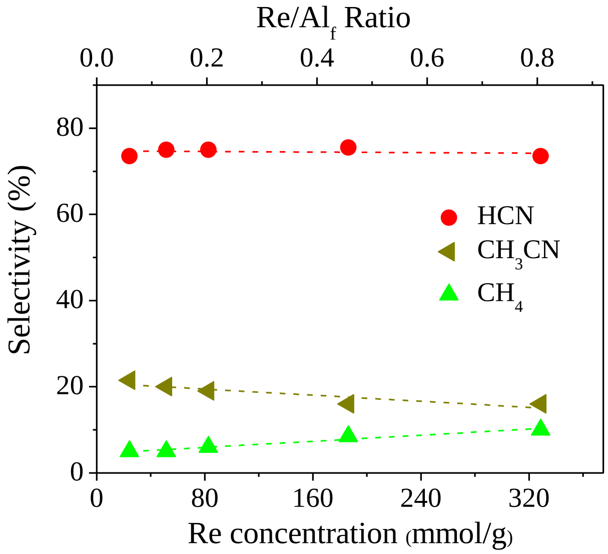

Figure 2.11 Influence of Re concentration on carbon-based selectivity.

Besides the high specific activity under the regular steam/dry reforming conditions, the other intriguing observation of such a catalytic system is about the stability/coke-resistibility. Although coke-induced rapid catalyst deactivation is prevailing during the hydrocarbon transformation, especially at high reaction temperatures over the acidic metal/zeolite catalysts, the

Re/HZSM-5 catalyst, unexpectedly, is highly coke-resistant during the ammonia reforming of ethane and propane. As shown in Fig. 2.12, the mass-specific activities of H_2 during the ethane and propane ammonia reforming over the Re/HZSM-5 (with 82.7 $\mu mol_{Re}/g_{cat}$) are highly stable within the time-on-stream (TOS) up to 20 h. The same stability is also found for the catalyst with the highest Re concentration (186 $\mu mol_{Re}/g_{cat}$); as shown in Fig. 2.13, ethane conversion and carbon selectivity of HCN change little within the TOS up to 93 h. By contrast, the Re/SiO_2 and Ni/HZSM-5 catalysts not only deactivate with TOS (see Fig. 2.14 for the activity coefficient "a", which is defined as the ratio of the real-time reaction rate to the initial reaction rate) but also show significantly lower activity than the Re/HZSM-5.

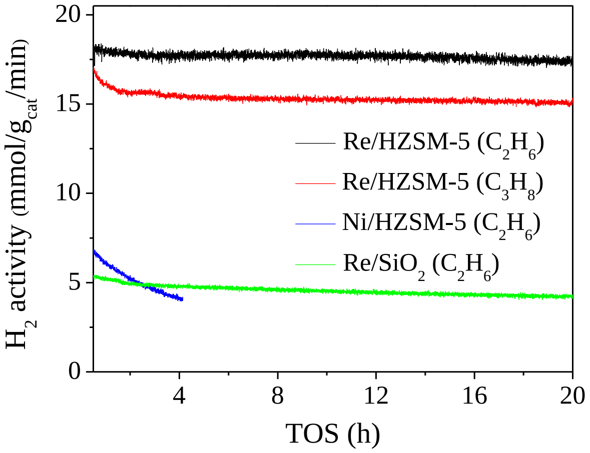

Figure 2.12 Mass-specific activity of H_2 with time-on-stream, over the Re/HZSM-5 (Re/Al_f = 0.2) for ethane and propane ammonia reforming, and over the Re/SiO_2 and Ni/HZSM-5 reference catalysts for ethane ammonia reforming.

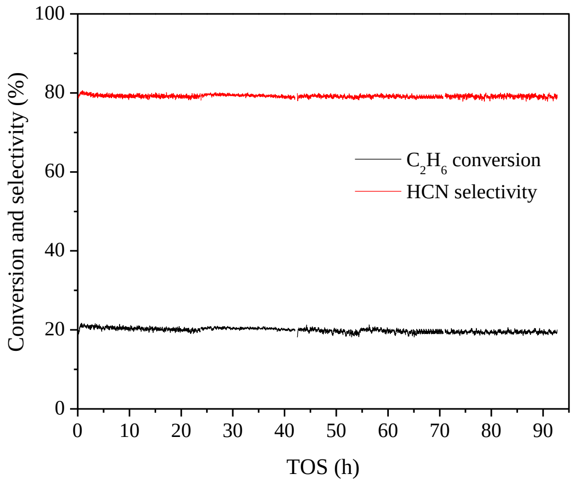

Figure 2.13 Ethane conversion and HCN selectivity, with time-on-stream, over the Re/HZSM-5 ($Re/Al_f = 0.8$) for ethane ammonia reforming.

The reaction conditions: T = 650 °C, partial pressure ratio of C_2H_6:NH_3:Ar = 0.25:0.5:0.25 atm, GHSV = 133000 h^{-1}.

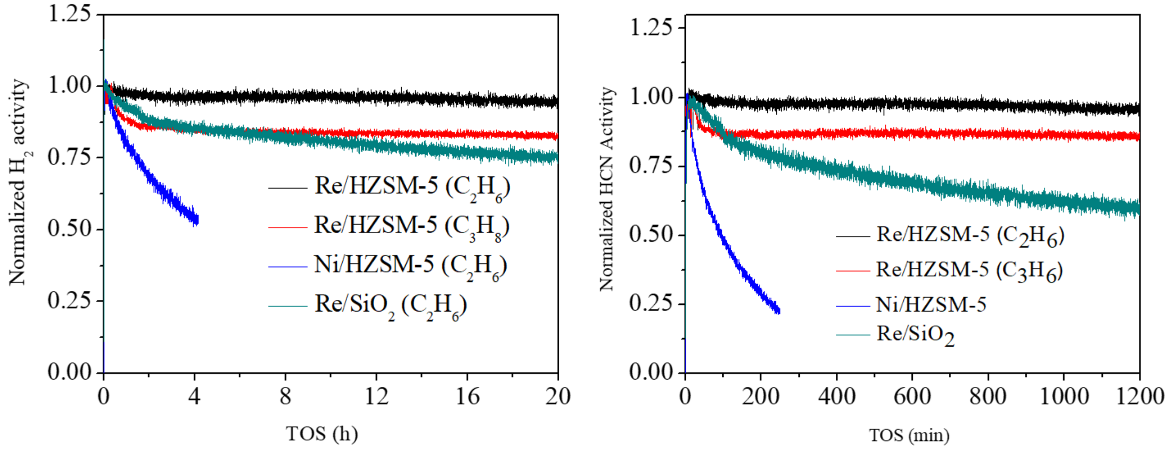

Figure 2.14 Normalizde activity of H_2 (left) and HCN (right), respectively, with time-on-stream.

Over the Re/HZSM-5 (Re/Alf = 0.2) for ethane and propane ammonia reforming, and over the Re/SiO_2 and Ni/HZSM-5 reference catalysts for ethane ammonia reforming. The reaction conditions: T = 650 °C, partial pressure ratio of C_2H_6:NH_3:Ar = 0.25:0.5:0.25 atm, GHSV = 26600 h^{-1} (Re supported catalysts) and 13300 h^{-1} (Ni catalyst).

The outstanding stability of the Re/HZSM-5 catalyst must be associated with the higher coke resistibility. The Re/HZSM-5 has been known as an active catalyst for light alkanes dehydrogenation [19] and dehydroaromatization [20] with serious deactivation due to coking. Catalytic results of ethane aromatization over the Re/HZSM-5 (under the ammonia reforming conditions except for the absence of NH_3) are shown in Fig. 2.15a. It is seen that the catalyst deactivates significantly with TOS due to coke deposition (Fig. 2.15b). The coke deposition was quantified based on the in-situ temperature-programmed oxidation (TPO) of the used catalysts.

As shown in Fig. 2.16, the CO_2 desorption from Re/HZSM-5 and Re/SiO_2 catalysts (after 20 h of TOS for ethane or propane ammonia reforming) is negligible, indicating higher coke resistibility of the Re based catalysts during the ammonia reforming. By contrast, a significant amount of CO_2 was desorbed from Ni/HZSM-5 (Ni has been widely used for the conventional steam/dry reforming) after 4 h of TOS. Further information regarding the coke deposition can be found from the Raman spectra. As shown in Fig. 2.17, the D and G bands of carbon species (at 1340 and 1600 cm^{-1}) were not observed from the used Re/HZSM-5 catalysts. The unprecedented coke resistibility of the Re/HZSM-5 catalyst for the high temperature hydrocarbon conversions must be associated with the presence of NH_3. During the ammonia reforming, the CH_x species from the C-C cleavage (one type of coke precursor) was converted into HCN with NH_3, which prevented the formation of coke on one hand. On the other hand, the strong interaction between NH_3 and Brønsted acid sites could prevent the oligomerization of olefins, which prohibited the formation of polyaromatic species (another type of coke precursor) [21].

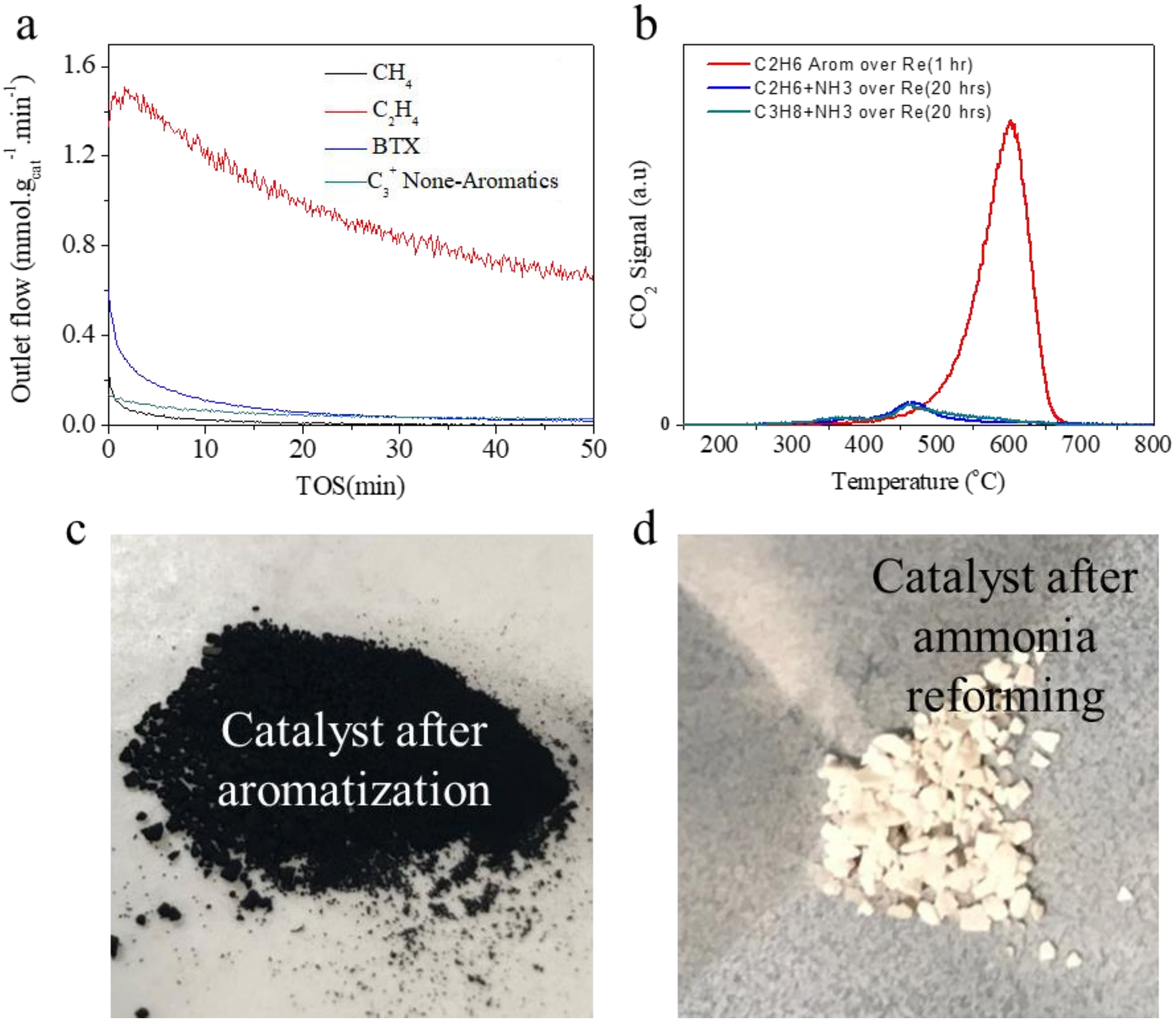

Figure 2.15 (a) Space Time Yield (STY) for products of ethane aromatization over Re/HZSM-5 (Re/Al$_f$ = 0.2). (b): CO_2 desorption profiles during TPO. (c) and (d) pictures of the catalyst after aromatization and ammonia reforming, respectively.

T = 650 °C, partial pressure ratio of C_2H_6:Ar = 0.25:0.75 atm, GHSV = 26600 h^{-1}.

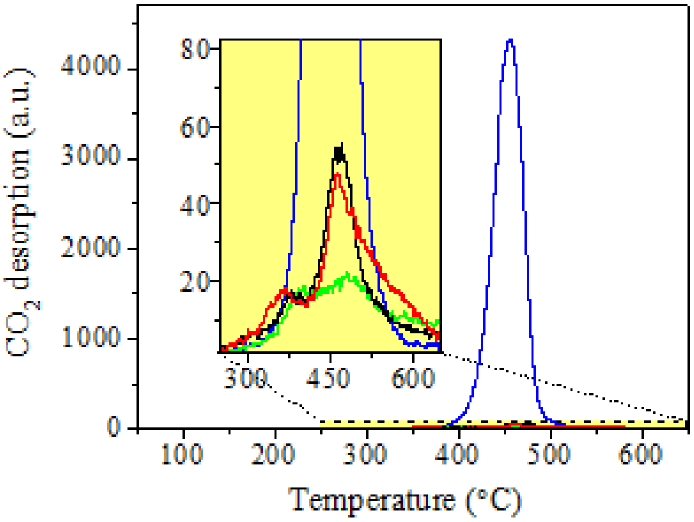

Figure 2.16 CO_2 desorption profiles during TPO for Re supported ZSM-5 (black and Red), Re supported SiO_2 (green) and Ni supported ZSM-5 (blue)in ammonia reforming of ethane/propane.

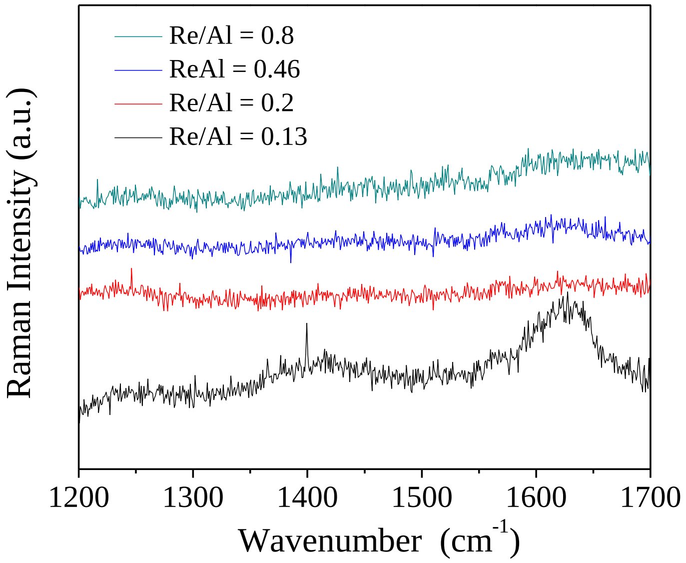

Figure 2.17 Raman spectra of fresh and used samples.

The comparison of the Raman spectra of D and G bands of carbon scattering (at 1340 and 1600 cm^{-1}) for the fresh and used samples confirm the absence of coke deposition during the reaction.

2.3.3 Structure Determination of Re-oxo Active Site

The outstanding catalytic activity and coke-resistibility of the Re/HZSM-5 catalyst inspired us to identify the structure of the Re species before and after the reaction. The Re species were introduced into the zeolite host simply through impregnation (using NH_4ReO_4 as the precursor), followed by solid-state ion exchange under 20% O_2 (see SI method). Characterization of the catalysts by X-ray absorption (XAS) and Raman spectroscopies suggests the formation of isolated ReO_4^- oxo species. Fig. 2.18 shows the XANES spectra of Re L_{III}-edge for the fresh catalysts and NH_4ReO_4 reference. Almost identical white lines, arising from 2 $p_{3/2} \rightarrow 5\ d_{3/2}$ (or 5 $d_{5/2}$) transitions, are found at 10538 eV for the catalysts (with different Re/Al_f ratio) and NH_4ReO_4 reference, confirming that the fresh Re/HZSM-5 catalysts have the same oxidation state (VII) as the NH_4ReO_4 regardless of the Re loading. The L_{III}-edge k^3-weighted Fourier-transform of the extended fine-structure (EXAFS) spectra for the fresh catalysts and reference are shown in Fig. 2.19. The spectra exhibit a pronounced peak at 1.3 Å, originated from the first shell Re-O scattering. There are no peaks at a high R distance of 2-4 Å, indicating the Re-Re scattering ins the catalysts are negligible, which suggests the formation of mainly single-atom isolated ReO_x sites rather than nanoparticles or nanoclusters [19-20].

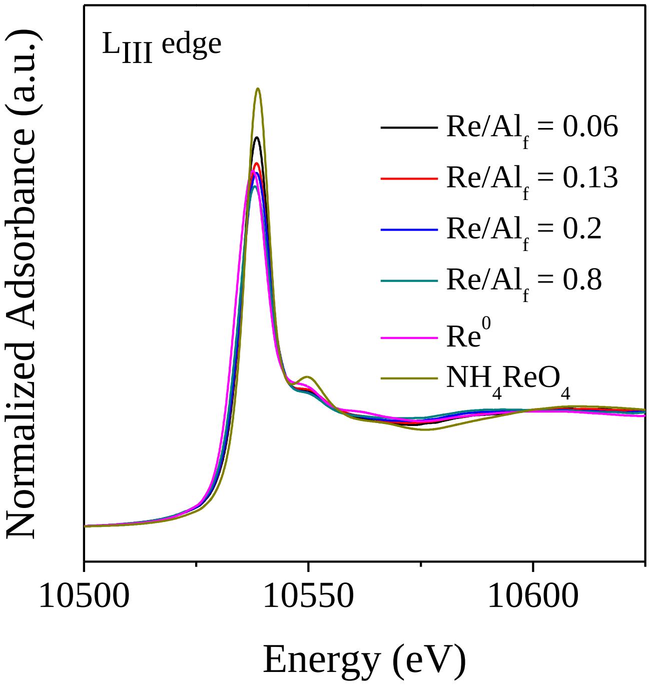

Figure 2.18   Re L$_{III}$ edge XANES spectra of the fresh catalysts and NH$_4$ReO$_4$ reference

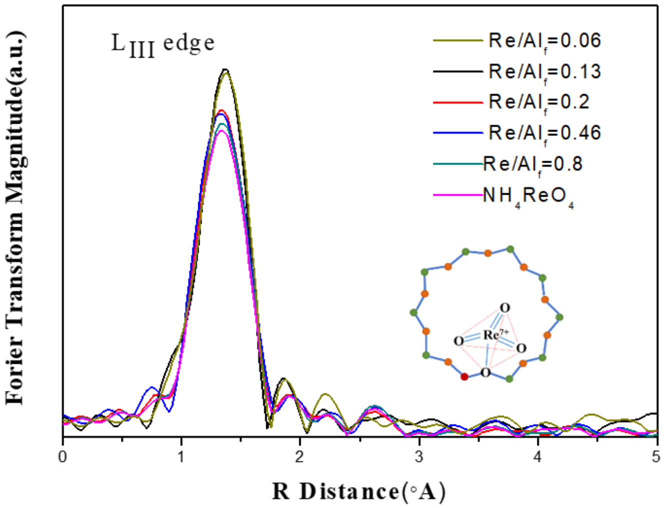

Figure 2.19   Re L$_{III}$ edge EXFAS spectra of the fresh catalysts and NH$_4$ReO$_4$

The coordination structures of the isolated ReO_x sites were obtained by further fitting the EXAFS spectra. The coordination number (CN), interatomic distance (R), Debye-Waller factor (σ^2), and inner potential correction (ΔE) of the EXAFS analysis are summarized in Table 2.2. The oxygen coordination is ~4 in all catalysts, suggesting that the tetrahedrally coordinated ReO_4^- structure is formed and the average absorber-back-scatterer distance between Re and O is 1.73Å [19-20]. Fig. 2.19 (inset) shows a cartoon that demonstrates the ReO_4^- tetrahedral in the 10MR (10-membered ring) of the ZSM zeolite.

Table 2.2 Analysis of EXAFS data for the fresh Re-HZSM-5 samples with various Re/Al ratios

Sample	$N_{Re=O}$	$R_{Re=O}$ (Å)	σ^2 (Å^2)	ΔE (eV)
Re/Al=0.06	4.0	1.733 ∓ 0.015	0.0001	8.8
Re/Al=0.13	4.0	1.728 ∓ 0.012	0.00004	7.9
Re/Al=0.2	4.1	1.728 ∓ 0.013	0.0009	8
Re/Al=0.46	4.3	1.727 ∓ 0.017	0.0013	7.8
Re/Al=0.8	3.8	1.727 ∓ 0.013	0.0007	7.8

The absence of ReO_x particles or clusters is also confirmed by the HAADF-STEM (see Fig. 2.20). Note that the STEM technique is difficult to probe the single atom in/on the zeolite support due to sensitivity to electron beam irradiation.[22] Nonetheless, the EDS mapping (Fig. 2.21) demonstrates the presence of Re species that are homogeneously distributed among the zeolite crystals.

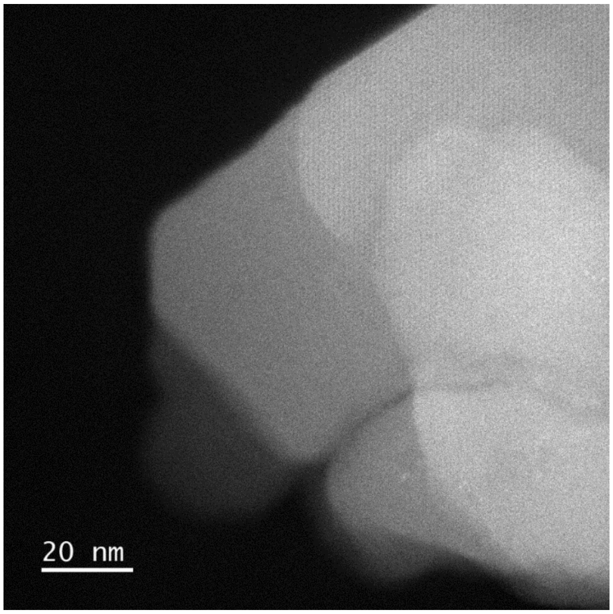

Figure 2.20 HAADF-STEM image of the fresh and used catalyst (Re/Al$_f$=0.2)

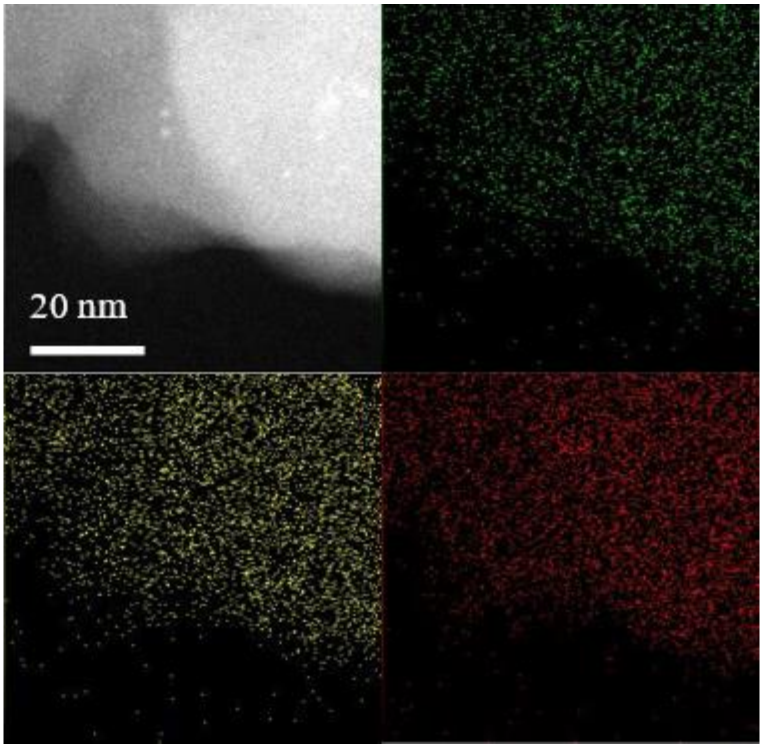

Figure 2.21 EDS elements mapping of the fresh and used catalyst (Re/Al$_f$=0.2)

Raman spectra were collected to further verify the ReO_4^- tetrahedral structure in the zeolite support. As shown in Fig. 2.22, the fresh Re/HZSM-5 catalysts (Re/Al_f ratio range from 0.2 to 0.8) exhibit a prominent peak at 985 cm^{-1}, which is corresponding to the v_s (O=Re=O) symmetric stretching vibration [19-20]. This is consistent with the same mode in the spectrum of the NH_4ReO_4 reference at 978 cm^{-1}. The peaks shift to higher frequencies relative to the NH_4ReO_4, indicating the tetrahedral ReO_4^- structure is distorted when connected to the Al_f through zeolite-lattice oxygen atoms (O_f) [19]. A weak shoulder peak at 1006 cm^{-1} is identified for the $Re/Al_f=0.8$ catalyst, indicating that there are different anchoring sites for the ReO_3^+ [23]. While the O_f ($Al-O_f^-$ $-Si$) is a preferential anchoring site for such Re oxo species, at a higher Re/Al_f ratio, a part of the Re oxo species might be connected to the silanol or extra framework Al [23]. The broad peak at 930 cm^{-1} could originate from the asymmetric stretching of the terminal O=Re=O and the stretching of the bridge Re-O-Si [19-20].

The results of NH_3-TPD for fresh samples are shown in fig. 2.23 and compared with NH_3-TPD profile of HZSM-5($Si/Al_2=80$). With increasing the Re loading the intensity of peak located at higher temperatures associated with Bronsted acid sites decreases while the intensity of peak located at low temperature assigned to Lewis acid sites increases. This further confirms that Re species exchanges with Bronsted acid centers in zeolite forming new Lewis acid sites which is consistent with the assumption of Re oxo single active site.

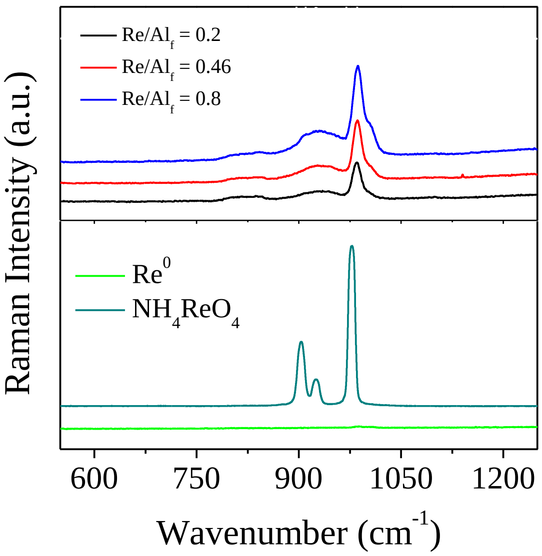

Figure 2.22 Raman spectra of the fresh catalysts and Re^0 and NH_4ReO_4 references. The Re^0 reference refer to Re/HZSM-5 sample being reduced in H_2 at 650 °C for 1 h.

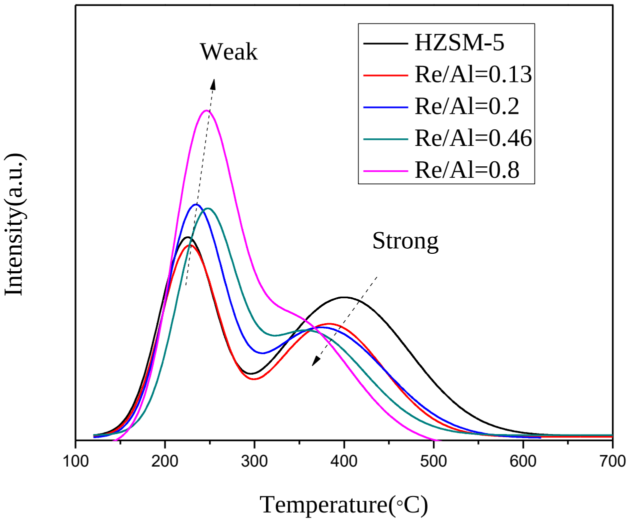

Figure 2.23 NH_3-TPD profile of Re supported HZSM-5 and parent support (Si/Al_2=80).

While the formation of isolated ReO_4^- tetrahedral in the zeolite for the fresh catalyst is not unusual, further characterization of the Re/HZSM-5 catalysts after reaction suggests that the isolated ReO_4^- sites remain stable during the light alkane ammonia reforming at 650ºC. As shown in Fig. 2.24, the prominent Raman peak at 980 cm^{-1}, corresponding to the v_s (O=Re=O) symmetric stretching vibration, is retained after the ammonia reforming reaction. Note that the characteristic Raman peak for the v_s (O=Re=O) is not observed for the Re^0 reference (prepared through reducing the Re/HZSM-5 sample in H_2 at 650ºC for 1 h), indicating that the Re (VII) oxo sites can be easily reduced to Re^0 (see Fig. 2.25 for H_2-TPR profiles) [19]. Nonetheless, such oxo sites are largely preserved during the reaction process, despite that the partial pressure of H_2 during the steady-state ammonia reforming of ethane is up to 40% depending on the reaction conditions.

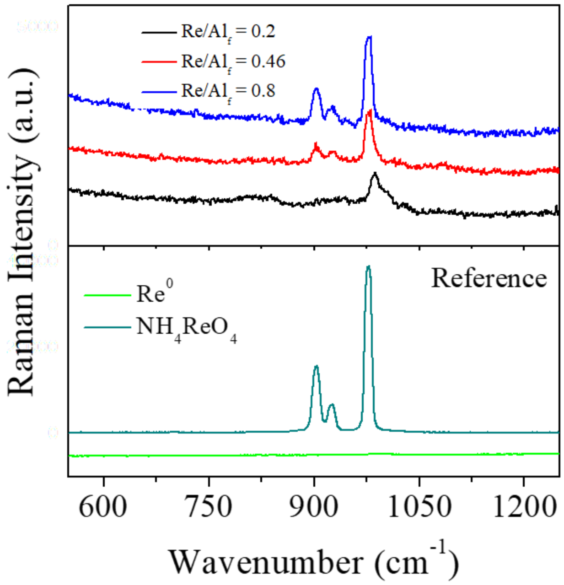

Figure 2.24 Raman spectra of the used catalysts and Re^0 and NH_4ReO_4 references. The Re^0 reference refer to Re/HZSM-5 sample being reduced in H_2 at 650 °C for 1 h.

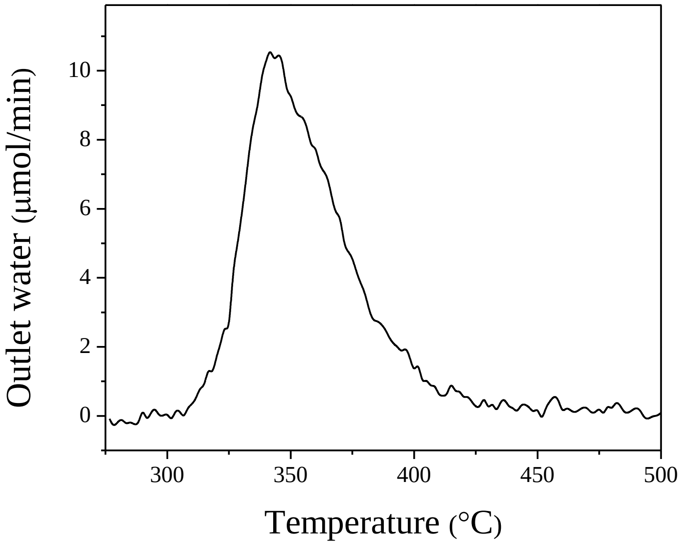

Figure 2.25 H_2-TPR profiles of Re/HZSM-5 ($Re/Al_f = 0.2$) catalyst

The preservation of Re (VII) oxo sites after the high temperature ammonia reforming were also verified by the EXAFS and XANES spectra of the used catalysts. The L_{III}-edge k^3-weighted Fourier-transform of the extended fine-structure (EXAFS) spectra for the used catalysts and references (Re^0 and NH_4ReO_4) are shown in Fig. 2.26 The spectra exhibit the same pronounced peak at 1.3 Å as the fresh catalysts and NH_4ReO_4 reference, again indicating that the retained ReO_4^- tetrahedral. The spectra of Re^0 reference shows pronounced peaks at 2-3 Å for the Re-Re scattering, which is absent from the spectra of the used catalyst, which is consistent with the observation from Raman spectra. It is also noteworthy to mention that by comparing the EXAFS Re L_{III} edge of used sample with the main scattering path for other possible structures such as ReO_2 and ReO_3, the presence of these oxide clusters could be ruled out since none of the used samples shows the strong feature at high R distance as characteristics ofthese oxide clusters (see fig. 2.27).

The XANES spectra of Re L_I and L_{III} edges for the used catalysts and references are shown in Fig. 2.28-29. The presence of a pre-edge peak at 12526 eV in the Re L_I edge XANES spectra of the used catalysts is another strong evidence for the preservation of Re (VII) oxo sites. Nonetheless, a slight shift of the Re L_{III} edge XANES spectra towards lower energy (with respect to the NH_4ReO_4 reference) is evident for the used catalysts, and such a shift becomes even larger for the Re^0 reference. Therefore, we expect that a part of the Re (VII) oxo site is reduced during the reaction process.

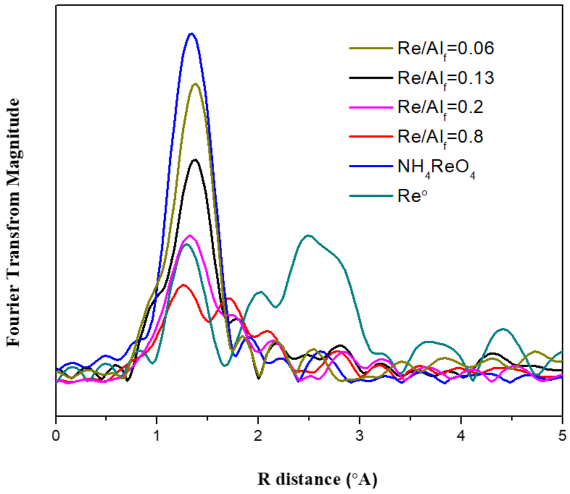

Figure 2.26 Re L_{III} edge EXFAS spectra of the used catalysts and Re^0 and NH_4ReO_4 references

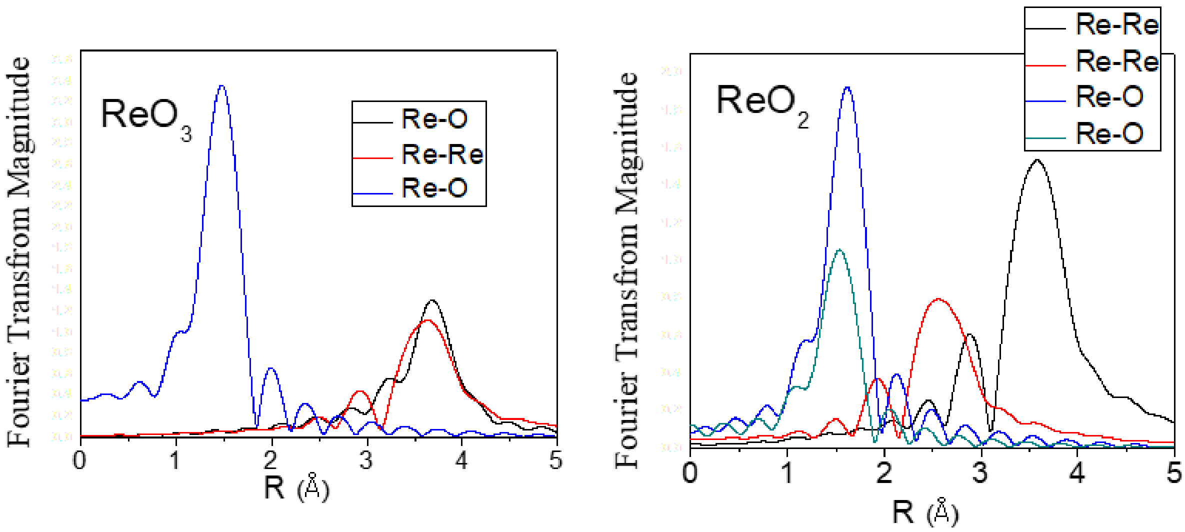

Figure 2.27 Spectra of main scattering path for ReO_2 and ReO_3 oxides

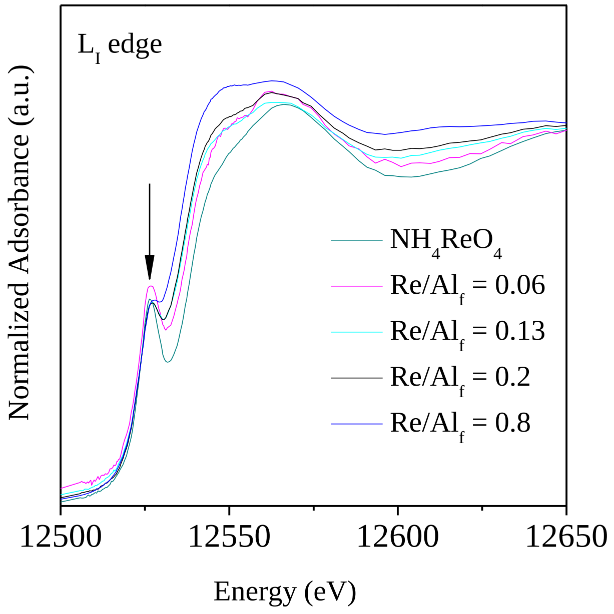

Figure 2.28 The XANES spectra of Re L_I edges for the used catalysts and references

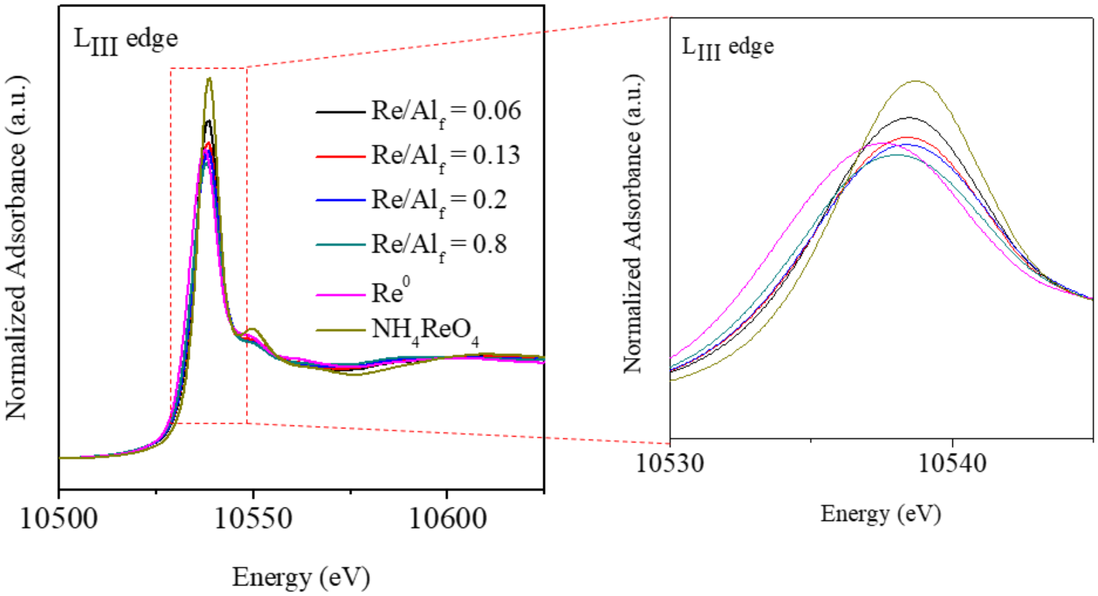

Figure 2.29 The XANES spectra of Re L$_{III}$ edge for the used catalysts and references

Further characterization of the used catalyst by HAADF-STEM (see Fig. 2.31) suggests the formation of nanoparticles (<1.5 nm), which most probably originates from the oligomerization and reduction of rhenia sites on the external surface. In ZSM-5, two anchoring sites is considered for Re oxo structure; Bronsted acid sites mainly located inside zeolite pores, and silanol groups being in the outer surface. We expect those Re species anchored to silanol groups in the outer surface of zeolite could not retain the initial oxo structure upon exposure to the reaction mixture due to lack of confinement effect as well as a weaker bond of Re oxo to silanol group compared to those attached to Bronsted acid sites of zeolite. To further prove such a hypothesis, we prepared Re supported silica and tested it in ammonia assisted ethane reforming. Re L$_I$ edge XANES spectra of this sample after the reaction is shown in figure 2.30 and compared with spectra of fresh sample. As it is obvious while fresh sample shows the pre-edge feature characteristics of the presence of

Re oxo structure, this disappears for the used sample, indicating that Re oxo site attached to silanol group being reconstructed during the reaction. The EDS mapping (Fig. 2.32) again demonstrates the homogeneous distribution of rhenia sites among the zeolite crystals, which is consistent with our conclusion regarding the presence of Re oxo structure for majority of Re species after reaction.

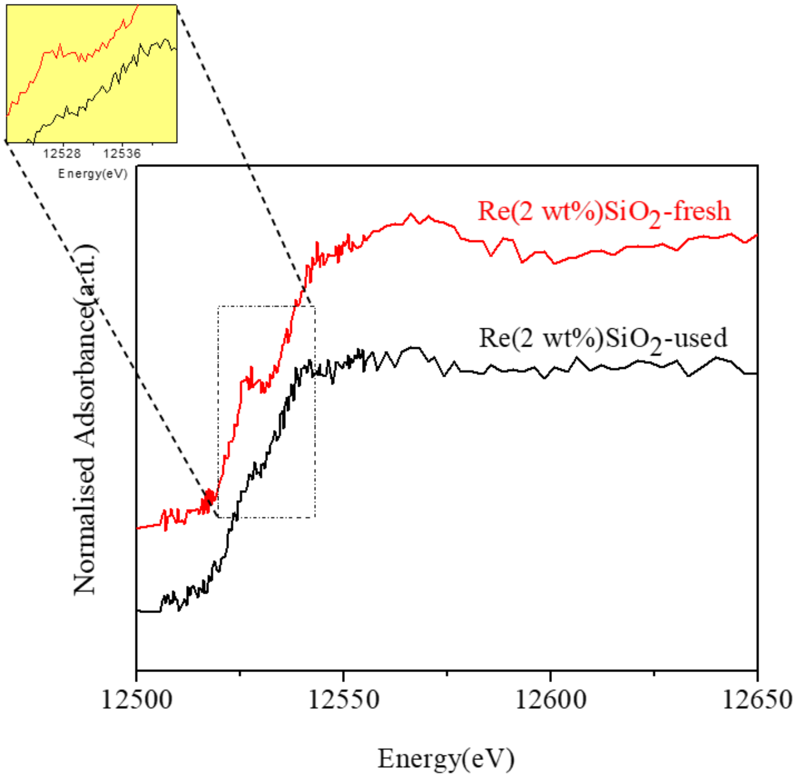

Figure 2.30 Re L_I edge XANES spectra of fresh and used Re (2 wt%) supported SiO_2 catalyst

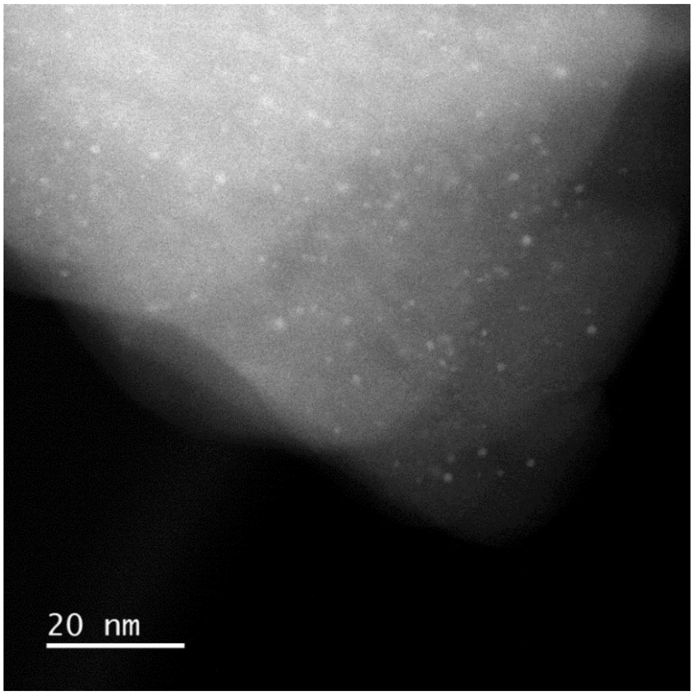

Figure 2.31 HAADF-STEM image of the used catalyst (Re/Al$_f$=0.2)

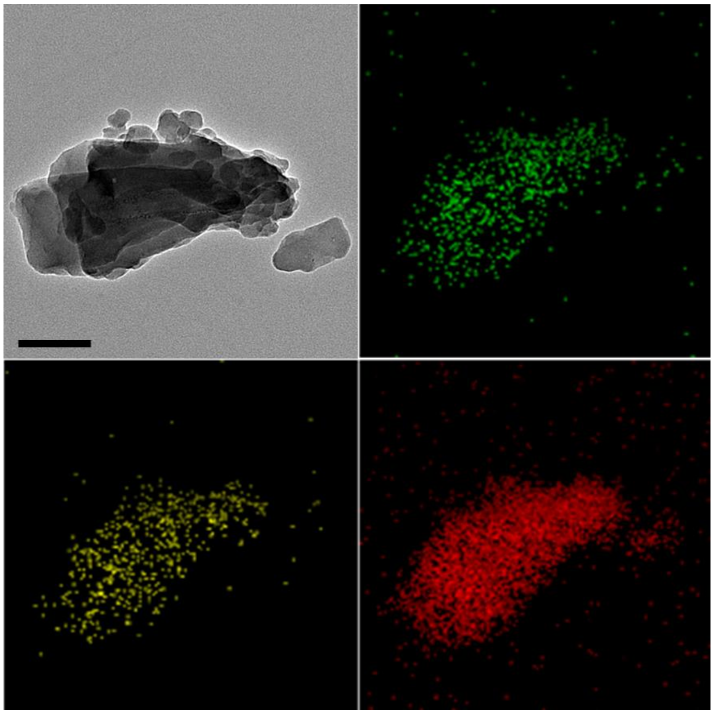

Figure 2.32 EDS elements mapping of the used catalyst (Re/Al$_f$=0.2), scale bar: 100 nm.

2.3.4 Mechanism and Discussion

Notably, the intensities of the Raman peak at 980 cm^{-1}, EXAFS peak at 1.3 Å, and the pre-edge peak at 12526 eV in the Re L_I edge XANES spectra all decrease for the used catalysts with reference to the fresh catalysts. Further operando-type transient kinetic analysis suggests that the declined spectroscopies' intensity is owing to the partial reduction of the original ReO_4^- tetrahedral structure, creating highly defective ReO_x ($x \approx 2$) oxo sites during the early-stage of the reaction. As shown in Fig. 2.33 (left), a sharp peak of CO_2 and a broader peak of H_2O are observed during the early-stage induction period. Quantification of total O (in CO_2 and H_2O) desorbed during the induction period suggests that nearly 50% of O in ReO_4^- tetrahedral structure is removed (see Oxygen Defects (%) in Fig. 2.33(right).

In terms of the catalytic behavior during the induction period, as shown in Fig. 2.34a, CH_4 and C_2H_6 appear in the gas phase almost simultaneously with the inert standard (Ar) during the early-stage induction period; NH_3 and CH_3CN are absent within the initial 7 seconds, and HCN emerges after 18 seconds. It takes up to 2.75 min for HCN to reach a steady-state, and the partial reduction of ReO_4^- tetrahedral is complete (*i.e.*, CO_2 and H_2O disappeared from the reactor effluent) at almost the same time. Further correlation of the early-stage activity with oxygen defects (refer to fig. 2.33(right)) demonstrates a linear relationship between the mass-specific activity of HCN and the degree of oxygen defects, indicating the pivotal role of the highly defective ReO_x ($x \approx 2$) oxo in the ammonia reforming of light alkanes. The mass-specific activities of CH_4 and CH_3CN are independent of the oxygen defects, so different catalytically active sites (probably the external Re nanoclusters) and mechanisms might be involved. The formation of CH_3CN from ethane and ammonia through tandem dehydrogenation/amination/dehydrogenation has been proposed during our recent study on the Pt/HZSM-5 catalyst [21].

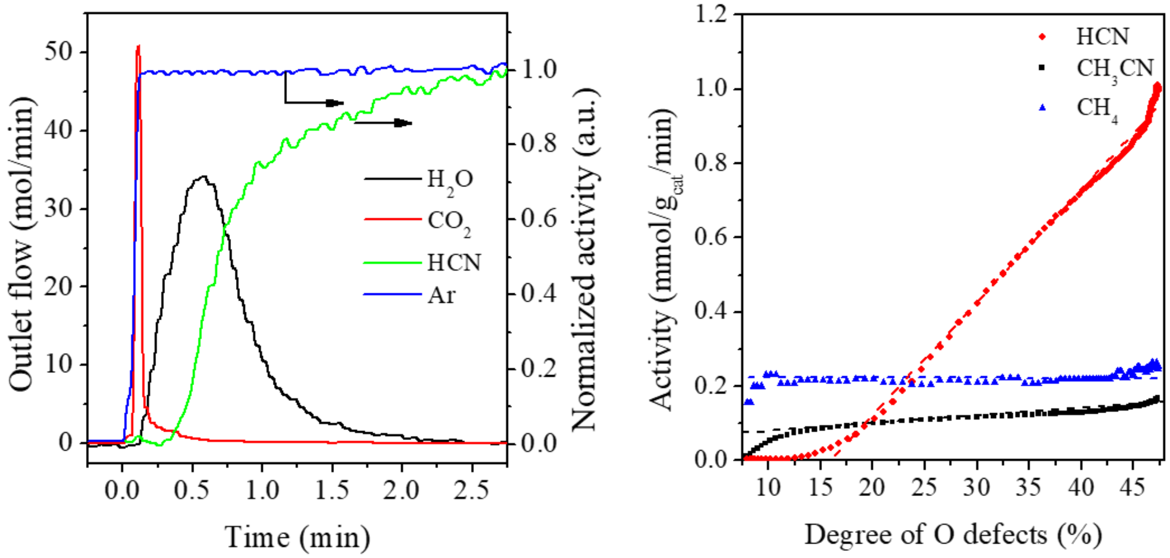

Figure 2.33 Transient kinetic analysis with partial pressure step-perturbation.

(Left) outlet flow of CO_2 and H_2O, and normalized outlet flow of HCN and inert standard (Ar) during the early-stage (Right) early-stage activities of HCN, CH_3CN, and CH_4 as a function of the degree of O defects. The degree of O defects was calculated by integrating the CO_2 and H_2O peak and normalizing it by the nominal O in the ReO_4^- tetrahedral based on the Re concentration from ICP. The transient experiment was performed at 600 ºC under atmospheric pressure ($NH_3/C_2H_6/Ar$ = 20/10/10 ml/min) over 0.2 g of Re/HZSM-5 (Re/Al_f = 0.2) catalyst.

It must be noted that the significant early-stage delay of HCN is absent during the second cycle transient experiment (see Fig. 2.34b). HCN appears in the product stream simultaneously with the NH_3 and CH_3CN, which show decreased delaying time around 4 s. This once again corroborates that the delay during the first cycle transient experiment originates from the partial reduction of the ReO_4^- tetrahedral. Moreover, during second cycle early-stage behavior of catalyst, CH_4 formation rate initially show a spike which later start decreasing once NH_3 appears in the gas phase. This suggest that before NH_3 cover all active Re sites, this site promotes CH_4 formation and NH_3 coverage of active sites inhibit CH_4 formation in favor of C-N linkage and HCN formation.

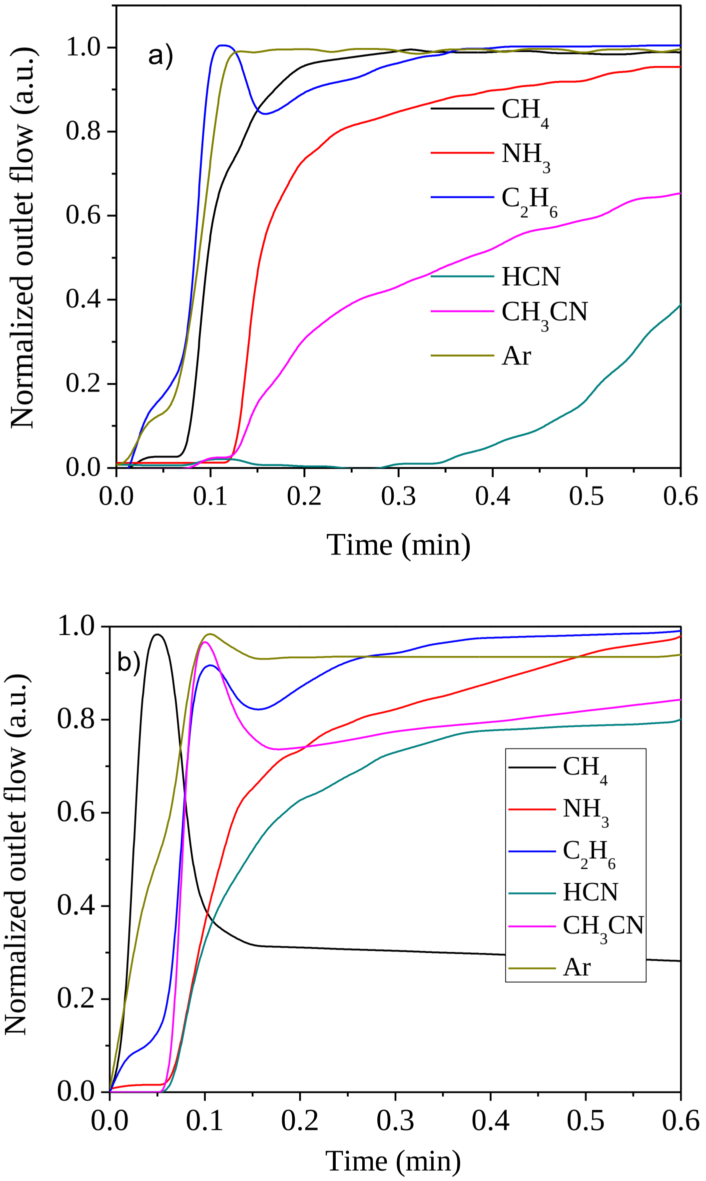

Figure 2.34 a) First cycle, and b) second cycle early-stage behavior of Re/HZSM-5 ($Re/Al_f = 0.2$) catalyst in ethane ammonia reforming.

The reaction conditions: T = 600 °C, partial pressure ratio of C_2H_6:NH_3:Ar = 0.25:0.5:0.25 atm, GHSV = 6600 h^{-1}.

The surface coverage of carbon during the early-stage behavior of catalyst was calculated and its correlation with HCN formation rate is shown in figure 2.35. From this figure, there is no linear correlation between surface carbon and HCN formation rate, showing that C_2H_6 adsorbed on the surface is less likely to be involved in HCN formation. However, if we plot the HCN formation rate versus gas-phase partial pressure of C_2H_6, as it is shown in figure 2.36, a linear relation could be observed, indicating gas-phase C_2H_6 may react with NH_3 derived intermediate bonded to the catalysts surface.

The surface coverage of different species during the steady-state ammonia reforming of ethane was quantified based on the time-dependent decay during the back-transient. As shown in Fig. 2.37, CH_4, C_2H_6, and CH_3CN disappear from the reactor effluent quickly (similar to Ar inert standard) after switching from reactants mixture to inert. Integrated decay curves suggest that the surface coverages of CH_4, C_2H_6, and CH_3CN during the ammonia reforming of ethane are negligible. The decay of NH_3 and HCN takes a significantly longer time than that of Ar, implying that they dominate the surface/active sites of the catalyst during the reaction.

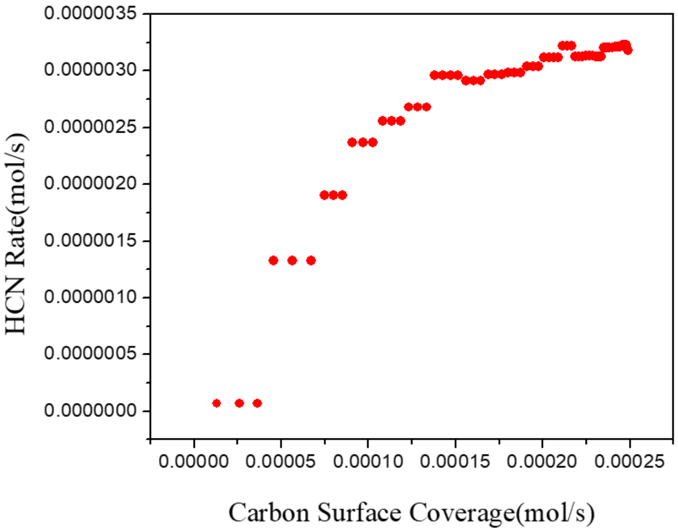

Figure 2.35 HCN formation rate versus carbon surface coverage during early stage behavior of Re/HZSM-5 (Re/Al_f = 0.2) catalyst in ethane ammonia reforming.

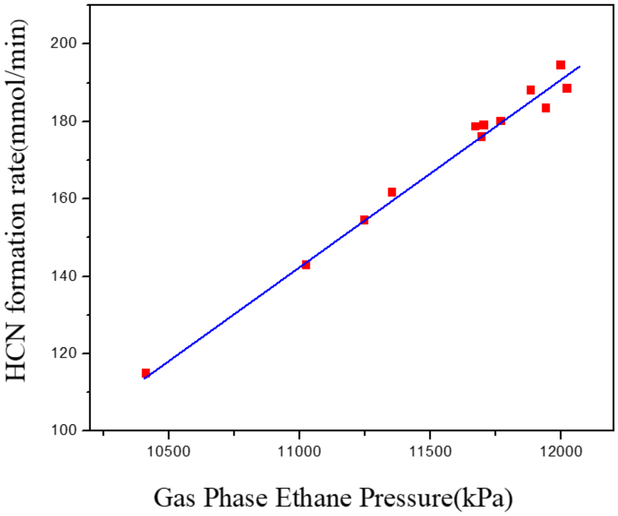

Figure 2.36 HCN formation rate versus gas phase ethane partial pressure during early stage behavior of Re/HZSM-5 (Re/Al$_f$ = 0.2) catalyst in ethane ammonia reforming.

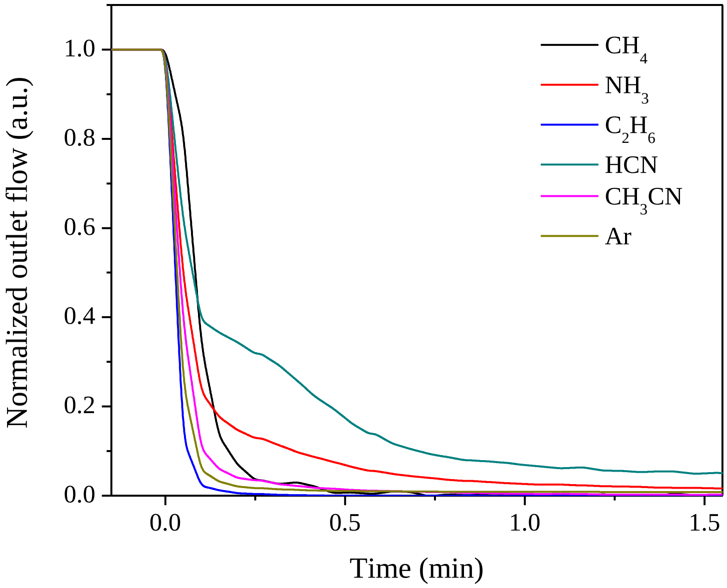

Figure 2.37 Back transient decay of various species in ethane ammonia reforming over Re/HZSM-5 (Re/Al$_f$=0.2)

The total specific amounts of NH_3 and HCN desorbed from the catalyst during the back transient are 207 and 309 μmol/g$_{Cat}$, respectively (see Table 2.3). These amounts correspond to approximately 50% of coverage of Brønsted acid sites by NH_3 and 400% of coverage of Re-oxo by HCN, respectively. Therefore, it might be expected that the highly defective ReO_x ($x \approx 2$) oxo tetrahedral is transformed into an octahedral structure coordinated with HCN, and the desorption of which could be the rate-limiting step. Although our results suggested that the Brønsted acid sites are not directly involved in the catalytic reforming, the "NH_3-pool" populated around the rhenia sites might be desired for ammonia reforming of light alkanes.

Moreover, from steady state kinetic experiments shown in figure 2.38 and 2.39, a Longmuir type isotherm could be observed for dependency of HCN formation rate on NH_3 partial pressure, showing a linear relationship at low NH_3 partial pressure which turns to zero order at high NH_3 partial pressure. This indicates that NH_3 or NH_3 derived intermediates are involved in RDS and cover most of the catalyst's surface similar to what is obtained from quantification of back transient (Fig. 2.37 and table 2.3). On the other hand, HCN formation rate show almost 0.5 order (~ 0.65) dependence on C_2H_6 partial pressure (Fig. 2.39). This suggests that C_2H_6 is involved in RDS and does not exist on the catalytic surfaces at considerable amounts which is consistent with the already discussed results of early stage and back transient quantification.

Considering what is mentioned so far, the rate law for HCN formation can be written as:

$$HCN = \frac{K_{HCN} P_{NH_3} {P_{C_2H_6}}^{0.5}}{(1 + K_1 P_{NH3})} \tag{2.14}$$

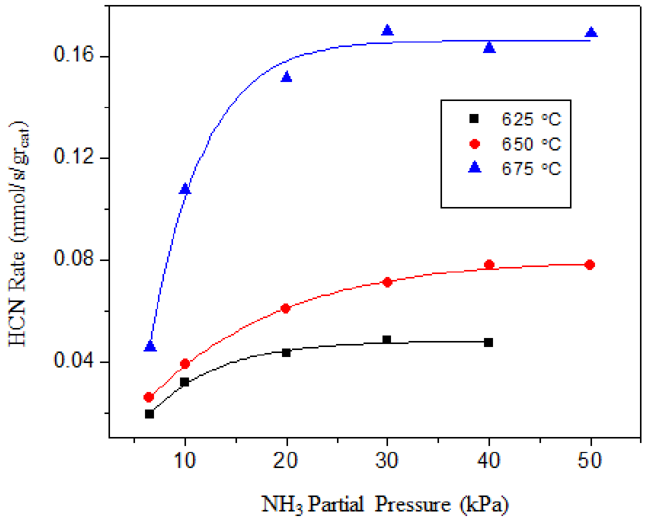

Figure 2.38 Steady state dependence of HCN formation rate on NH_3 partial pressure in ethane ammonia reforming over Re/HZSM-5 (Re/Al_f=0.2)

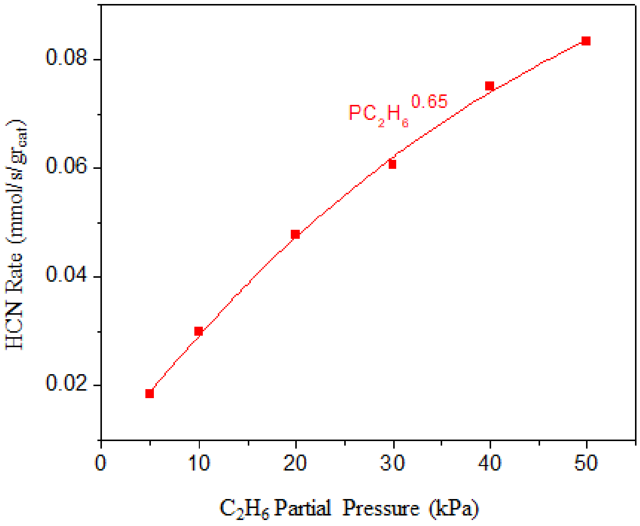

Figure 2.39 Steady state dependence of HCN formation rate on C_2H_6 partial pressure in ethane ammonia reforming over Re/HZSM-5 (Re/Al_f=0.2)

Table 2.3 The quantification of specific amounts of various species desorbed from the catalyst surface during the back-transient and the overall numbers of Bronsted (H^+ protons) and Lewis acid sites (Re oxo moieties) for ammonia reforming of ethane Re/HZSM-5 (Re/Alf = 0.2) catalyst.

	CH_4	NH_3	C_2H_6	HCN	CH_3CN
Specific amounts (μmol/g)[a]	12	207	0	309	2.5
Ratio to Bronsted acid sites		0.5			
Ratio to Re oxo sites[a]				3.9	

[a] Data calculated based on back-transient calculations (fig. 2.35)

Table 2.4 Summary of H_2 production rate in Dry/Steam Reforming of Ethane/propane over various catalysts presented in the literature

Catalyst	H_2 Rate (min^{-1})	H_2 Rate (mmol/gr/min)	T (K)	GHSV ($ml/g_{cat}/h$)	Feed Composition	Ref.
Re/HZSM-5 (Re/Al = 0.8)	198	53.5	923	132000	$NH_3:C_2H_6:Ar$ 2:1:1	This work
Re/HZSM-5 (Re/Al = 0.2)	186	15.4	923	132000	$NH_3:C_3H_8:Ar$ 2:1:1	
$PtNi/CeO_2$	33.3	11.3[a]	873	240000	$CO_2:C_2H_6:Ar$ 2:1:5	[25]
Pt/CeO_2	4.8					
Ni/CeO_2	9.8					
$PtCo/CeO_2$	82.5	3[a]	873	24000	$CO_2:C_2H_6:He$ 1:1:2	[26]
Rh/Al_2O_3	6	/	723	100000	$C_3H_8:H_2O:He$ 1:11:12	[27]
Ir/Al_2O_3	3	/				
Ru/Al_2O_3	2.4	/				
Pt/Al_2O_3	1.2	/				
Rh/YSZ	120	5.8[a]				
$Mo\text{-}Ni/Al_2O_3$	/	0.055	923	12000	$CO_2:C_3H_8$ 5	[28]
$Co\text{-}Ni/Al_2O_3$	/	0.04				
$Ni\text{-}Ce/MgAl_2O_4$	/	16.95[a]	873	30000	$C_3H_8:N_2:H_2O$ 1:1:3	[29, 30]
$La\text{-}NiO\text{-}MgO\text{-}SiO_2$	/	32.89[a]	973	100000	$C_3H_8:N_2:H_2O$ 1:3:3	[31]
$LaFe_{0.9}Ni_{0.1}O_3$	/	2.385 [a]	873	24000	$C_2H_6:CO_2:Ar$ 1:1:2	[32]
$Ni_{1.96}Pd_{0.04}MnO_4/\gamma\text{-}Al_2O_3$	/	0.482 [a]	973	5600	C_3H_8: H_2O 1:6	[33]
$NiGa/SiO_2$	1948[a]	2[a]	873	/	$H_2O:C_3H_8:Ar$ 8.1:0.9:91	[34]

[a] Rate calculated with respect to the available data

Table 2.5 Summary of H_2 production rate in NH_3 decomposition over various catalysts presented in the literature

Catalyst	H_2 Rate (min^{-1})	H_2 Rate (mmol/gr/min)	T (K)	GHSV ($ml/g_{cat}/h$)	Ref.
Co-Mo bulk metallic	0.033	0.2	773	36000	[35]
CoMoN	0.38	0.38	773	6000	[36]
Ni–Ce–Al–O		5.5	773	18000	[37]
Co /Na-SiO_2	78	7	873	36000	[38]
Co /Na-SiO_2	0.51	0.15	773	150000	[39]
Al_2O_3-K_2O/Co_3O_4	0.83	6.6	773	24000	[40]
Co/MgLa	0.55	6.4	773	6000	[41]
Co/MgO-La_2O_3	0.6	9.03	773	6000	[42]
Co-Al	/	36.8	873	36000	[43]
Ni/SBA-15	9.6	3.8	773	30000	[44]
Ni/Al_2O_3(CeO_2)	8.2	6.1	773	30000	[45]
Fe_2O_3–SiO_2	82	4.4	1023	15000	[46]
Fe/C	8.5	0.2	773	7500	[47]
Fe/CNT	17.6	0.8	973	5000	[48]
Mo_2C	18.5	9	873	36000	[49]
FeCo/CNT	68	3	873	36000	[50]
FeMo/La–Al_2O_3	110.7	9.7	873	46000	[51]
Fe/CNF	1.98	0.5	773	6500	[52]
CoMo/γ-Al_2O_3	76	4.45	773	36000	[53]
Co-Re/SiO_2	/	0.007	723	6000	[54]
Ru/La_2O_3	498	14.6	723	18000	[55]
Ru/$La_{0.33}Ce_{0.67}$	684	26.5	723	30000	
Ru/CeO_2	138	/	823	3067	[56]
Ni/CeO_2	15	/			

2.4 Conclusions

To summarize, we demonstrated that the ammonia reforming of ethane and propane can be realized at the same temperature range as the traditional steam/dry reforming over the isolated Re oxo sites in the HZSM-5 zeolite. Such a process extracts H_2 simultaneously from NH_3 and light alkanes (both can be liquefied at relatively low pressure that facilitates transportation) and co-produces HCN as value-added chemicals or if not need can be converted back to NH_3 through hydrolysis. Hydrogen produced from the ammonia reforming of light alkanes is CO_x free and can be used directly for PEMFCs. The Re/HZSM-5 catalyst developed in this study is highly active and stable. The highly defective ReO_x ($x \approx 2$) oxo tetrahedral was anticipated to be the catalytically active site for the ammonia reforming of alkanes. The specific activity of such isolated Re oxo sites is up to ~1 mol_{H2}/g_{Re}/min (or turnover frequency ~180 min^{-1}) for the ammonia reforming of ethane at 650ºC, which is significantly higher than H_2 production from steam and dry reforming of ethane or propane and ammonia direct decomposition (see Tables 2.4 and 2.5). Additionally, the Re/HZSM-5 catalyst is also highly coke-resistant for the ammonia reforming of ethane and propane, no significant catalyst deactivation was observed with time-on-stream up to 93 h. The Re/HZSM-5 is a conventional catalyst for light alkanes dehydrogenation and aromatization that has a significant challenge of coke deposition.[19-20, 24] The presence of NH_3, due to the strong interaction with the Lewis and Brønsted acids prohibited the C-C coupling through oligomerization and coke deposition. As we have seen, the Re/HZSM-5 catalyst demonstrated superior performance than the conventional steam or dry reforming, so appears to have considerable potential for CO_x free H_2 production in the industrial. Additionally, the present catalytic system demonstrated significantly reduced reaction temperatures compared with the commercial BMA and Shawinigan processes, therefore could be an important alternative for industrial HCN production.

2.5 References

1. Hydrogen: A Clean, Flexible Energy Carrie. 2017, https://www.energy.gov/eere/articles/hydrogen-clean-flexible-energy-carrier#:~:text=Hydrogen%20is%20a%20clean%20fuel,water%2C%20electricity%2C%20and%20heat.&text=Due%20to%20their%20high%20efficiency,gas%20emission%20in%20many%20applications.

2. Bakenne, A.; Nuttall, W.; Kazantzis, N., Sankey-Diagram-based insights into the hydrogen economy of today. *International Journal of Hydrogen Energy* 2016, *41* (19), 7744-7753.

3. Nagaoka, K.; Eboshi, T.; Takeishi, Y.; Tasaki, R.; Honda, K.; Imamura, K.; Sato, K., Carbon-free H_2 production from ammonia triggered at room temperature with an acidic $RuO_2/\gamma\text{-}Al_2O_3$ catalyst. *Science Advances* 2017, *3* (4), e1602747.

4. Licht, S.; Cui, B.; Wang, B.; Li, F.-F.; Lau, J.; Liu, S., Ammonia synthesis by N_2 and steam electrolysis in molten hydroxide suspensions of nanoscale Fe_2O_3. *Science* 2014, *345* (6197), 637-640.

5. Babson, D. M.; Bellman, K.; Prakash, S.; Fennell, D. E., Anaerobic digestion for methane generation and ammonia reforming for hydrogen production: A thermodynamic energy balance of a model system to demonstrate net energy feasibility. *Biomass and Bioenergy* 2013, *56*, 493-505.

6. Chen, J. G.; Crooks, R. M.; Seefeldt, L. C.; Bren, K. L.; Bullock, R. M.; Darensbourg, M. Y.; Holland, P. L.; Hoffman, B.; Janik, M. J.; Jones, A. K.; Kanatzidis, M. G.; King, P.; Lancaster, K. M.; Lymar, S. V.; Pfromm, P.; Schneider, W. F.; Schrock, R. R., Beyond fossil fuel–driven nitrogen transformations. *Science* 2018, *360* (6391), eaar6611.

7. Andrussow, L., Über die schnell verlaufenden katalytischen Prozesse in strömenden Gasen und die Ammoniak-Oxydation (V). *Berichte der deutschen chemischen Gesellschaft (A and B Series)* 1927, *60* (8), 2005-2018.

8. Kröcher, O.; Elsener, M., Hydrolysis and oxidation of gaseous HCN over heterogeneous catalysts. *Applied Catalysis B: Environmental* 2009, *92* (1), 75-89.

9. Yan, L.; Tian, S.; Zhou, J.; Yuan, X., Catalytic hydrolysis of gaseous HCN over $Cu\text{–}Ni/\gamma\text{-}Al_2O_3$ catalyst: parameters and conditions. *Frontiers of Environmental Science & Engineering* 2016, *10* (6), 5.

10. Song, Z.; Zhang, Q.; Ning, P.; Wang, Y.; Duan, Y.; Wang, J.; Huang, Z., Catalytic hydrolysis of HCN on ZSM-5 modified by Fe or Nb for HCN removal: surface species and performance. *RSC Advances* 2016, *6* (112), 111389-111397.

11. Heise, G. W.; Foote, H. E., The Production of Ammonia and Formates from Cyanides, Ferrocyanides, and Cyanized Briquets. *Journal of Industrial & Engineering Chemistry* 1920, *12* (4), 331-336.

12. Sulzer, H., Verfahren zur Darstellung von Ammoniak und Ameisensäure aus Kalkstickstoff. *Angew. Chem.* 1912, *25*, 1268-1273.

13. Cyano Compounds, Inorganic. In *Ullmann's Encyclopedia of Industrial Chemistry*, Gail, E., Gos, S., Kulzer, R., Lorösch, J., Rubo, A., Sauer, M., Kellens, R., Reddy, J., Steier, N. and Hasenpusch, W. (2011). Cyano Compounds, Inorganic. In Ullmann's Encyclopedia of Industrial Chemistry, (Ed.). doi:10.1002/14356007.a08_159.pub3.

14. Endter, F., Die technische Synthese von Cyanwasserstoff aus Methan und Ammoniak ohne Zusatz von Sauerstoff. *Chemie Ingenieur Technik* 1958, *30* (5), 305-310.

15. Voigt, C.; Kleinschmit, P.; Walter, E. Process for the production of hydrogen cyanide. US 4,289,741, 1981.

16. Pirie, J. M., The Manufacture of Hydrocyanic Acid by the Andrussow Process. *Platinum Metals Rev.* 1958, *2* (1), 7-11.

17. Denton, W. I.; Bishop, R. B., Production of Acetonitrile and Other Low Molecular Weight Nitriles. *Industrial & Engineering Chemistry* 1953, *45* (2), 282-286.

18. Yi, Y.; Wang, X.; Jafarzadeh, A.; Wang, L.; Liu, P.; He, B.; Yan, J.; Zhang, R.; Zhang, H.; Liu, X.; Guo, H.; Neyts, E. C.; Bogaerts, A., Plasma-Catalytic Ammonia Reforming of Methane over Cu-Based Catalysts for the Production of HCN and H_2 at Reduced Temperature. *ACS Catalysis* 2021, 1765-1773.

19. Lacheen, H. S.; Cordeiro, P. J.; Iglesia, E., Isolation of Rhenium and ReO_x Species within ZSM5 Channels and their Catalytic Function in the Activation of Alkanes and Alkanols. *Chemistry – A European Journal* 2007, *13* (11), 3048-3057.

20. Wu, Y.; Holdren, S.; Zhang, Y.; Oh, S. C.; Tran, D. T.; Emdadi, L.; Lu, Z.; Wang, M.; Woehl, T. J.; Zachariah, M.; Lei, Y.; Liu, D., Quantification of rhenium oxide dispersion on zeolite: Effect of zeolite acidity and mesoporosity. *Journal of Catalysis* 2019, *372*, 128-141.

21. Chen, G.; Liang, T.; Yoo, P.; Fadaeerayeni, S.; Sarnello, E.; Li, T.; Liao, P.; Xiang, Y., Catalytic Light Alkanes Conversion through Anaerobic Ammodehydrogenation. *ACS Catalysis* 2021, *11* (13), 7987-7995.

22. Yokota, Y.; Hashimoto, H.; Yamaguchi, T., Electron beam irradiation of natural zeolites at low and room temperatures. *Ultramicroscopy* 1994, *54* (2), 207-214.

23. Zhang, B.; Lwin, S.; Xiang, S.; Frenkel, A. I.; Wachs, I. E., Tuning the Number of Active Sites and Turnover Frequencies by Surface Modification of Supported $ReO_4/(SiO_2–Al_2O_3)$ Catalysts for Olefin Metathesis. *ACS Catalysis* 2021, *11* (4), 2412-2421.

24. Ma, L.; Zou, X., Cooperative catalysis of metal and acid functions in Re-HZSM-5 catalysts for ethane dehydroaromatization. *Applied Catalysis B: Environmental* 2019, *243*, 703-710.

25. Yan, B., et al., Dry Reforming of Ethane and Butane with CO_2 over $PtNi/CeO_2$ Bimetallic Catalysts. ACS Catalysis, 2016: p. 7283-7292.

26. Porosoff, M.D., et al., Identifying Different Types of Catalysts for CO_2 Reduction by Ethane through Dry Reforming and Oxidative Dehydrogenation. Angew Chem Int Ed Engl, 2015. 54(51): p. 15501-5.

27. Kokka, A., et al., Hydrogen production via steam reforming of propane over supported metal catalysts. International Journal of Hydrogen Energy, 2020. 45(29): p. 14849-14866.

28. Siahvashi, A. and A.A. Adesina, Hydrogen production via propane dry reforming: Carbon deposition and reaction-deactivation study. International Journal of Hydrogen Energy, 2018. 43(36): p. 17195-17204.

29. Arvaneh, R., et al., Effects of Ce, La, Cu, and Fe promoters on $Ni/MgAl_2O_4$ catalysts in steam reforming of propane. Korean Journal of Chemical Engineering, 2019. 36(7): p. 1033-1041.

30. Azizzadeh Fard, A., et al., Propane steam reforming over promoted $Ni–Ce/MgAl_2O_4$ catalysts: Effects of Ce promoter on the catalyst performance using developed CCD model. International Journal of Hydrogen Energy, 2019. 44(39): p. 21607-21622.

31. Barzegari, F., et al., The Influence of Lanthanide on $NiO-MgO-SiO_2$ Catalysts for Syngas Production via Propane Steam Reforming. Molecular Catalysis, 2021. 499.

32. Zhao, B., et al., $LaFe_{0.9}Ni_{0.1}O_3$ perovskite catalyst with enhanced activity and coke-resistance for dry reforming of ethane. Journal of Catalysis, 2018. 358: p. 168-178.

33. Do, J.Y., et al., Synthesis and characterization of $Ni_{2-x}Pd_xMnO_4/\gamma-Al_2O_3$ catalysts for hydrogen production via propane steam reforming. Chemical Engineering Journal, 2018. 334: p. 1668-1678.

34. Song, Y., Y. He, and S. Laursen, Controlling Selectivity and Stability in the Hydrocarbon Wet-Reforming Reaction Using Well-Defined Ni + Ga Intermetallic Compound Catalysts. ACS Catalysis, 2020. 10(16): p. 8968-8980.

35. Duan, X., et al., Understanding Co-Mo Catalyzed Ammonia Decomposition: Influence of Calcination Atmosphere and Identification of Active Phase. ChemCatChem, 2016. 8(5): p. 938-945.

36. Podila, S., et al., Hydrogen production by ammonia decomposition using high surface area Mo_2N and Co_3Mo_3N catalysts. Catalysis Science & Technology, 2016. 6(5): p. 1496-1506.

37. Yan, H., et al., Promoted Multimetal Oxide Catalysts for the Generation of Hydrogen via Ammonia Decomposition. The Journal of Physical Chemistry C, 2016. 120(14): p. 7685-7696.

38. Varisli, D. and N.G. Kaykac, CO_x free hydrogen production over cobalt incorporated silicate structured mesoporous catalysts. Applied Catalysis B: Environmental, 2012. 127: p. 389-398.

39. Varisli, D. and N.G. Kaykac, Hydrogen from ammonia over cobalt incorporated silicate structured catalysts prepared using different cobalt salts. International Journal of Hydrogen Energy, 2016. 41(14): p. 5955-5968.

40. Czekajło, Ł. and Z. Lendzion-Bieluń, Effect of preparation conditions and promoters on the structure and activity of the ammonia decomposition reaction catalyst based on nanocrystalline cobalt. Chemical Engineering Journal, 2016. 289: p. 254-260.

41. Podila, S., et al., Hydrogen production by ammonia decomposition using Co catalyst supported on Mg mixed oxide systems. International Journal of Hydrogen Energy, 2015. 40(45): p. 15411-15422.

42. Podila, S., et al., Hydrogen generation by ammonia decomposition using $Co/MgO–La_2O_3$ catalyst: Influence of support calcination atmosphere. Journal of Molecular Catalysis A: Chemical, 2016. 414: p. 130-139.

43. Gu, Y.-Q., et al., Transition metal nanoparticles dispersed in an alumina matrix as active and stable catalysts for CO_x-free hydrogen production from ammonia. Journal of Materials Chemistry A, 2015. 3(33): p. 17172-17180.

44. Liu, H., et al., Preparation, characterization and activities of the nano-sized Ni/SBA-15 catalyst for producing CO_x-free hydrogen from ammonia. Applied Catalysis A: General, 2008. 337(2): p. 138-147.

45. Zheng, W., et al., Effects of CeO_2 addition on Ni/Al_2O_3 catalysts for the reaction of ammonia decomposition to hydrogen. Applied Catalysis B: Environmental, 2008. 80(1-2): p. 98-105.

46. Feyen, M., et al., High-temperature stable, iron-based core-shell catalysts for ammonia decomposition. Chemistry, 2011. 17(2): p. 598-605.

47. Lu A-H, et al., Spatially and Size Selective Synthesis of Fe-Based Nanoparticles on Ordered Mesoporous Supports as Highly Active and Stable Catalysts for Ammonia Decomposition. J Am Chem Soc, 2010. 132: p. 14152–14162.

48. Zhang, J., et al., Commercial Fe- or Co-containing carbon nanotubes as catalysts for NH_3 decomposition. Chem Commun (Camb), 2007(19): p. 1916-8.

49. Zheng, W., et al., Experimental and theoretical investigation of molybdenum carbide and nitride as catalysts for ammonia decomposition. J Am Chem Soc, 2013. 135(9): p. 3458-64.

50. Zhang J, et al., Individual Fe-Co Alloy Nanoparticles on Carbon Nanotubes: Structural and Catalytic Properties. Nano Letters, 2008. 8: p. 2738–2743.

51. Lorenzut, B., et al., FeMo-based catalysts for H_2 production by NH3 decomposition. Applied Catalysis B: Environmental, 2012. 125: p. 409-417.

52. Duan, X., et al., Tuning the size and shape of Fe nanoparticles on carbon nanofibers for catalytic ammonia decomposition. Applied Catalysis B: Environmental, 2011. 101(3-4): p. 189-196.

53. Ji, J., et al., Towards an efficient CoMo/γ-Al_2O_3 catalyst using metal amine metallate as an active phase precursor: Enhanced hydrogen production by ammonia decomposition. International Journal of Hydrogen Energy, 2014. 39(24): p. 12490-12498.

54. Kirste, K.G., et al., XAS investigation of silica aerogel supported cobalt rhenium catalysts for ammonia decomposition. Phys Chem Chem Phys, 2020. 22(34): p. 18932-18949.

55. Le, T.A., et al., Ru-supported lanthania-ceria composite as an efficient catalyst for CO_x-free H_2 production from ammonia decomposition. Applied Catalysis B: Environmental, 2021. 285.

56. Lucentini, I., A. Casanovas, and J. Llorca, Catalytic ammonia decomposition for hydrogen production on Ni, Ru and Ni Ru supported on CeO_2. International Journal of Hydrogen Energy, 2019. 44(25): p. 12693-12707.

CHAPTER III

AMMONIA-ASSITED SELECTIVE LIGHT ALKANE CONVERSION OVER INTERMETALLIC NI_3GAC_X CATALYSTS PREPARED USING OXALATE SYNTHESIS ROUTE

This chapter is adopted from an under-preparation article: Siavash Fadaeerayeni, Hossein Toghiani, Yizhi Xiang, Ammonia-assisted selective light alkane conversion over Ni_3GaC_x intermetallic compound.

3.1 Introduction

The fact that hydrogen is a clean and versatile fuel offers an attractive carbon-free source of energy and leverages the U.S. economy toward long-term sustainable economic growth. At an industrial scale, hydrogen production is mostly relying on methane steam reforming producing stoichiometric amounts of carbon oxides (CO and CO_2), which imposes economic and environmental concerns. To mitigate the issue, we propose NH_3 assisted anaerobic reforming of natural gas liquids (ethane and propane) as an alternative approach to produce CO_x free hydrogen. In the previous chapter, we have shown that atomically dispersed Re-oxo grafted into Al_f of the HZSM-5 zeolite are highly active and stable for the ammonia reforming of ethane and propane at temperatures comparable to steam reforming ≤ 650 °C. With regards to the high price of Re as a precious metal, it is demanding to find an alternative cheap non-noble based catalyst for this process. Ni as the most commonly used metal for steam reforming could be a wise choice. However, Ni based catalysts are suffering from coke deposition due to the polymerization of surface carbon. To alleviate the issue of high surface reactivity of nickel, the addition of secondary metal is proposed to improve the surface and bulk structure through the formation of intermetallic compounds. Different from alloys, these multi-compound materials offer well-defined crystalline structures with fixed atom positions arising from strong electronic/ionic interaction between its constituents [1, 2]. Moreover, computational studies revealed that a combination of a group of Ni transition metals and a post-transition P-orbital rich compound of similar size (Ga, Sn, In, Ge, Al) promote the orbital overlap and modify the bulk structure, resulting in improved surface reactivity and catalytic performance [3]. In this regard, Ni+Ga intermetallic compound has been received considerable attention in several reactions including, but not limited to, alkane dehydrogenation, propane wet reforming, and CO_2 reduction [4-9]. Our group also reported that the presence of intermetallic Ni_3Ga compound in Ni/Ga supported HZSM-5 catalyst inhibits aggressive C-C bond cleavage and hydrogenolysis in ethane aromatization, therefore significantly improved stability and aromatics selectivity compared to the Ni/HZSM-5 catalyst [10]. However, since the process of IMC synthesis is governed by bulk thermal diffusion of constituent metals, besides the importance of atmosphere, temperature, and initial composition, surface property and bulk composition of ultimate material may also be kinetically influenced by the intimacy of metal components during the thermal diffusion (annealing) processes.

Several approaches are adopted to optimize the atomic scale mixing of constituent metals in Ni/Ga intermetallic compounds. Recently, Young et. al. synthesized A NiMgGa intermetallic compound through layered double hydroxide method which was successfully tested in dry reforming of methane (DRM) showing promising stability in high CH_4 and CO_2 conversion [11]. The same synthesis approach utilized by Li et al. also demonstrates improved catalytic performance in the selective hydrogenation of phenylacetylene to styrene[12]. Torelli et. al.

successfully utilized Ni/Ga IMC films prepared by drop-casting in electrocatalytic reduction of CO_2 to C_2 products such as ethylene and ethane [13]. A Ni_5Ga_3 IMC was also developed through hydrotalcite-like compound (HTlc) precursors. The enhanced catalytic performance in CO_2 hydrogenation to methanol was observed which is assigned to the production of smaller crystal size and stabilized structure [14]. Kai et al prepared NiGa IMC using non-aqueous wet-chemical synthesis applying organometallic precursors which proved improved catalytic performance in selective semi hydrogenation of alkynes to alkenes [15]. However, both impregnation and layered double hydroxide as the most frequently used methods for synthesis of NiGa IMC may result in the formation of off-stochiometric IMC along with other segregated phases.

Here, in search of a novel, simple efficient, and scalable synthesis method, we suggest preparing the IMC from Metal-Organic Framework (MOF) precursor synthesized via the oxalate route. We believe that through this synthesis approach, oxalate anions coordinate with the transition metals to create a polymer-like structure, which forms mixed-metal-oxalate units upon coprecipitation [16]. Then, these entities decompose to mixed-metal particles upon heating in H_2 at mild temperature (350-400 °C), which finally leads to a well-defined IMC under heating at high temperature ($>$ 600 °C) annealing in Ar. Starting from a MOF precursor with a matrix of high proximity metal compounds, we expect that the final IMC should be of more phase pure and less segregated moieties compared to sampled prepared by more traditionally used synthesis routes. Here, Ni/Ga IMC with three Ni to Ga ratios was synthesized using MOF precursor and the catalytic performance in ammonia assisted ethane reforming is evaluated. Moreover, the structure reactivity relationship is investigated through several characterization methods to reveal the effect of metal function on stability, activity, and selectivity of the catalyst in CO_x free H_2 formation through ammonia assisted ethane reforming.

3.2 Experimental

3.2.1 Catalyst Preparation

Ni and Ga monometallic, as well as Ni/Ga intermetallic compounds with the various molar ratios, were prepared by oxalate method. Typically, according to the given molar ratio of the final catalyst, metal salts (metal nitrate in this case) were dissolved in isopropyl alcohol in a beaker to get a final solution of approximately 0.14 M. Then, oxalic acid ($H_2C_2O_4$) as the oxalate source was also dissolved in isopropyl alcohol in a second beaker. The amount of oxalic acid was 20% extra stochiometric required for consuming all the metal cation in solution to make sure the metal oxalate formation is not limited by oxalate concentration. The metal salt precursor (beaker 1) was then poured into the oxalic acid solution (beaker 2) and kept under stirring for 15 mins at room temperature. Afterward, the resulting solution was divided into half and one portion was left at room temperature to age for 24 h. The other half was transferred to an autoclave for solvothermal synthesis at the temperature of 100 °C and under autogenic pressure for 24 hr. The resulting solution from both methods was centrifuged at 4000 rpm and dried in the oven at 100 °C for 24 h. Before catalytic testing, the oxalate was decomposed in situ in 100 ml/min 10% H_2 (balanced in Ar) at 750 °C for 2 h and was annealed in pure Ar at temperature 650-750 °C for different times (depending on the experiment). For Ni and Ga monometallic catalyst, the same method was used except in the case of Ga we also added a small amount of Magnesium nitrate (molar ratio of Ga/Mg:20/1) into the initial Ga precursor to disperse Ga within the Mg matrix to increase the activity of final catalyst.

3.2.2 Catalytic Performance Evaluation

The prepared samples were tested in a home-built set-up connected to an online Agilent 5973 mass spectrometer (MS). For each test, the desired amount of catalyst (mixed with 1 g silica sand) was loaded into a quartz reactor with a volume of 2 ml (i.d., Φ = 1/2"). After in situ oxalate decomposition and annealing, explained in the previous section, the reactor temperature was set to the reaction temperature. Then the spectra of Ar and the feed (by-pass) consisting of C_2H_6, Ar, and NH_3 with a molar flow ratio of 1/1/2 were collected for mass spectrometer calibration and used as a reference for the calculation of catalytic performance. The reactions were performed at 650 °C under atmospheric pressure at a gas hourly space velocity (GHSV) of 24000 h^{-1}. The reactor effluent was measured by an online Agilent 5973 mass spectrometer (equipped with MS Sensor 2.0 software, Diablo Analytical, Inc.).

3.2.3 Characterization

The XRD patterns of the catalysts were measured by the Rigaku Ultima III X-ray Diffraction System with Cu Kα radiation (154.06 pm, 40 kV, and 44 mA). Diffraction spectra were collected at the scanning rate of 5° min^{-1} in the range of 2θ from 10°-80°.

Transmission electron microscopy (TEM) images and STEM-EDX chemical mapping of the activated catalysts were obtained using a JEOL 2100TEM (operating at 200 kV). A portion of the high-angle annular dark-field STEM imaging and EDX was performed using a JEOL NeoARM operating at 200 kV.

Hydrogen temperature-programmed decomposition (H_2-TP_{Dec}) of MOF precursors was recorded in the aforementioned home-built set-up and CH_4 (m/z = 16), H_2O (m/z = 18), CO (m/z = 28), and CO_2 (m/z = 44) signals was monitored using the same online Agilent 5973 mass spectrometer. Specifically, 150 mg of sample was placed in the reactor and H_2-TPDec was performed by increasing the temperature of the samples from 50 - 750 °C (ramp rate: 10 °C/min) under 10% H_2 in Ar (40 ml/min). Before experiments, MS was calibrated for the signals of CO, CO_2, and CH_4. The H_2O was recorded by MS but discussed qualitatively in the text.

Selected samples after the reaction were characterized by Temperature-Programed Oxidation (TPO) to quantify the amounts of coke deposition. The TPO was performed in-situ in the same aforementioned reactor by increasing the reactor temperature from 50-650 °C (ramp rate: 10 °C/min) in 20% O_2 in Ar (40 ml/min). The molar specific outlet flow of CO_2 during the TPO was quantified based on the calibration of MS using a mixture of 2.5 % CO_2 in Ar.

3.3 Results and discussion

3.3.1 Effect of Annealing Condition

Considering that reforming is a structure-sensitive reaction, in addition to the surface and bulk composition of the intermetallic compound, the crystalline size and structure significantly influence the catalytic performance. IMC structure could be significantly altered during the annealing process in which the diffusion of metal compounds into the IMC lattice takes place [17]. Therefore, careful consideration of the factors affecting the annealing process should be of utmost importance. In this regard, we started with investigating the effect of annealing temperature on the catalytic performance of Ni/Ga IMC in ammonia assisted light alkane conversion. The Ni/Ga IMC with various Ni to Ga ratios was annealed at temperatures 650 and 750 °C. It is noteworthy to mention according to thermodynamics data formation of Ni/Ga IMC phase within the given temperature range (650-750 °C) is not thermodynamically limited [18].

The result of the performance test has shown in figure 3.1. In this set of experiments, all the samples are reduced at 750 °C for 2 h followed by annealing for 30 min in the given temperatures.

All samples show high selectivity to HCN (above 80% for low temperature annealed samples and above 60% for high temperature). However, regardless of Ni to Ga ratio, samples annealed at 650 °C show higher activity for ethane conversion and more selectivity to HCN (figure

3.1.a & b) at comparable stability (figure 3.1.d) as compared to those annealed at a higher temperature which is more selective to C_2H_4. The only exception is the Ni/Ga with a molar ratio of 3/1 which shows comparable selectivity to HCN for both temperatures. From figure 1.3 c, annealing temperature also has a significant effect on the formation rate of HCN. For all the Ni to Ga ratios, the lower annealing temperature is in favor of CN bond linkage and HCN formation rate which is our desired reaction pathway. Considering this result, we chose 650 °C as the preferred annealing temperature for the rest of the experiments.

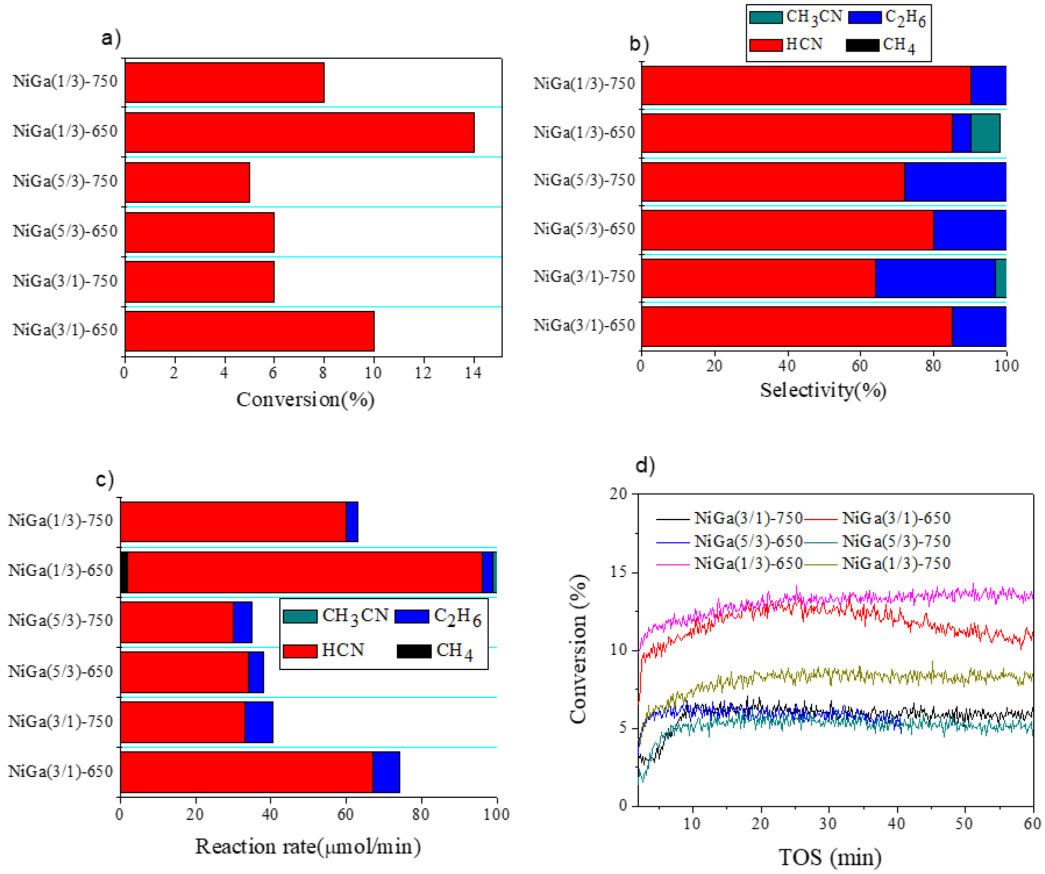

Figure 3.1 Effect of annealing temperature on catalytic performance for various Ni to Ga ratios; a) conversion, b) carbon selectivity, c) reaction rate, d) conversion with TOS

Reactions were performed at T = 650 °C, P = 1 atm, 50 mg catalyst, Total flow =40 mL/min, $NH_3/C_2H_6/Ar=2/1/1$.

The effect of annealing time on the catalytic performance of NiGa IMC with various Ni to Ga ratios is also studied and the results are shown in Figures 3.2 and 3.3. In these experiments, the NiGa IMC with molar ratio of Ni to Ga of 1/1 was selected to balance the effect of Ni and Ga. Moreover, all these samples are annealed at 650 °C for the given time depending on each experiment. While increasing the annealing time does not have a significant effect on selectivity, the remarkable increase in the production rate of HCN was observed for prolonged annealed samples which is due to the higher activity of these samples in ethane conversion (figure 3.3 and 3.2a). The results of the long-term stability of samples show a slight deactivation of samples prepared with a longer annealing time (figure 3.2a). Nonetheless, all the samples have demonstrated comparable stability. This result combined with the result of the previous section suggests that annealing at lower temperature with prolonged annealing time is in favor of C-N bond formation. This may be because, at lower temperatures, the process of diffusion of metal compound and IMC formation is kinetically slower compared to higher temperatures and needs a longer time to reach the final structure. However, proof of such speculation needs further characterization.

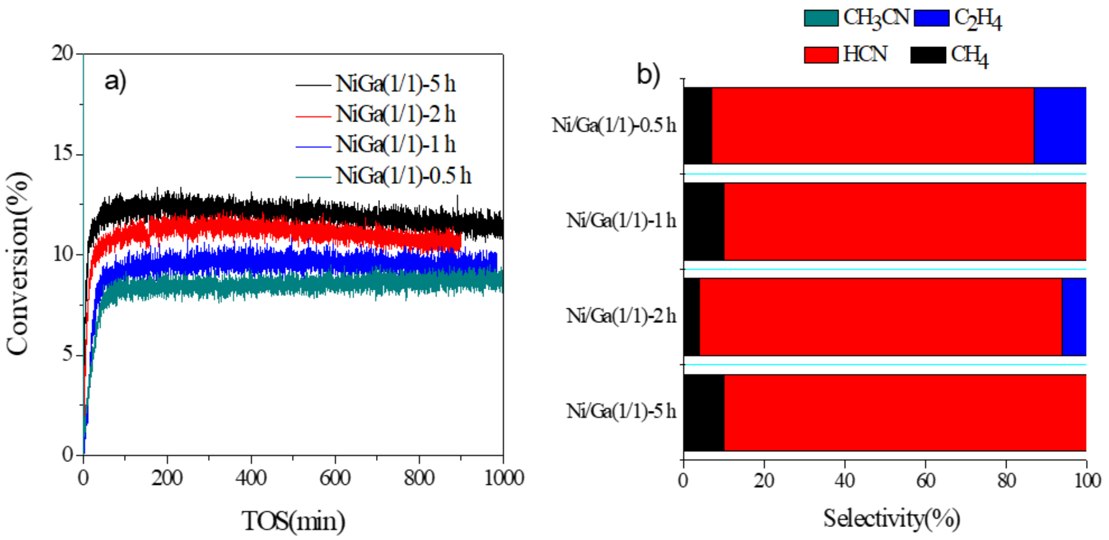

Figure 3.2 Influence of annealing time on a) carbon conversion, b) product selectivity in ammonia assisted ethane conversion over NiGa (1/1) catalyst.

Reactions were performed at T = 650 °C, P = 1 atm, 50 mg cat., Total flow =40 mL/min, $NH_3/C_2H_6/Ar=2/1/1$. All samples are reduced at 750 °C for 2 h before annealing.

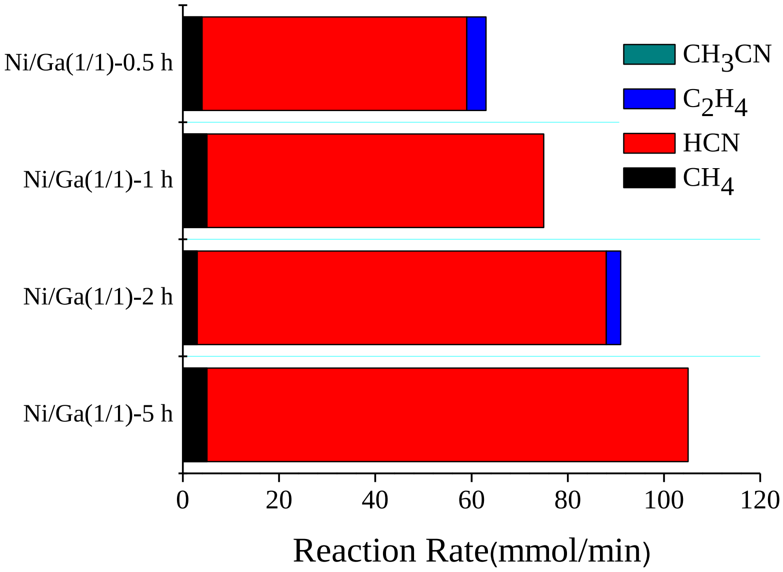

Figure 3.3 Influence of annealing time on product formation rate in ammonia assisted ethane conversion over NiGa (1/1) catalyst.

Reaction condition is the same as Figure 3.2.

3.3.2 Influence of Ni to Ga Ratio

Based on the result of the previous section, the samples studied in this section were annealed at 650 °C and the annealing time was selected 16 h to minimize the influence of the slow kinetic in formation of IMC final phase. In addition, here we only present the result of the samples prepared using a solvothermal method as these samples generally show more activity and are expected to have a more well-defined crystalline structure due to the synthesis condition.

The catalytic performance of bimetallic NiGa catalysts is shown in figure 3.4 and compared with monometallic Ni and Ga catalysts. From figure 3.4a, while Ni monometallic catalysts significantly deactivate during 10 h time on stream and Ga monometallic catalyst shows negligible activity, bimetallic catalysts outperform their monometallic counterparts in terms of stability and long term activity.

According to figure 3.4b, all Ni based catalysts are highly selective for HCN formation while Ga monometallic catalysts mainly promote ethane dehydrogenation. For bimetallic catalysts, carbon conversion was increased by increasing Ga to Ni ratio, while comparable selectivity to HCN (> 95%) was observed. Another interesting observation is that for bimetallic catalysts there is a long induction period (figure 3.5). Specifically, in case of NiGa(3/1), the carbon conversion is negligible during the first 10 min, after which it slowly starts increasing till it reaches the steady-state after almost 2 h. Early-stage behavior of Ga rich samples, NiGa(1/1) and NiGa(1/3) shows different behavior. Initially, there is a jump in conversion and then the activity remains constant in case of NiGa(1/1) or drops a little bit for NiGa(1/3). Later, it again slowly increases to reach the steady state. Nonetheless, overall, by increasing Ga to Ni ratio in bimetallic catalyst, the induction period decreases. We expect that this long induction period might be due to significant reconstruction of the active phase upon exposure to the reaction mixture.

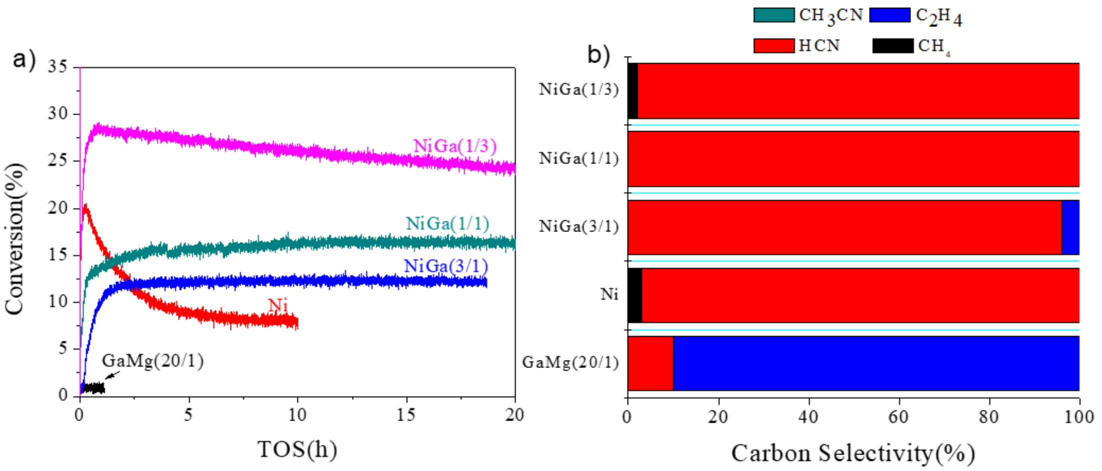

Figure 3.4 Influence of metal function on a) long-term conversion, and b) product selectivity.

Reactions were performed at T = 650 °C, P = 1 atm, 150 mg cat., Total flow =120 mL/min, $NH_3/C_2H_6/Ar=2/1/1$.

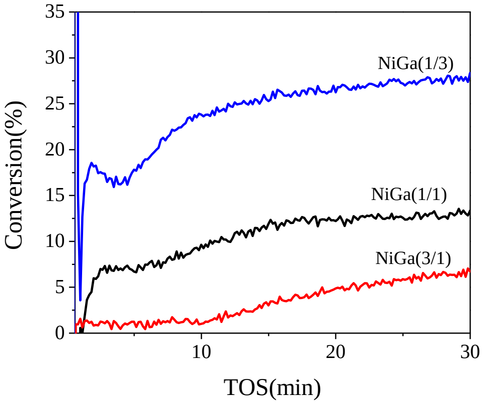

Figure 3.5 Early-stage catalytic activity for bimetallic Ni/Ga catalyst with different molar ratios of Ni to Ga.

Reaction conditions are the same as in figure 3.4.

Figure 3.6 shows the reaction rate of various species with time for all the samples. In terms of bimetallic samples, it is obvious that the main products are H_2, HCN, and N_2 indicating HCN formation and NH_3 decomposition are the main reaction pathways. On the other hand, a much lower rate of N_2 compared to HCN indicate that C-C bond breaking and C-N bond linkage are favored on bimetallic samples compared to ammonia decomposition. It is also obvious that despite the higher activity of NiGa (1/3) sample, it produces less N_2 (almost half) compare to Ni rich sample NiGa (3/1). This indicates that Ni rich samples are more active for NH_3 decomposition compared to Ga rich samples. As another interesting observation, with increasing the Ga content in bimetallic samples while the activity for HCN formation increases the stability of catalyst decreases evidenced with slow deactivation of NiGa(1/3) with time on stream. This difference in catalytic performance may be originated from various structures of Ni and Ga rich bimetallic samples. Moreover, no activity of the catalyst for CH_3CN formation is due to the absence of Bronsted acid sites which are required for acetonitrile formation.

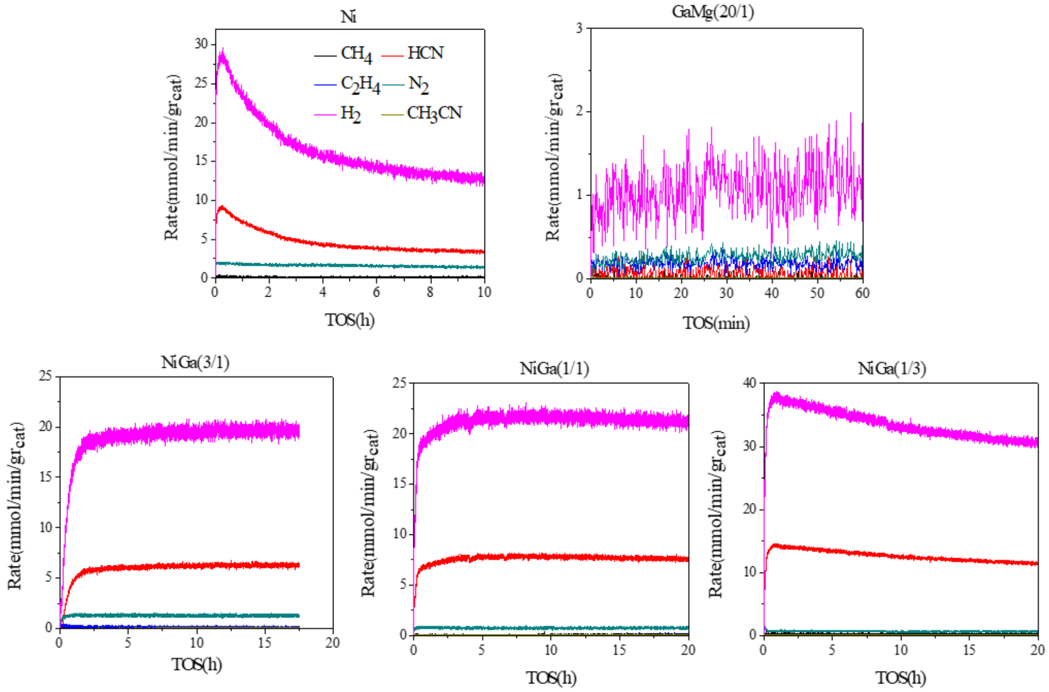

Figure 3.6 Influence of metal function on product formation rate in ammonia assisted ethane reforming over bimetallic Ni/Ga as well as monometallic Ni and Ga catalysts.

Reaction conditions are the same as in figure 3.4.

3.3.3 Catalyst Characterization

The results of Temperature Program oxidation (TPO) profile of monometallic Ni as well as bimetallic NiGa (3/1) and NiGa (1/3) are shown in figure 3.7. As expected from sharp activity drop of monometallic Ni catalysts significant coke deposition was observed for this catalyst. In case of bimetallic catalysts, a negligible peak of CO_2 was observed. Although this was not surprising for the NiGa (3/1) sample as it shows remarkable stability during 20 h time on stream, it was not expected for NiGa (1/3) which slowly deactivates with time of stream. This result shows that coke formation could not be the reason for the deactivation of Ga-rich IMC. Therefore, we expect that surface/bulk reconstruction of this catalyst during the reaction may be responsible for catalyst deactivation. Interestingly, the maxima of CO_2 peak shifts to higher temperatures for bimetallic samples (450-490 °C) compared to monometallic Ni (~400 °C). This shows that different carbon species should be present for these catalysts. In the case of bimetallic catalysts removal of deposited carbon seems to be more difficult. It may be speculated the carbon in bimetallic catalysts might be of lattice carbon which is more difficult to be removed compared to surface carbon for monometallic Ni, hence requiring higher temperatures for coke oxidation.

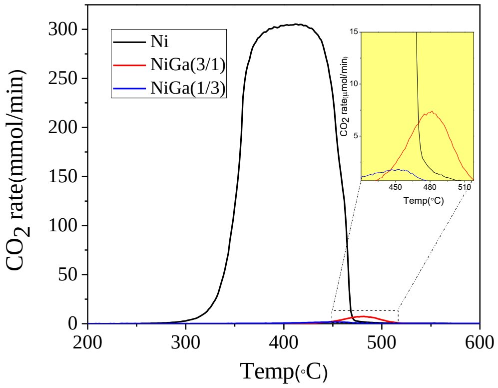

Figure 3.7 Temperature Programmed Oxidation (TPO) of used Ni, NiGa (3/1), and NiGa (1/3).

The result of H_2 temperature program decomposition (H_2-TP_{dec}) of MOF precursor for various samples is shown in figure 3.8. and 3.9. The (co) precipitated metal oxalates need to be thermally decomposed in presence of H_2 to produce active components of intermetallic compounds.

The TPR profiles of $MC_2O_4.xH_2O$ (M: metal cation) mainly consist of two steps. In the first step, crystalline water is removed according to equation 3.1 evidenced by the appearance of a broad peak of H_2O with maxima at almost 250 °C.

$$MC_2O_4.xH_2O \rightarrow MC_2O_4 + xH_2O \qquad (3.1)$$

Following this step, decomposition of oxalate structure starts at a temperature higher than 300 °C. This is realized by emerging CO, CO_2, CH_4, and second H_2O peak. Oxalate decompositions occur according to the two mechanisms mentioned below. Metal oxalate could either directly convert to metal leaving behind 2 molecules of CO_2 (equation 3.2) or can be transformed to metal oxide producing one molecule of CO_2 and CO (equation 3.3). These metal oxides could be further reduced to form metal. This latter is evidenced by emerging the second H_2O peak once CO and CO_2 reach their maxima (equation 3.4).

$$MC_2O_4 \rightarrow 2CO_2 + M \qquad (3.2)$$

$$MC_2O_4 \rightarrow MO + CO + CO_2 \qquad (3.3)$$

$$MO + H_2 \rightarrow M + H_2O \qquad (3.4)$$

In addition to CO, CO_2, and H_2O, with a short delay, a small peak of CH_4 is also observed during the decomposition of the oxalate structure. This could be the product of the reaction of released CO and H_2 over newly reduced Ni sites(Fischer-Tropsch reaction).

As it is shown in figure 3.8, for monometallic Ni, the appearance of only one peak of CO_x (x=1,2) centered at 370 °C in addition to the negligible peak of CO compared to CO_2 indicates that the majority of Ni oxalate decomposes directly to metallic Ni. Likewise, in case of Ga monometallic, one peak of CO_x is observed; however, the intensity of CO ratio is significantly increased compared to Ni monometallic sample indicating the majority of Ga oxalate should be converted to Ga oxide species. The fact that this peak is centered at 330 °C, indicates that Ga should most likely exist in form of Ga_2O_3 since further reduction of Ga needs temperatures higher than 500 °C.

From figure 3.9, for NiGa (3/1) bimetallic catalyst, there is only one peak of CO_x centered at 370 °C with a high ratio of CO_2/CO peak, quite similar to monometallic Ni. More importantly, this sample does not show peak cantered at 330 °C associated with the formation of Ga oxide species. Considering this observation, we conclude that for Ni rich bimetallic sample, Ni may promote the reduction of Ga similar to what is reported before [12].

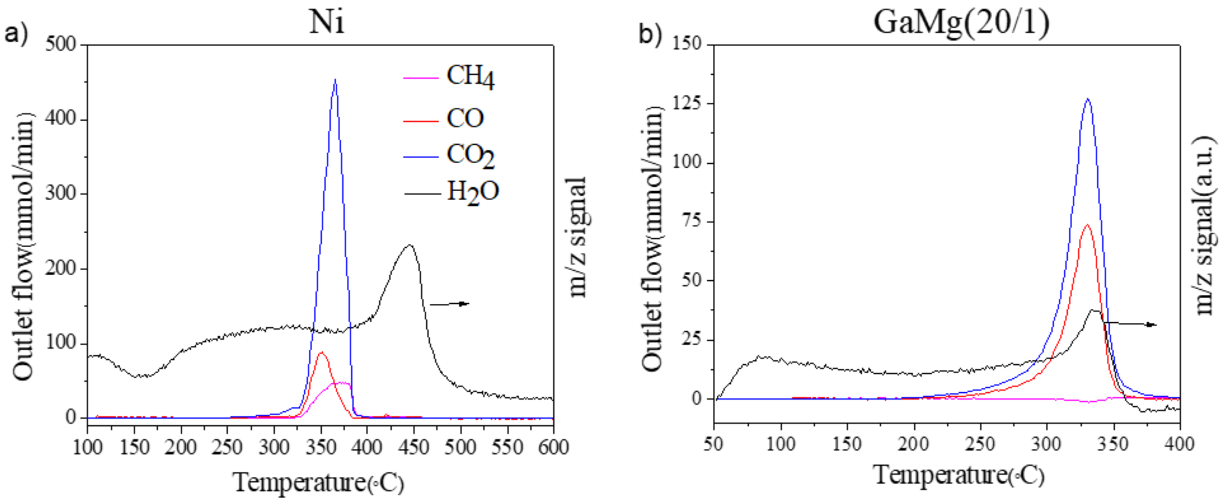

Figure 3.8 H$_2$-Temperature Programmed Decomposition(H$_2$-TPdec) profile of a) Ni, b) GaMg.

Contrary to Ni rich samples, decomposition of oxalate precursor for NiGa (1/1) and NiGa (1/3) samples shows two convoluted peaks centered at 330 and 370 °C. The peak at low and high temperatures resembles the decomposition profile of Ga and Ni monometallic samples, respectively. Another important observation is that with increasing the Ga content in the sample the intensity of peaks located at lower temperatures increase while those at higher temperatures decrease. Therefore, we propose that with increasing Ga in the sample there is more likely to form Ga oxide rather than Ga metallic species. On the other hand, the fact that for Ni rich bimetallic sample, NiGa (3/1), we observed a single peak of CO$_x$, suggests that this sample has better atomic-scale mixing. It is noteworthy to mention that the oxalate precipitation method has been carefully adapted to enhance the perfect atomic-scale mixture of constituent metals to increase the chance of the formation of well-defined intermetallic compounds after annealing.

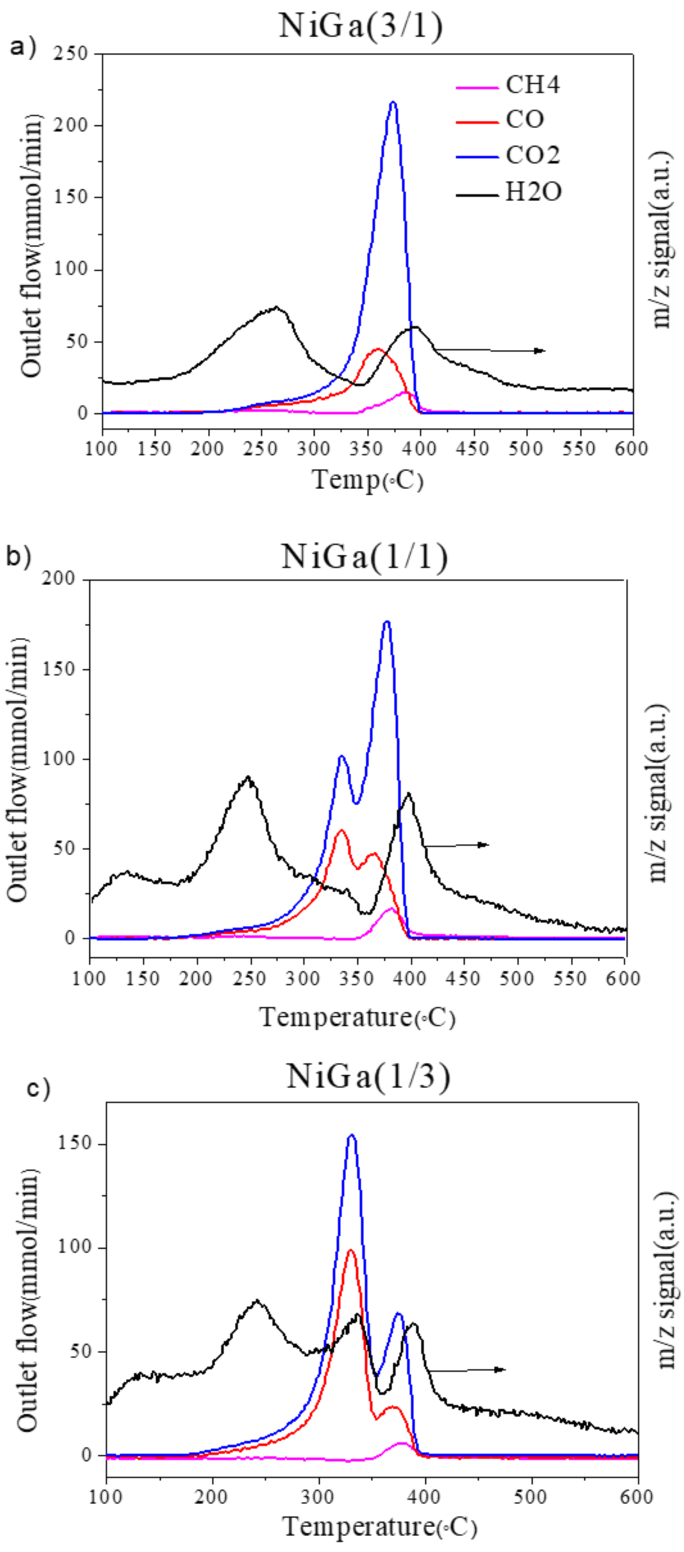

Figure 3.9 H_2-Temperature Programmed Decomposition(H_2-TPdec) profile of a) NiGa (3/1), b) NiGa (1/1), and c) NiGa (1/3).

To further elucidate the catalyst structure, Xray Diffraction patterns (XRD) of bimetallic and monometallic oxalate samples were measured. The XRD spectra of oxalate samples upon aging in autoclave and before decomposition is shown in figure 3.10. All the samples show a pronounced peak of metal oxalate structure indicating oxalate structure is successfully synthesized using the proposed synthesis method. The XRD pattern of these samples after decomposition in H_2 and high temperature annealing in Ar is also depicted in figure 3.11. Spectra of Ni monometallic sample shows a well crystalline structure of metallic nickel. On the other hand, Ga monometallic sample shows an amorphous structure with a low degree of crystallinity; yet the main peaks of Ga_2O_3 could be recognized. This is consistent with the result of the catalytic performance test showing high selectivity for ethane dehydrogenation as Ga_2O_3 is known as an effective catalyst for propane dehydrogenation [19, 20]. This is also confirmed through the result of H_2-TP_{dec} which shows majority of Ga should form Ga_2O_3 structure.

Regarding bimetallic samples, NiGa (3/1) shows a well-defined Ni_3Ga IMC evidenced with three peaks at 2θ of 43.9, 51, and 75.3. However, XRD pattern of NiGa (1/1) catalyst shows presence of Ga_2O_3 and an off stoichiometric Ni_5Ga_3 IMC. With further increase in Ga content for NiGa (1/3), peaks of Ga_2O_3 phase become more pronounced while the formation of a new off stochiometric Ni rich IMC with the formula of $(Ni_{23}Ga_2)_{0.16}$ is also observed. Nonetheless, quantitative analysis of this sample shows the majority of this sample is comprised of Ga_2O_3 phase (~ 93%). This is consistent with the result of H_2-TP_{dec}, suggesting the formation more segregated Ga_2O_3 phase with increasing Ga in the sample. To understand the dynamic change of samples upon exposure to the reaction mixture, XRD pattern of used bimetallic catalysts is shown in figure 3.12. By comparing the spectra of NiGa (3/1) and NiGa (1/1) used samples with the fresh one, it is obvious that these samples retain the initial Ni_3Ga IMC structure, however, the main peaks are shifted to lower angles. This could be realized through the formation of carburized IMC, namely $NiGa_3C_x$. The dynamic formation of $Ni_3GaC_{0.25}$ phase during methane dry reforming is also reported recently [11]. The formation of $NiGa_3C_x$ is also consistent with the long induction period observed for bimetallic catalysts. In our case, the careful analysis of this phase using the data set proposes formation of $NiGa_3C_{0.31}$ species. It is also noteworthy to mention that in the case Ga rich samples, i.e. NiGa (1/1) and NiGa (1/3), Ga_2O_3 related peaks disappear while several new peaks associated with the formation of Gallium nitride was observed. This shows for Ga rich samples, Ga species should undergo phase reconstruction during the reaction condition to form GaN moities upon exposure to NH_3. This could be the reason for the deactivation of and NiGa (1/3) with time.

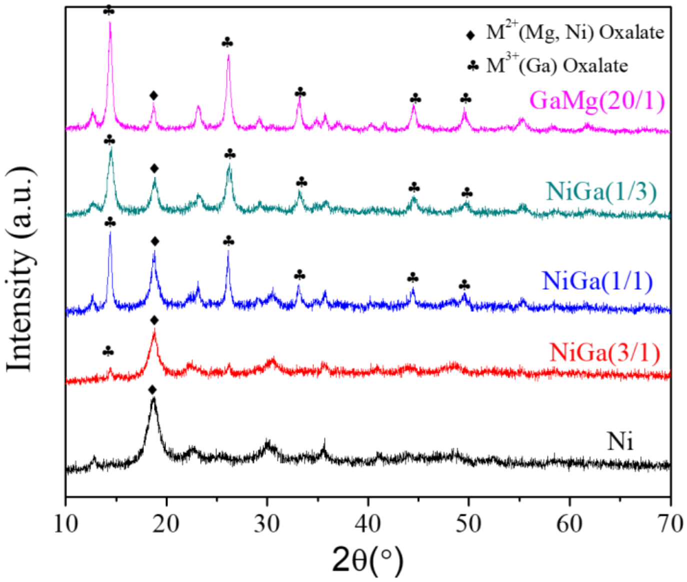

Figure 3.10 XRD pattern of monometallic Ni and Ga as well as bimetallic Ni/Ga samples before oxalate decomposition.

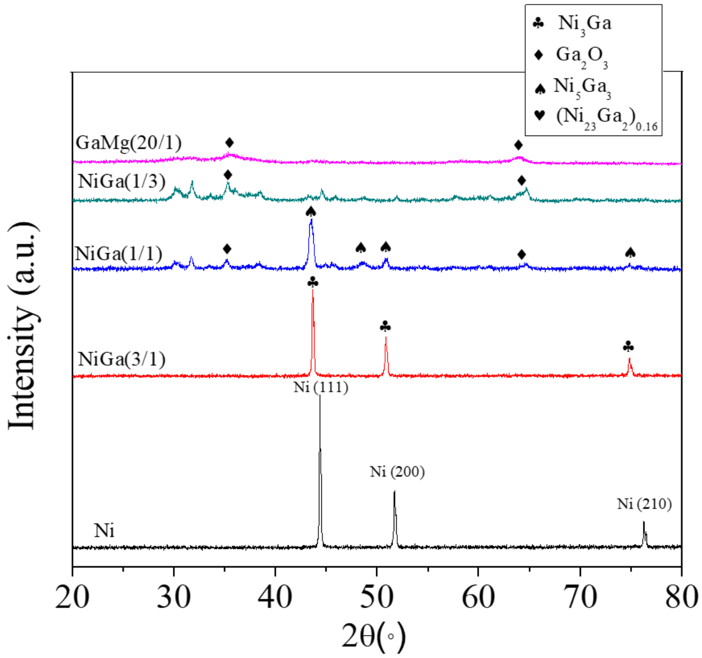

Figure 3.11 XRD pattern of monometallic Ni and Ga and bimetallic Ni/Ga samples after oxalate decomposition and high-temperature annealing

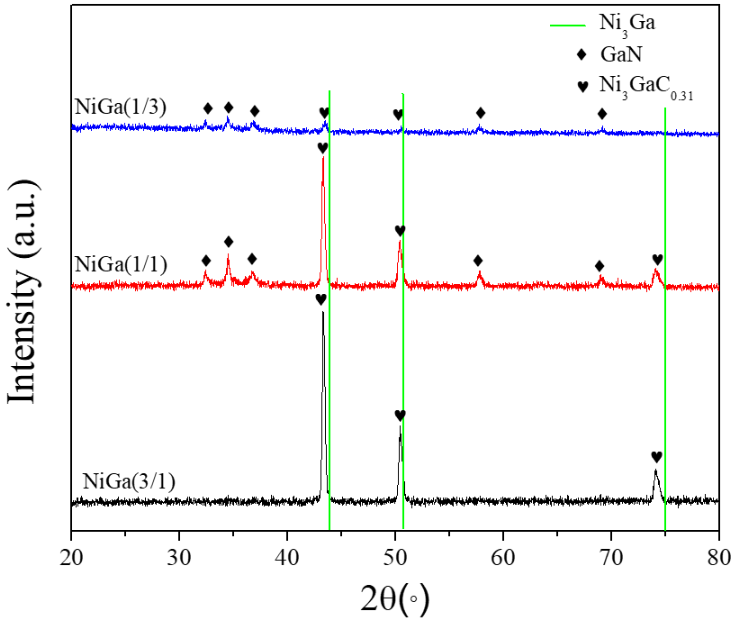

Figure 3.12 XRD pattern of monometallic Ni and Ga and bimetallic Ni/Ga samples after the reaction.

The STEM and elemental mapping of bimetallic catalysts after oxalate decomposition and annealing were also shown in Figures 3.13 to 3.15 NiGa (3/1) catalyst shows the identical distribution of Ga and Ni in the samples which is consistent with the formation of well-defined Ni_3Ga IMC as confirmed with XRD and H_2-TPdec. However, in case of NiGa (1/1) sample, Ni and Ga do not show identical distribution within the sample. This uneven distribution is even more pronounced for NiGa (1/3), in which there is a pronounced correlation between dispersion of Ga and O confirming the formation of Ga_2O_3 phase rather than IMC as supported by XRD and H_2-TP_{dec}. Another interesting finding is that the crystal's shape significantly depends on the Ni to Ga ratio. For example, while NiGa (1/1) has nanorod crystals, the crystals of NiGa (1/3) resemble chips species. This might be translated to higher surface area and could be the origin of higher activity of NiGa (1/3) compared to other samples. The formation of nanorod crystals crystal of Ga_2O_3 is already reported in the literature may further prove that Ga rich samples mostly consist of Ga_2O_3 species [21].

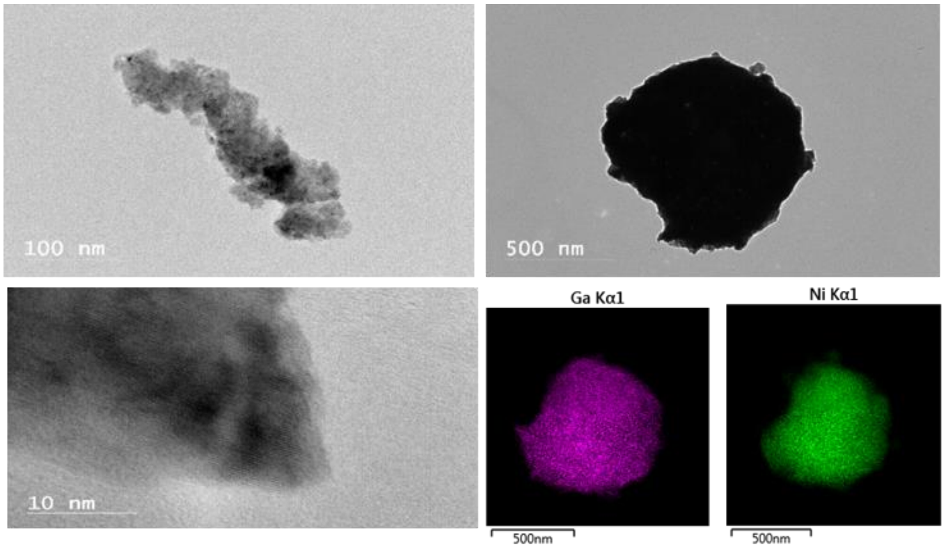

Figure 3.13 STEM image and elemental mapping of Ni/Ga (3/1) after oxalate decomposition and high-temperature annealing

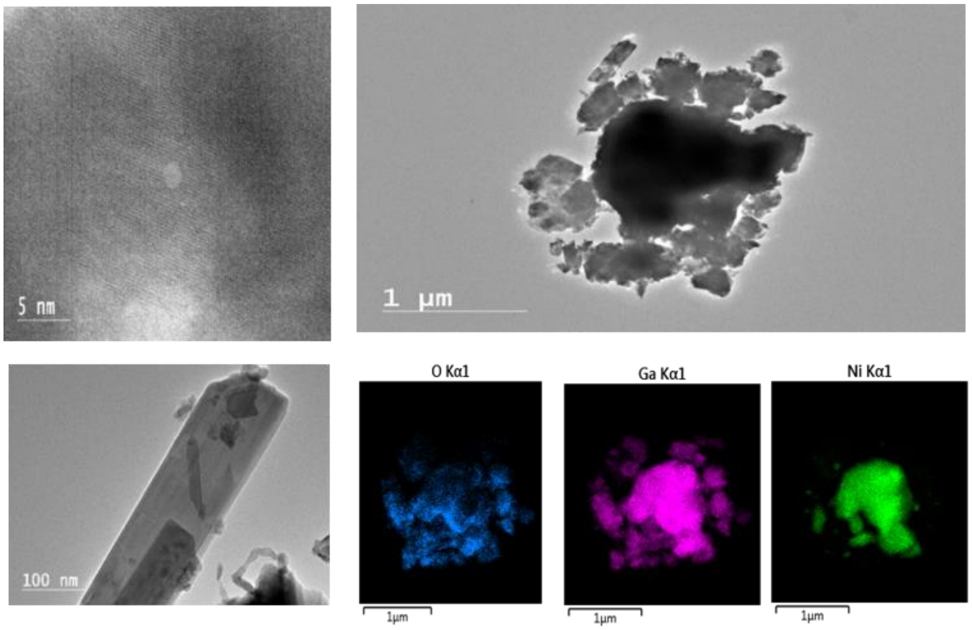

Figure 3.14 STEM image and elemental mapping of Ni/Ga (1/1) after oxalate decomposition and high-temperature annealing

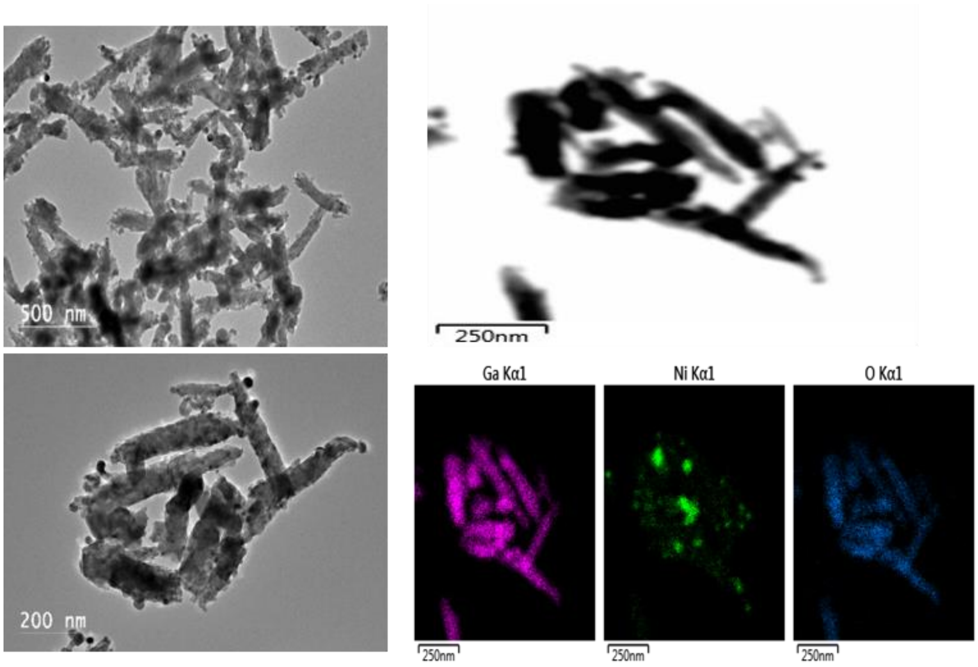

Figure 3.15 STEM image and elemental mapping of Ni/Ga (1/3) after oxalate decomposition and high-temperature annealing

3.4 Conclusion

The performance of NiGa bimetallic compounds prepared by solvothermal method and oxalate precursor was studied in ammonia assisted light alkane conversion. The catalytic performance test has shown that bimetallic catalyst outperforms its monometallic counterparts in terms of activity and stability. While all bimetallic catalysts show high selectivity for C-N bond linkage, stability and activity highly depend on the Ni to Ga ratios. The characterization of catalyst reveals Ni rich sample, i.e., NiGa (3/1), forms well defined Ni_3Ga IMC upon high temperature annealing while increase in the Ga content results in the formation of segregated Ga_2O_3 phase and off stochiometric Ni_xGa_y IMC with low stability. Bimetallic samples undergo dynamic structure change during the reaction forming carburized NiGa IMC phase, namely $NiGa_3C_x$, which might be the reason for the long induction period observed for these catalysts. On the basis of extensive characterization and catalytic performance test, we suggest that $NiGa_3C_{0.31}$ phase should be the stable active site in ammonia assisted ethane conversion.

3.5 References

1. Dasgupta, A. and R.M. Rioux, *Intermetallics in catalysis: An exciting subset of multimetallic catalysts.* Catalysis Today, 2019. 330: p. 2-15.

2. Armbruster, M., R. Schlogl, and Y. Grin, *Intermetallic compounds in heterogeneous catalysis-a quickly developing field.* Sci Technol Adv Mater, 2014. 15(3): p. 034803.

3. Song, Y. and S. Laursen, *Control of surface reactivity towards unsaturated C-C bonds and H over Ni-based intermetallic compounds in semi-hydrogenation of acetylene.* Journal of Catalysis, 2019. 372: p. 151-162.

4. Studt, F., et al., *Discovery of a Ni-Ga catalyst for carbon dioxide reduction to methanol.* Nature Chemistry, 2014. 6(4): p. 320-324.

5. Song, Y., Y. He, and S. Laursen, *Controlling Selectivity and Stability in the Hydrocarbon Wet-Reforming Reaction Using Well-Defined Ni + Ga Intermetallic Compound Catalysts.* ACS Catalysis, 2020. 10(16): p. 8968-8980.

6. He, Y., Y. Song, and S. Laursen, *The Origin of the Special Surface and Catalytic Chemistry of Ga-Rich* Ni_3Ga *in the Direct Dehydrogenation of Ethane.* ACS Catalysis, 2019: p. 10464-10468.

7. Zhou, W., et al., *Efficient selective oxidation of benzyl alcohol with oxygen in a continuous fixed bed reactor over NiGa hydrotalcite derived catalyst.* Applied Catalysis A: General, 2020. 592.

8. Niu, X., L. Wang, and J. Chen, *Improved performance of* SiO_2*-supported* Ni_3Ga *intermetallic compound for deoxygenation of phenolic compounds.* Catalysis Communications, 2020. 140.

9. Sharafutdinov, I., et al., *Intermetallic compounds of Ni and Ga as catalysts for the synthesis of methanol.* Journal of Catalysis, 2014. 320(0): p. 77-88.

10. Fadaeerayeni, S., et al., *Nickel/gallium modified HZSM-5 for ethane aromatization: Influence of metal function on reactivity and stability.* Applied Catalysis A: General, 2020. 601: p. 117629.

11. Kim, K.Y., et al., *Layered Double Hydroxide-Derived Intermetallic* $Ni_3GaC_{0.25}$ *Catalysts for Dry Reforming of Methane.* ACS Catalysis, 2021: p. 11091-11102.

12. Li, C., et al., *Nickel-Gallium Intermetallic Nanocrystal Catalysts in the Semihydrogenation of Phenylacetylene.* ChemCatChem, 2014. 6(3): p. 824-831.

13. Torelli, D.A., et al., *Nickel–Gallium-Catalyzed Electrochemical Reduction of* CO_2 *to Highly Reduced Products at Low Overpotentials.* ACS Catalysis, 2016. 6(3): p. 2100-2104.

14. Men, Y., et al., *Synthesis of Ni_5Ga_3 catalyst by Hydrotalcite-like compound (HTlc) precursors for CO_2 hydrogenation to methanol.* Applied Catalysis B: Environmental, 2020. 275.

15. Schutte, K., et al., *Colloidal nickel/gallium nanoalloys obtained from organometallic precursors in conventional organic solvents and in ionic liquids: noble-metal-free alkyne semihydrogenation catalysts.* Nanoscale, 2014. 6(10): p. 5532-44.

16. Xiang, Y., et al., *Long-Chain Terminal Alcohols through Catalytic CO Hydrogenation.* Journal of the American Chemical Society, 2013. 135(19): p. 7114-7117.

17. A. T. DONALDSON, a.R.D.R., *The Diffusion of Nickel and Gallium in the Inetermetallic Compound NiGa.* Acta Metallurgica, 1976. 24: p. 285-291.

18. Okamoto, H., *Ga-Ni (Gallium-Nickel).* Journal of Phase Equilibria and Diffusion, 2008. 29(3): p. 296-296.

19. Chang, Q.-Y., et al., *Rational Design of Single-Atom-Doped Ga_2O_3 Catalysts for Propane Dehydrogenation: Breaking through Volcano Plot by Lewis Acid–Base Interactions.* ACS Catalysis, 2021. 11(9): p. 5135-5147.

20. Castro-Fernández, P., et al., *Propane Dehydrogenation on Ga_2O_3-Based Catalysts: Contrasting Performance with Coordination Environment and Acidity of Surface Sites.* ACS Catalysis, 2021. 11(2): p. 907-924.

21. Li, X., et al., *Nanorod β-Ga_2O_3 semiconductor modified activated carbon as catalyst for improving power generation of microbial fuel cell.* Journal of Solid State Electrochemistry, 2019. 23(10): p. 2843-2852.

CHAPTER IV

NICKEL/GALLIUM MODIFIED HZSM-5 FOR ETHANE AROMATIZATION: INFLUENCE OF METAL FUNCTION ON REACTIVITY AND STABILITY

This chapter is adopted from a published article: Siavash Fadaeerayeni, Junjun Shan, Erik Sarnello, Haiping Xu, Hui Wang, Jihong Cheng, Tao Li, Hossein Toghiani, Yizhi Xiang, Nickel/gallium modified HZSM-5 for ethane aromatization: Influence of metal function on reactivity and stability, Applied Catalysis A, General 601 (2020) 117629.

4.1 Introduction

The increased supply of shale gas has triggered many interests toward the conversion of natural gas compounds into more valuable petrochemical products. Consequently, the feedstock for steam cracking is shifting from naphtha to ethane (the second-largest component of shale gas). However, the lighter feedstock, ethane, does not lead to the production of heavier products during the steam cracking, which reduced the production of heavier petrochemical “building-blocks”, such as aromatics [1]. As a result, it becomes important to rebalancing the global petrochemicals markets with “on-purpose” technologies using light alkanes as the feedstock [2]. An efficient catalytic system for direct ethane aromatization, therefore, could have far-reaching implications to the global BTX (benzene, toluene, and xylene) market [3, 4].

While several catalytic processes for C_{3+} hydrocarbons aromatization, such as M2-forming [5], Cyclar^{TM} process [6], Aroforming [7], and Z-forming [8], have been developed by the industrial community, a similar process for ethane conversion remains a formidable challenge. Different from C_{3+}-alkanes, which can be converted to aromatics by the ZSM-5 in the H-form (through secondary carbenium formation) [5, 9, 10], the activation of ethane requires an additional metal function either exchanged with the proton of the zeolite or forming nanoparticles/clusters in close proximity with the zeolite [9, 11, 12]. Many efforts have been devoted to ethane aromatization since the 1980s and various metal species, such as Pt, Zn, Ga, Re, and Mo, modified HZSM-5 catalysts have been reported to be active [11-30]. However, a trade-off between activity and selectivity/stability has been found for such a catalytic system, which hampered the industrial applications. According to Hu and coworkers, the bimetallic Ga/Pt modified HSZM-5 catalyst shows higher activity than monometallic Ga, Pt, and Mo based catalysts, but the stability seems decreased (both conversion and selectivity attenuate, with time-on-stream, faster than the monometallic catalysts) [31, 32]. More recently, the catalytic systems for ethane aromatization have also been extensively studied from a more fundamental point of view. For example, Mehdad and Lobo studied the Zn modified HZSM-5 catalyst and suggested that the balance between the number of Zn (II) Lewis acid and the remaining Brønsted acid sites is of great importance to the ethane and ethylene aromatization [33]. Our recent study also revisited the Zn-HZSM-5 catalyst, the influence of acidity on the early-stage reactivity and long term stability were discussed based on the transient kinetics analysis and deactivation kinetics [34, 35]. Additionally, the effect of Al distribution in the MFI framework on the ethane aromatization over the Pt/HZSM-5 catalyst has been investigated by Cheng et al. [36] and the kinetics/mechanism of the ethane aromatization on the Re/HZSM-5 was discussed by Ma and Zou [37]. It might be expected, from the literature, that the metal functions have significant effects on the initial ethane dehydrogenation activity, product selectivity, and stability.

Among different catalysts, Ga modified HZSM-5 exhibits a higher selectivity to BTX and a slower rate of deactivation than the other metals, such as Zn and Pt, modified HZSM-5 catalysts. The Ga/HZSM-5 catalyst has been employed in the UOP/BP's Cyclar^{TM} process for propane/butane aromatization, which produces up to 60 wt% of aromatics yield (a commercial unit of 45,000 BPD was operated in the Middle East from 1999−2013) [6]. However, the activity of the Cyclar catalyst in the ethane aromatization is low [12, 38]. On the other hand, Ni modified HZSM-5 catalyst has not been reported for the ethane aromatization, most probably due to its high rate of coking (Ni-based catalysts have been used for the synthesis of carbon nanotubes from ethane [39]). Nonetheless, Ni-exchanged HZSM-5 has been investigated for the aromatization of C_{3+} alkanes [40-43]. Comparable selectivity to the Ga-ZSM-5 and Zn-ZSM-5 has been found during the pentane aromatization [42]. However, a higher methane selectivity [44] and a faster rate of deactivation [43] were observed during the propane and n-butane aromatization.

While single Ni metal modified ZSM-5 catalyst has been considered "ineffective" in the ethane aromatization, here we will demonstrate a significant bi-metal synergistic effect in the Ni and Ga co-functionalized HZSM-5 for this reaction. The bi-metal Ni/Ga (with 1/1 atomic ratio) modified HZSM-5 shows improved activity or selectivity and stability than the single metal modified HZSM-5 catalysts. Specifically, we are focusing on the influence of metal species chemical composition on the early-stage catalytic activity/selectivity and stability during the ethane aromatization. Therefore, a series of Ni and/or Ga modified HZSM-5 catalysts were prepared through impregnation, and the physicochemical properties of the prepared catalysts were extensively characterized by hydrogen temperature-programmed reduction (H_2-TPR), X-ray powder diffraction (XRD), X-ray photoelectron spectrometers (XPS), X-ray absorption spectroscopy (XAS), scanning transmission electron microscopy (STEM-EDS), and ammonia temperature-programmed desorption (NH_3-TPD). Consequently, the relationships between the chemical properties of the metal species and their reactivity will be discussed based on the early-stage transient results. The deactivation kinetics will be evaluated based on the modified power-law equation model for different catalysts; the effect of chemical composition on the kinetic parameters will be discussed.

4.2 Experimental

4.2.1 Catalyst Preparation

The NH_4-ZSM-5 zeolite (specific area 400 m^2/g, $SiO_2/Al_2O_3=30$) was purchased from Alfa Aesar. The zeolite was pretreated under vacuum (100 mbar) at 120 °C for 12 h to remove the moisture. $Ni(NO_3)_2{\cdot}6H_2O$ and $Ga(NO_3)_3{\cdot}xH_2O$ (trace metals) were purchased from Sigma-Aldrich and were used as obtained. The Ni and Ga modified HZSM-5 catalysts were prepared through incipient wetness co-impregnation. The Ni loadings were fixed at 2 wt% (metal base) and the Ni/Ga atomic ratio was varied. The bi-metal catalysts were noted as Ni_1Ga_x/HZSM-5, in which x represents the relative atomic ratio between Ga to Ni. The monometallic Ni and Ga modified HZSM-5 catalysts were also prepared through incipient wetness impregnation both at 2 wt% metal loading. Experimentally, 2 g of the dried NH_4-ZSM-5 zeolite was impregnated with a 2 ml aqueous solution of $Ni(NO_3)_2{\cdot}6H_2O$ and/or $Ga(NO_3)_3{\cdot}xH_2O$ precursor at room temperature. The samples were kept under ambient conditions for 24 h for aging. Finally, the samples were dried at 70 °C under vacuum overnight and calcined in air at 600 °C for 6 h. The powder sample was formed through tablet press, then crushed and sieved to obtain a size fraction between 125 and 250 μm for characterization and catalytic performance investigations.

4.2.2 Catalyst Characterization.

Ammonia temperature-programmed desorption (NH_3-TPD) experiment was performed on the Micrometrics AutoChem 2910 equipped with an external online mass spectrometer. Before each experiment, the sample (0.1 g) was first activated in 10% H_2/Ar at 650 °C for 30 min. The pre-adsorption of NH_3 was then performed at 120 °C under the flow of pure NH_3 for 30 min. After that, the physically adsorbed NH_3 was swept by Ar flow (20 ml/min) at the same temperature for 2 h. Finally, the temperature of the sample was increased from 120 to 650 °C at a ramp of 10 °C/min under the flow of Ar at 20 ml/min. Desorption of NH_3 (m/z = 17) and the signal of Ar (m/z = 40) and H_2O (m/z =18) were measured online by the Ametek mass spectrometer (Dymaxion Benchtop).

Hydrogen temperature-programmed reduction (H_2-TPR) was performed on the same Micrometrics AutoChem 2910 equipped with Agilent 5973 mass spectrometry to monitor the formation of H_2O (m/z=18) during the TPR. Hydrogen consumption during the TPR monitored by the Ametek mass spectrometer was negligible due to the low metal loading. Specifically, 0.2 g sample was first pretreated under Ar (30 mL/min) at 600°C for 30 min to remove the moistures adsorbed on the catalyst. The temperature of the sample was then decreased to 200°C before switching the reactor influence to 10% H_2/Ar. The sample was kept at 200°C until the signal of H_2O and H_2 reaches the baseline. Afterward, the temperature was increased to 800°C at 10 °C /min. The signal of H_2O and H_2 was recorded by the two mass spectrometers aforementioned.

The XRD patterns of the activated catalysts (after reduction, at 650°C for 30 min, and passivation) were measured by the Rigaku Ultima III X-ray Diffraction System with Cu Kα radiation (154.06 pm, 40 kV, and 44 mA). Diffraction spectra were collected at the scanning rate of 4° min^{-1} in the range of 2θ from 4°-70°.

The surface chemistry of the activated catalysts was measured using a Thermo Scientific K-alpha X-ray Photoelectron Spectroscopy (XPS) equipped with a monochromatic aluminum X-ray source at 1486.6 eV. A spot size of 400 µm^2 was used for each measurement. The survey spectra were collected in the binding energy range of 0-1350 eV with a pass energy of 200 eV at a step size of 1 eV. To correlate the high resolution (HR) core level spectra of Ga 2p and Ni 2p, a 40 eV pass energy under an ultrahigh vacuum condition with an energy step size of 0.1 eV was applied. The C1s binding energy at 284.5 eV of adventitious carbon was taken as an energy reference to compensate for surface charging effects.

The X-ray absorption spectroscopy (XAS) experiments of the activated catalysts, involving X-ray absorption near edge structure (XANES) and extended X-ray absorption fine structure (EXAFS), were conducted at the beamline 20-BM in Advanced Photon Source (APS). Data were acquired in fluorescence mode using a 13-element germanium detector; the sample was set at a 90 degree angle to the incoming beam and detector. Powder samples were pressed to a disk and sealed in Kapton® tape before being attached to the sample stage. Spectra were recorded at the K-edge of Ni and Ga. The XAS data were normalized and analyzed by Athena software.

Transmission electron microscopy (TEM) images and STEM-EDX chemical mapping of the activated catalysts were obtained using a JEOL 2100TEM (accelerating voltage 200kV) equipped with a Gatan camera.

4.2.3 Catalytic Performance Evaluation

The catalytic performance of the prepared catalysts in ethane aromatization was tested in a home-built setup for step-change transient kinetic analysis. Typically, 0.2 g of the catalysts were loaded into a stainless-steel reactor (ID, Φ = ¼ inches) and activated in 10% H_2/Ar (20 ml/min) at 650 °C (ramp 10 °C/min) for 30 min. After activation, the temperature of the reactor was decreased to 550 °C and the reactor influent was switched to pure Ar (20 ml/min). Prior to each experiment, Ar and the by-pass feed spectra were both recorded for mass spectrometer calibration and used as a reference for the calculation of conversion. Finally, the reaction was initiated by fast switching (by a 4-way valve) of the reactor influent gas from Ar (20 ml/min) to C_2H_6 (20 ml/min, which gives a GHSV (gas hourly space velocity) of 4000 h^{-1}). The effluent gases were analyzed continuously by an online Agilent 5973 mass spectrometry. Information about the catalytic behavior during the early-stage induction period and the "steady-state" deactivation can be obtained simultaneously. A more detailed method for product quantification with the mass spectrometer has been shown in our previous paper [35]. It must be noted that the blank test of the stainless-steel reactor shows negligible activity in ethane conversion at 550°C. We used the stainless steel (instead of quartz) reactor because the Ni/HZSM-5 catalyst shows significant high activity towards coking, which will crack the quartz reactor.

4.2.4 Catalyst deactivation kinetics evaluation

The general reaction rate with catalyst deactivation can be expressed as

$$r(T, C, t) = r_{t0}(T, C) \cdot a(t) \tag{4.1}$$

Where r_{t0} (T, C) is the rate after reaching the steady-state, T is reaction temperature, C is reactants concentration, and a (t) represents the reactivity coefficient (a (t) ≤ 1).

The rate of deactivation or the kinetic expression of the reactivity coefficient a (t) will be evaluated based on the generalized power-law equation model (GPLE) [45, 46].

$$-\frac{da}{dt} = k \cdot f(C) \cdot (a - a_\infty)^\beta \tag{4.2}$$

Where k is the rate constant of deactivation (as a function of T); f (C) is the power law expression of the deactivation rate (as a function of the concentration of the reactants and products); β is the order of deactivation (should be an integer), and a_∞ is the asymptotic reactivity coefficient as the time approaches infinity (a_∞ should approach to 0 for the present catalytic system). Assuming the concentration term f (C) is independent of the deactivation rate, namely f (C) is constant, integration of Eq. (2) for the first order (β = 1) deactivation kinetics can be written as:

$$a(t) = exp(-k_1 t) \tag{4.3}$$

For second order (β = 2) deactivation kinetics, it can be integrated to

$$a(t) = \frac{1}{1 + k_2 t} \tag{4.4}$$

For the present catalytic system, we proposed to modify the GPLE models by adding power to the time (t in equations (3) and (4) becomes t^α). We expect $\alpha \leq 1$ and can be understood as the change of the amount of coke deposition on the surface of the catalyst "$C_C = At^n$" where C_C is the concentration of carbon on the surface of the catalyst (g/m^2). The modified first and second order deactivation kinetic models are shown in equations (5) and (6):

$$a(t) = exp(-k_1 t^{\alpha_1}) \tag{4.5}$$

$$a(t) = \frac{1}{1 + k_2 t^{\alpha_2}} \tag{4.6}$$

It is seen that the second order modified GPLE model is the same (in mathematic) as the model we proposed in our previous paper for ethane aromatization over the Zn exchanged HZSM-5 catalysts [35]. The activity coefficient was expressed as a function of the concentration of carbon on the catalyst C_C ($a = 1/(1+ k_0 C_C^{\beta})$).

The kinetic parameters k and α will be determined and the effect of chemical compositions of the metal species on the parameters k and α will be discussed.

4.3 Results and Discussion

4.3.1 Catalyst Characterization

The prepared Ni and/or Ga modified HZSM-5 catalysts were characterized by means of XRD, H_2-TPR, XPS, XAS, TEM/STEM-EDX, and NH_3-TPD. As shown in Figure 4.1, the XRD patterns of the monometallic Ni and Ga modified HZSM-5 show almost identical diffraction patterns to the HZSM-5 zeolite host. The diffraction of Ni and Ga species was absent, indicating very high dispersion of the Ni and Ga related species in the HZSM-5 zeolite. The metal species on the zeolites normally underwent significant ion exchange during impregnation and the high-temperature activation process to form exchanged Ni^{2+} or Ga^{+}, $[GaO]^{+}$, and $[GaOH]^{+}$, cations (see also XPS characterization) [47, 48]. Quite interestingly, a new peak at 2 θ of 43.5° (see the inset), which can be assigned to the diffraction of 111 facet of the Ni_3Ga intermetallic alloy [49, 50], was identified for the bimetallic Ni/Ga modified HZSM-5 catalysts. As shown in Figure 4.1 (inset), the formation of such Ni-rich intermetallic alloy with a stoichiometric Ni/Ga ratio of 3/1 was favored under Ga-rich conditions (Ni_1Ga_1 and Ni_1Ga_3 samples).

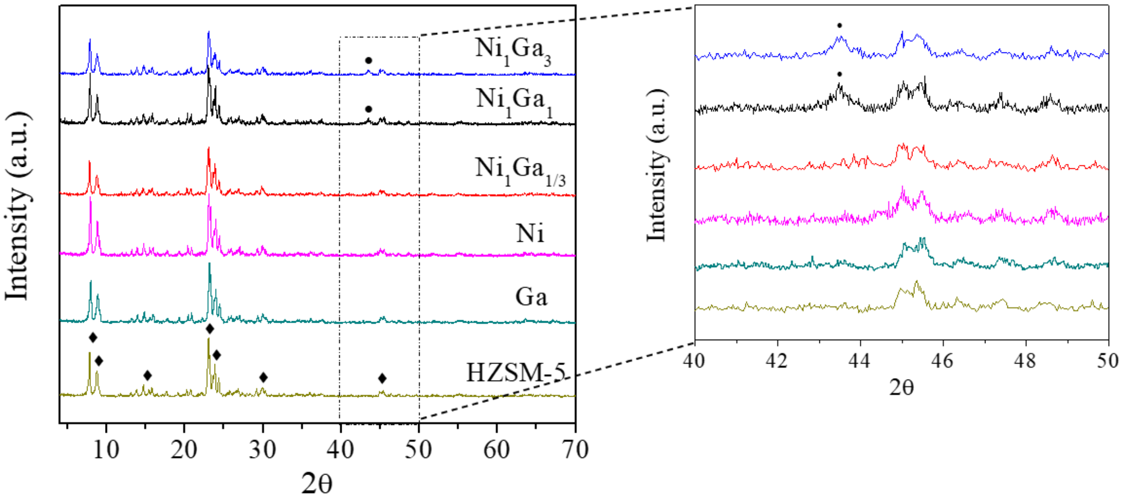

Figure 4.1 XRD patterns of bimetallic Ni/Ga and its monometallic components supported ZSM-5 and parent ZSM-5.

The H_2-TPR profiles (see Figure 4.2)) clearly show two distinct peaks at temperatures range of 250-450 °C and 550-750 °C, corresponding to the reduction of the oxidic Ni and Ga particles, respectively [31, 51, 52]. While the peak for the reduction of Ni species in the monometallic sample was found at 367 °C, the profile was not back to the baseline until 600 °C, indicating the presence of the exchanged Ni^{2+} Lewis acid sites [51, 53]. In contrast to the monometallic Ga/HZSM-5 sample, the broadness of the profiles for the bimetallic samples was decreased, indicating the presence of metallic Ni species promoted the reduction of the Ga species through hydrogen spillover. More interestingly, the intensity of the Ga peak for the Ni_1Ga_1/HZSM-

5 is the highest among the samples (even higher than the samples with higher Ga loading), suggested that the reduction of Ga species was favored at Ni-rich condition.

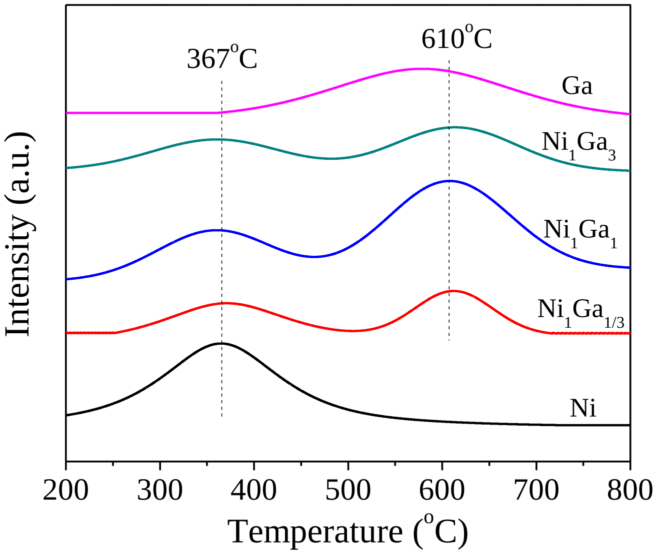

Figure 4.2 H_2-TPR profile of bimetallic Ni/Ga and its monometallic components supported ZSM-5.

The Ni and Ga $2p_{3/2}$ XPS spectra of the samples are displayed in Figure 4.3, and the normalized relative concentration of Ni^0/Ni^{2+} and $Ga^0/GaO^+/Ga^+$ from the spectra are shown in Table 4.1. As shown in Figure 4.3, the Ga $2p_{3/2}$ spectra could be deconvoluted into three peaks at 1116.7, 1118.2, and 1119.2 eV, respectively. The low binding energy peak at 1116.7 eV is associated with metallic gallium (Ga^0), which, however, was almost absent for the Ga/HZSM-5 and $Ni_1Ga_{1/3}$/HZSM-5 samples. As shown in Table 4.1, the normalized concentrations of Ga^0 were ~ 5% for the Ga/HZSM-5 and $Ni_1Ga_{1/3}$/HZSM-5, which might be originated from the error of deconvolution. Nevertheless, the concentration of Ga^0 was 19.5 and 7.8%, respectively, for the

Ni_1Ga_1/HZSM-5 and Ni_1Ga_3/HZSM-5, indicating the presence of Ni^0 promoted the reduction of Ga species (consistent with the TPR results) through hydrogen spillover and yielded the formation of intermetallic alloys (see XRD). The higher-binding energy peaks at 1118.2 and 1119.2 eV are attributed to the GaO^+ and Ga^+ cations, respectively, bound to the zeolite (see eqs. 4.7-4.10 for the most plausible reactions) [47, 52, 54-56]. More detailed normalized concentrations of these species are shown in Table 4.1.

$$\mathrm{Ga_2O_3} + 2H^+\mathrm{OZ^-} \rightarrow \mathrm{2GaO^+OZ^-} + \mathrm{H_2O} \tag{4.7}$$

$$\mathrm{Ga_2O_3} + \mathrm{H_2} \rightarrow \mathrm{Ga_2O} + \mathrm{2H_2O} \tag{4.8}$$

$$\mathrm{Ga_2O} + 2H^+\mathrm{OZ^-} \rightarrow \mathrm{2Ga^+OZ^-} + \mathrm{H_2O} \tag{4.9}$$

$$\mathrm{GaO^+OZ^-} + \mathrm{H_2} \rightarrow \mathrm{Ga^+OZ^-} + \mathrm{H_2O} \tag{4.10}$$

Different from the Ga $2p_{3/2}$ spectra, the intensity of the Ni $2p_{3/2}$ spectra of various samples is significantly lower. As shown in Figure 4.4, the spectra show two main peaks at 852.2 and 856.5 eV for the metallic Ni^0 and Ni^{2+}, respectively [53, 57, 58]. It is speculated that most of the Ni species were anchored inside the zeolite channels, and part of which has been exchanged with the Brønsted acid sites, forming Ni^{2+} cation as the Lewis acid site. Additionally, the surface concentrations of the nickel species are varied depending upon the ratio of Ni/Ga, although the samples are containing the same 2 wt% nominal Ni loadings. In particular, the Ni_1Ga_1/HZSM-5 sample shows the highest Ni^0 concentration, which once again can be explained by the formation of Ni_3Ga intermetallic alloy particles outside the zeolite channel, consistent with the XRD patterns and Ga 2p spectra. While the XRD patterns show the formation of Ni_3Ga intermetallic alloy, the ratio of Ni^0/Ga^0 on the surface is different from the 3/1 stoichiometric, which indicates the presence of unalloyed metallic species or the formation of different Ni/Ga stoichiometric alloys on the surface of the particles. However, these species cannot be directly identified from the XRD patterns.

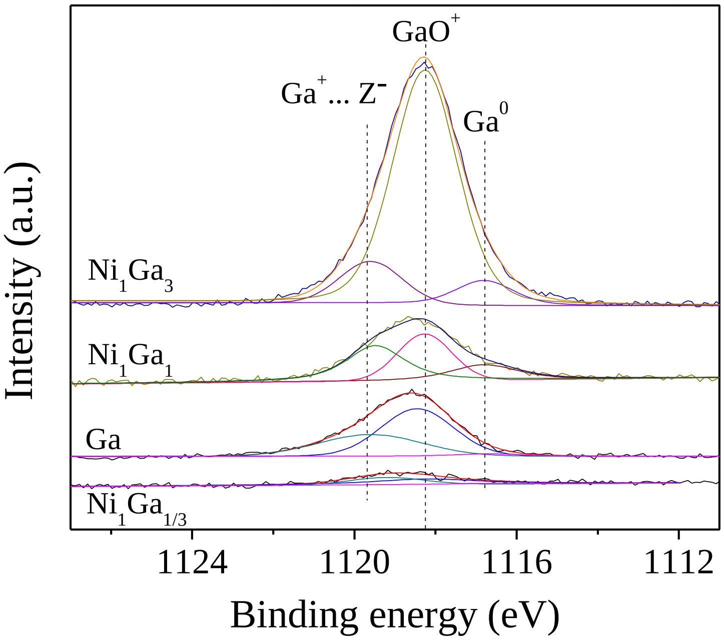

Figure 4.3 Ga 2p XPS spectra of bimetallic Ni/Ga and monometallic Ga supported ZSM-5.

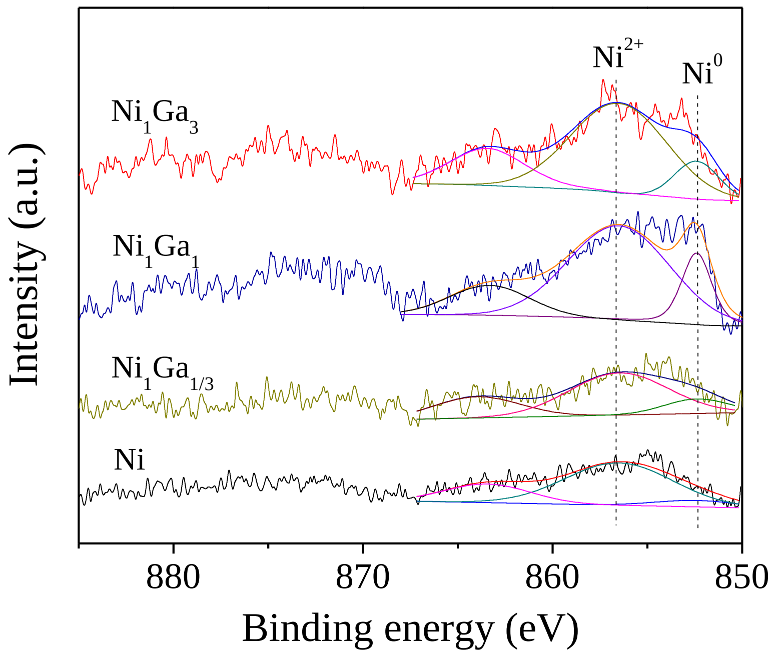

Figure 4.4 Ni 2p XPS spectra of bimetallic Ni/Ga and monometallic Ni samples.

Table 4.1 Quantitative analysis of the relative surface composition of various Gallium and Nickel species for different catalysts

Catalyst	Ga°	GaO^+	Z-…Ga^+	Ni^0	Ni^{2+}
Ni_3Ga_1/HZSM-5	120(5.4)	1318(59.4)	779(35 .1)	328(18.2)	1466(81.8)
Ni_1Ga_1/HZSM-5	1868(19.5)	3679(38.5)	4016(42)	842(20)	3364(80)
Ni_1Ga_3/HZSM-5	2415(7.8)	24721(80)	3802(12.2)	592(16.4)	3000(83.6)
Ni/HZSM-5	----	---	---	187(10.4)	1600(89.6)
Ga/HZSM-5	360(4)	5267(58.7)	3337(37.3)	---	---

The Ni_1Ga_x/HZSM-5 samples were further characterized by X-ray absorption spectroscopy (XAS). XANES spectra of the K-edge of Ni and Ga are shown in Figures 4.5 a and c. The Ni K-edge spectra of the Ni_1Ga_x/HZSM-5 samples, as well as the Ni modified HZSM-5 samples prepared through impregnation (IM) and ion-exchange (IE) were compared with the Ni foil and $Ni(OH)_2$ standards. As shown in Figure 4.5 a, while the Ni IE shows a similar adsorption edge to the $Ni(OH)_2$, the edges of the Ni IM and Ni_1Ga_x samples are between the Ni foil and $Ni(OH)_2$ standards. Additionally, the adsorption edges of the Ni_1Ga_x samples shifted to the left in contrast to the Ni IM, indicating the presence of Ga affects the chemical state of the Ni species. The Fourier transform EXAFS spectra of the Ni K-edge (Figure 4.5 b) show that the radial distance of Ni-Ni is slightly larger than that for the Ni foil standard, which suggested the formation of Ni_3Ga intermetallic alloy rather than monometallic Ni particles [58]. Further information about the coordination number and the bond length cannot be identified from the EXAFS, because it is difficult to fit/model the data reliably due to the presence of Ni species with different chemical states. The Ga K-edge spectrum of the sample shifted to lower energy than the Ga foil shows a quite different pre-edge peak, which suggested the formation of positively charged $Ga^{\delta+}$ species. Additionally, the pre-edge peak shown in the spectrum is also quite different from the β-Ga_2O_3, indicating such Ga species (exchanged with the proton of the zeolite) are coordinated in both tetrahedral and octahedral with O atoms [59]. Fourier-transformed EXAFS spectrum of the Ga K-edge (Figure 4.5 d) shows dominant features at 1.4 and 2.1 Å in R-space, corresponding to backscattering from O atoms coordinated to Ga^{3+} centers [59].

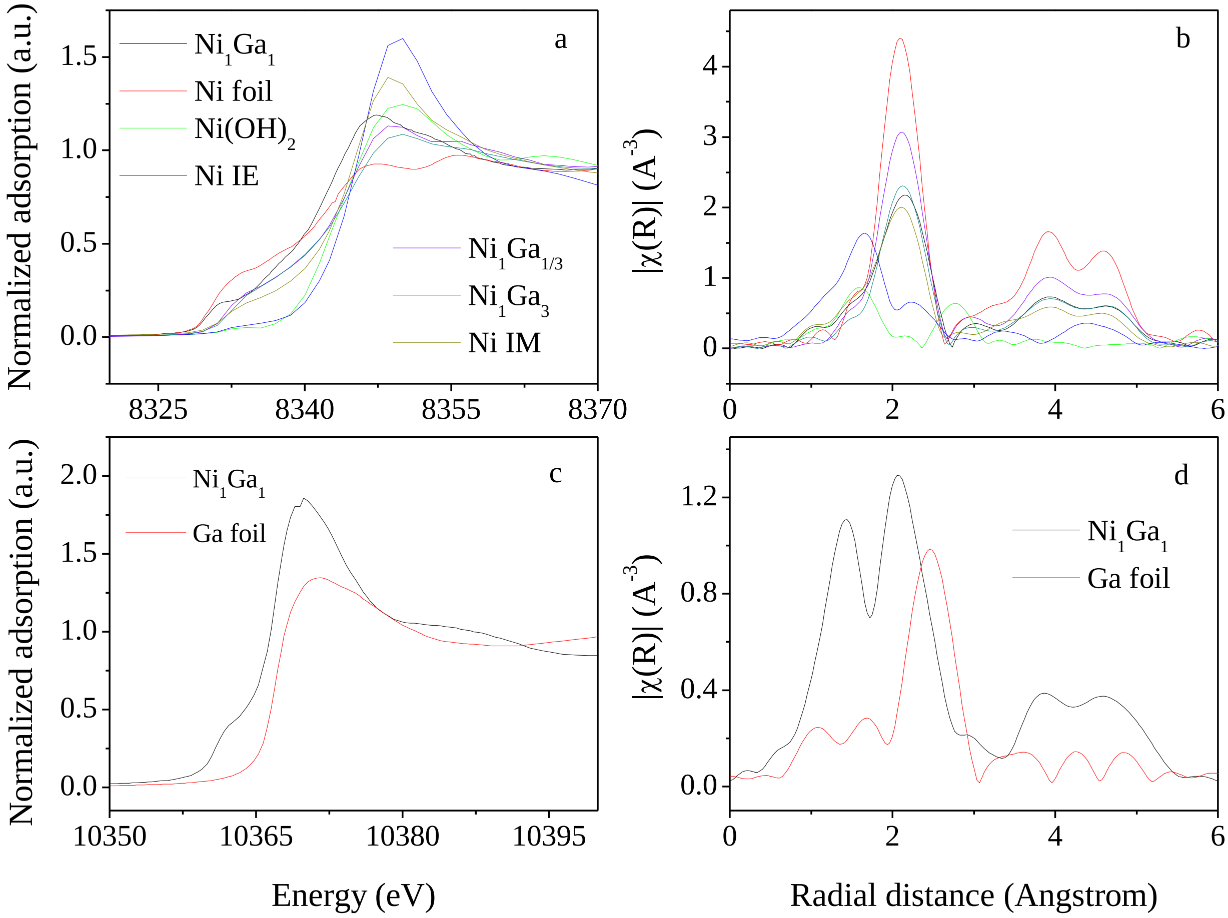

Figure 4.5 XAS spectra at the K-edge of Ni and Ga, respectively.

(a) and (c): Normalized XANES spectra of Ni (panel a) and Ga (panel c), (b), and (d): the magnitude of the Fourier transform EXAFS spectra of Ni (b) and Ga (d).

The chemical properties of the metal species were further characterized by TEM and STEM-EDS. As shown in Figure 4.6 for the Ni_1Ga_1/HZSM-5 sample, a considerable number of nanosized particles (range from 5 to 40 nm) are observed from the TEM image. These particles should be located outside the zeolite channels since their size is much larger (>10 times) than the pore size of the MFI zeolites. Smaller particles or nanoclusters anchored inside the zeolite channels cannot be identified from the TEM and HRTEM images since it quickly eclipses due to the fast etching of the zeolite framework under high-energy electrons. Nevertheless, from the STEM-EDS chemical mappings, besides the aggregated particles identified from the TEM image, a relatively homogeneous distribution of the Ni and Ga species on the ZSM-5 host was observed at the regions where the large particles were not identified. Therefore, the metal species must migrate into the channels of the zeolite and form either nanoclusters or exchanged with the H^+ of the zeolites forming metal cations (δ^+) as the Lewis acid sites. Additionally, the Ni and Ga show almost identical distribution over the entire zeolite host, which suggested that Ni and Ga species have close intimacy, and part of which should form intermetallic alloys as identified by the XRD. Quantitative analysis of the EDS spectrum suggested that the Ni and Ga loadings are both around 1.8 wt% (see Figure 4.7), similar to the nominal Ni/Ga ratio and loadings. The TEM images and STEM-EDS chemical mappings for the other samples are shown in Figures 4.8 to 4.11. It seems that the distribution of metal species for the other samples shows less homogeneity than the Ni_1Ga_1/HZSM-5 sample.

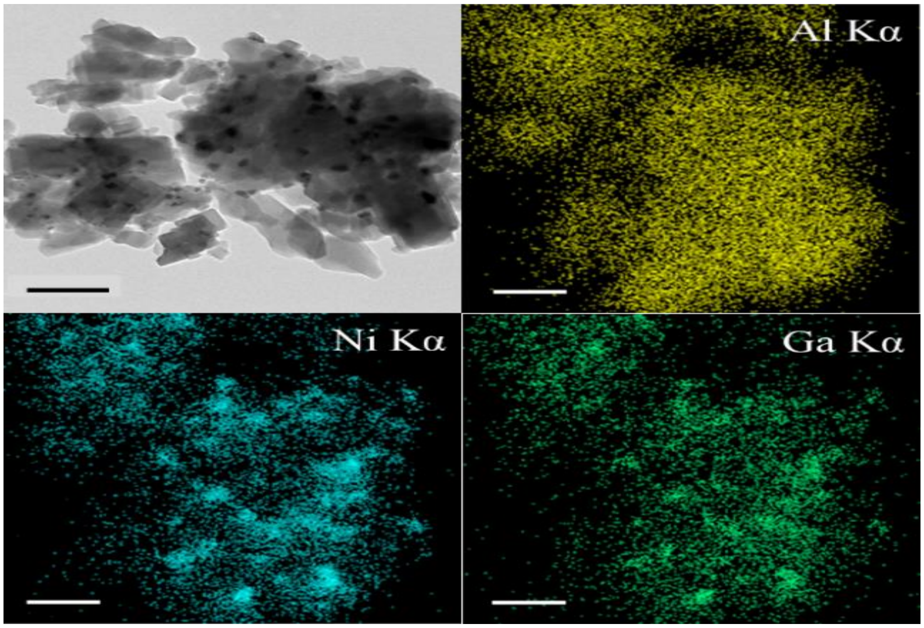

Figure 4.6 TEM image and STEM-EDS chemical mapping of Al, Ga, and Ni for Ni_1Ga_1/HZSM-5 sample. Scale bar 250 nm

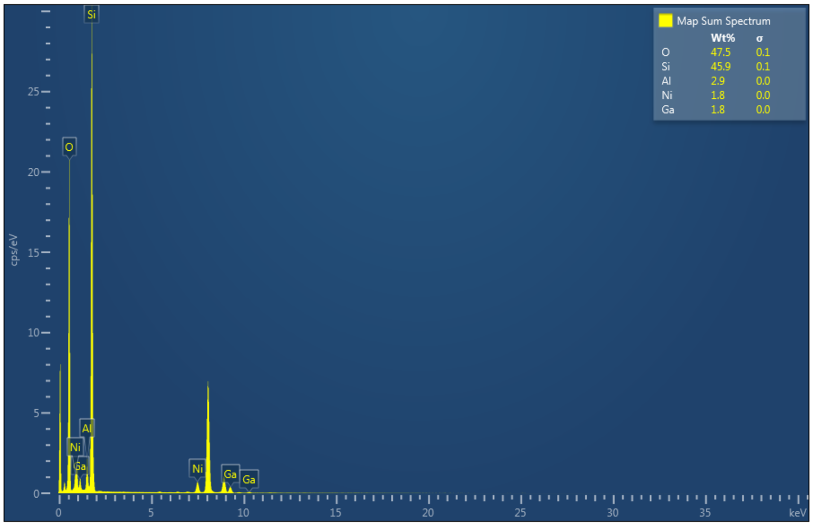

Figure 4.7 EDS spectrum of Ni_1Ga_1/HZSM-5 sample

This result shows almost similar Ni/Ga ratio (1/1) and loadings (1.8 wt%) as the nominal Ni and Ga loadings (2 wt%) and ratio (1/1)

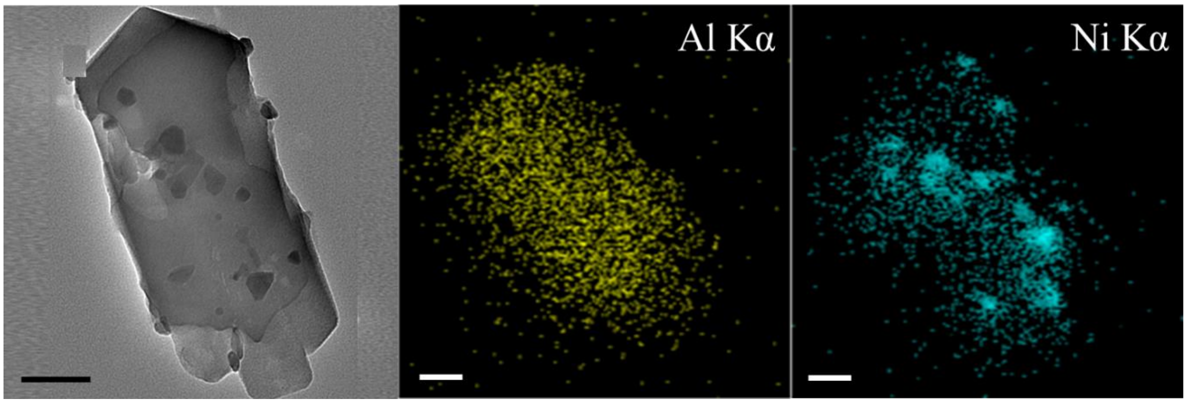

Figure 4.8 STEM-EDX chemical maps of Al and Ni Kα Ni/HZSM-5 (scale bar 100 nm).

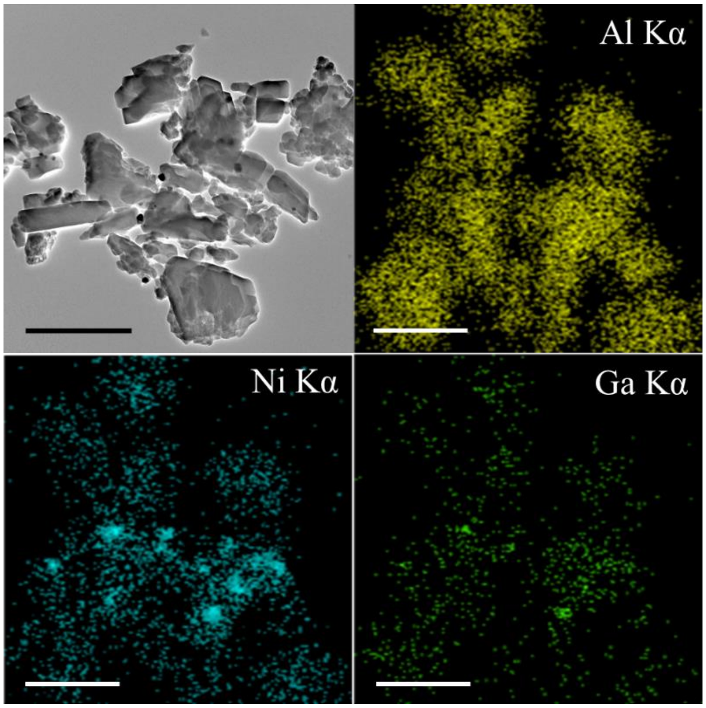

Figure 4.9 STEM-EDX chemical maps of Al, Ga, and Ni Kα for $Ni_1Ga_{1/3}$/HZSM-5 (scale bar 500 nm).

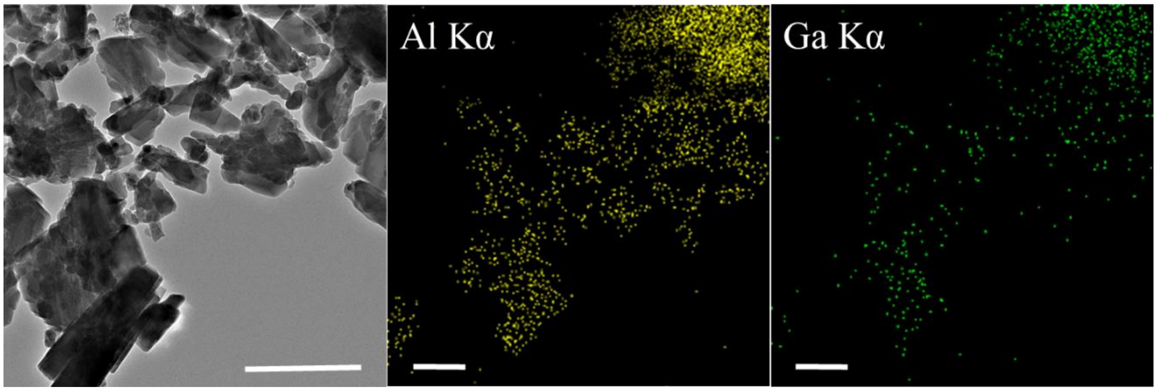

Figure 4.10 STEM-EDX chemical maps of Al and Ga Kα for Ga/HZSM-5 (scale bar 500 nm).

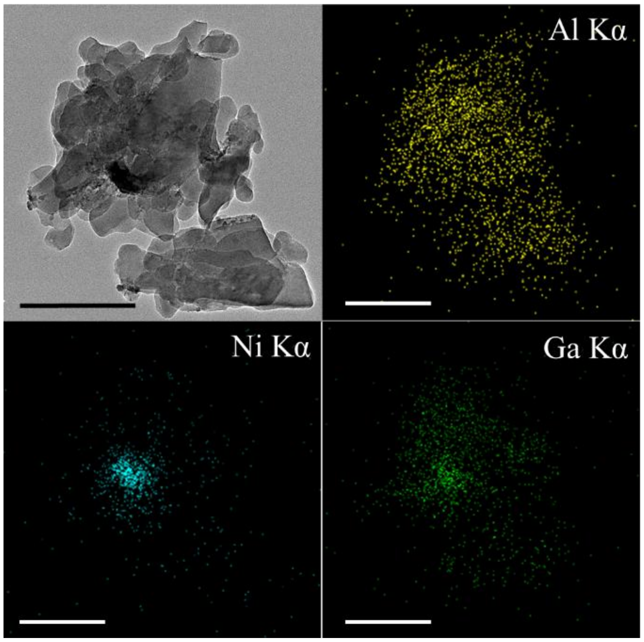

Figure 4.11 STEM-EDX chemical maps of Al, Ga, and Ni Kα for Ni_1Ga_3/HZSM-5 (scale bar 250 nm).

The effect of metal species modification on the acidity of the HZSM-5 zeolite was characterized by the NH_3-TPD. As shown in Figure 4.12 a, NH_3 desorption profiles exhibit mainly two peaks at 150-350 and 360-550°C, corresponding to the weak and strong acidic sites, respectively. In comparison with the HZSM-5 host, the presence of metal species decreased the density of total acid sites (see Table 4.2), especially the strong Brønsted acids. The metal species could exchange with part of the H^+ of the zeolite to form Ni^{2+}, GaO^+, and Ga^+ metal cations (see discussion of XPS results), which decreased the Brønsted acid density and increased the Lewis acid density. Such a conclusion was proved by the deviations of the NH_3 profiles (for the metal modified HZSM-5) from the HZSM-5 host (see Figure 4.12 b), which shows positive deviation at low temperatures and negative deviation at high temperatures. It is also seen that Ga has the least effect on the strong acid site of the zeolite. The desorption of NH_3 deviates only around -5 μmol/g/min at a temperature around 500 °C. The Ni/HZSM-5 and NiGa/HZSM-5 (with Ni/Ga ratio 3/1 and 1/3) show significantly higher such deviations, indicating the ion-exchange of the Ni species with the H^+ of the zeolite is easier than the Ga species (the same conclusion can be obtained based on the XPS results). What is the most interesting is the Ni_1Ga_1/HZSM-5 sample, while it contains the same Ni loading as the other samples, a significantly lower deviation was observed. Therefore, it might be expected that the Ni_1Ga_1/HZSM-5 catalyst might be a good candidate for ethane aromatization since it shows a balanced metal function (Ni_3Ga intermetallic alloy) and acidity.

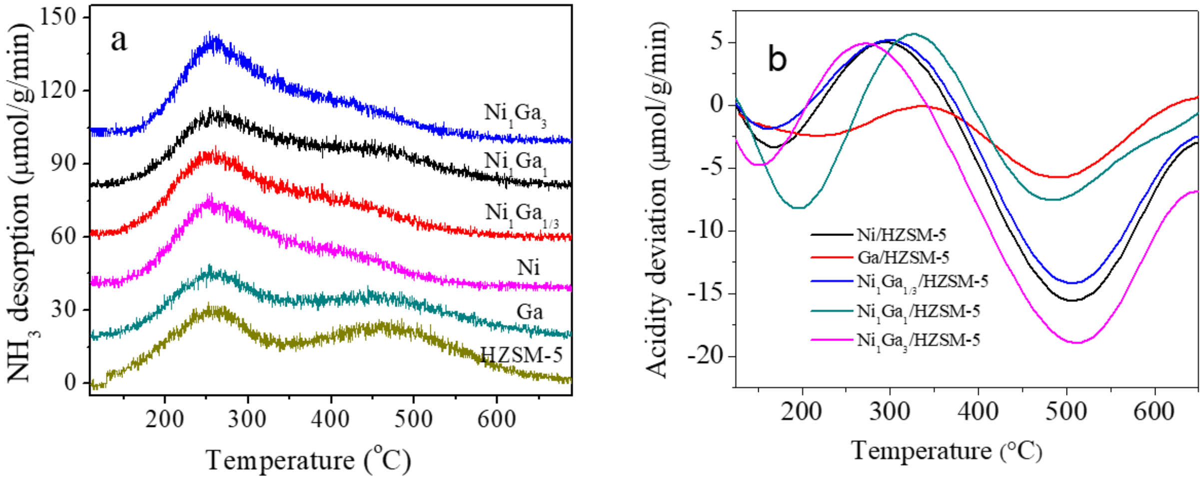

Figure 4.12 a) NH_3-TPD profiles, and b) Deviations of the NH_3 profiles for the metal modified HZSM-5 catalysts from the HZSM-5 acidity.

Table 4.2 Quantitative analysis of total acidity for various catalysts, indicating the decrease in density of total acid sites after addition of metal species to ZSM-5 support.

Catalyst	Total acidity by strength (μmol.g^{-1})
Ni/HZSM-5	1120
Ni_3Ga_1/HZSM-5	1135
Ni_1Ga_1/HZSM-5	1222
Ni_1Ga_3/HZSM-5	1275
Ga/HZSM-5	1142
HZSM-5	1516

4.4 Catalytic Performance

The catalytic performance of the Ni and/or Ga modified HZSM-5 catalysts will be discussed based on the early-stage behavior and the steady-state activity/selectivity, respectively. As shown in Figure 4.13 a-e, the chemical compositions of the metal species have a significant influence on the early-stage (induction period) reactivity based on the step-change transient experiments. While methane shows in the gas phase and reaches the maximum rate of production immediately (after switching the reactor influent from Ar to ethane), all of the other products show delay with various extent dependent highly upon the compositions of the metal species. For the Ga/HZSM-5 catalyst (Figure 4.13a), ethylene was produced right after methane, whereas the formation of benzene and toluene was delayed for 30 and 50 s, respectively. For the Ni/HZSM-5 catalyst (Figure 4.13b), such delay was significant. The formation of ethylene and benzene was observed after 10 min, and further delay was found for toluene and xylene. The presence of methane as the only gas-phase product during the early-stage suggested that the fresh Ni/HZSM-5 catalyst is highly selective for ethane cracking ($C_2H_6 \rightarrow CH_4 + C + H_2$). Additionally, ethane is absent from the gas phase for the initial ~4 min, indicating significantly higher initial activity (100% conversion) for the cracking. A fast decrease of methane or increase of ethane after 5 min further suggested that the catalytically active sites are being reconstructed during the early-stage. For the $Ni_1Ga_{1/3}$/HZSM-5 catalyst (Figure 4d), the delay times for benzene and toluene are 20 and 30 min, respectively, which are longer than that for the Ni/HZSM-5. However, ethylene was produced almost without delay, and it was not run into the steady-state even after 2 h. Additionally, the initial rate of methane over the $Ni_1Ga_{1/3}$/HZSM-5 is only one-tenth of that over the Ni/HZSM-5. Therefore, the catalytically active sites for ethane cracking/coking, as well as the rate of the catalyst surface reconstruction, are different between these two catalysts. Quite interestingly, the Ni_1Ga_1/HZSM-5 (Figure 4c) catalyst shows significantly reduced delay time, which is only slightly longer than that for the Ga/HZSM-5. Benzene and ethylene appear in the gas phase right after methane with a shoulder peak at 30 s, which might be due to the presence of different kinds of catalytically active sites. The Ni_1Ga_3/HZSM-5 (Figure 4.13e) shows a slightly longer delay time but very similar early-stage behavior to the Ni_1Ga_1/HZSM-5 catalyst. These two catalysts both show the formation of Ni_3Ga alloy based on the XRD, indicating a similar type of active site was formed.

The time-dependent rate for the formation of total BTX is compiled in Figure 4.13f. After the early-stage induction period, the Ni/HZSM-5 shows the highest rate for total BTX formation; however, it attenuates with time-on-stream (TOS) significantly faster than the other samples (the effect of metal function on the deactivation kinetics will be discussed later). It is seen that the Ni_1Ga_1/HZSM-5 shows a higher rate of BTX than the Ga/HZSM-5 and is more stable than the Ni/HZSM-5. The $Ni_1Ga_{1/3}$ and Ni_1Ga_3 modified HZSM-5 catalysts, however, show lower rates of BTX than the Ga/HZSM-5.

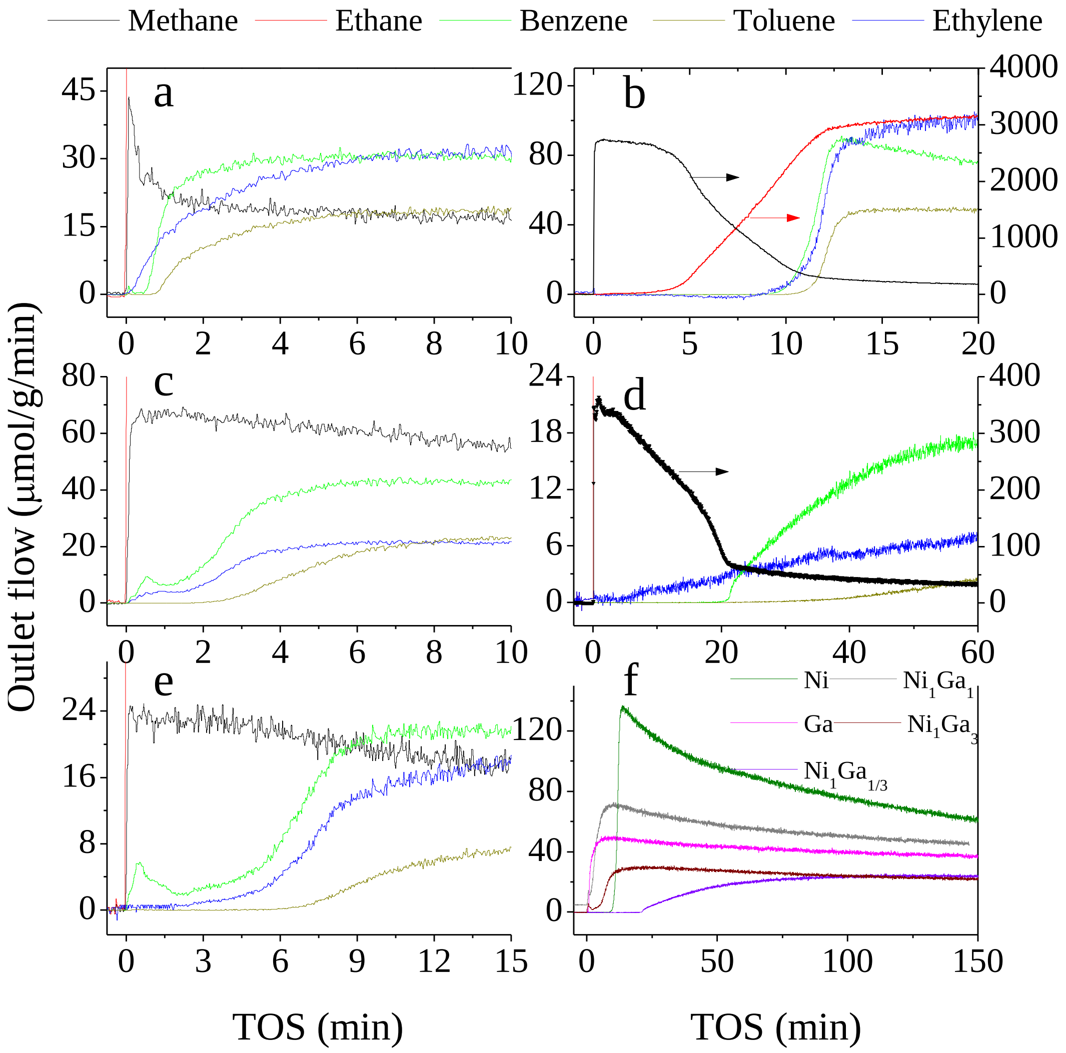

Figure 4.13 Early-stage catalytic behavior of ethane aromatization over the (a) Ga, (b) Ni, (c) Ni_1Ga_1, (d) $Ni_1Ga_{1/3}$, and (e) Ni_1Ga_3 modified HZSM-5 catalysts. (f) Rate of total BTX formation over different catalysts.

At t= 0, the reactor influent gas was switched abruptly from Ar to C_2H_6. Reactions were performed at T = 550 °C, P = 1 atm, and GHSV = 4000 h^{-1}

The catalytic performance in terms of ethane conversion and product selectivity is shown in Figure 4.14 (the rates of different products can be found in Figure 4.15). To re-emphasize, Ni and $Ni_1Ga_{1/3}$ modified HZSM-5 catalysts show a significantly high activity of ethane cracking during the early-stage. Up to 100% of ethane was converted into methane and coke over the

Ni/HZSM-5 catalyst. While Ni/HZSM-5 holds the highest ethane conversion, selectivity to BTX is the lowest among the samples (see Figure 4.16). Quite interestingly, the Ni_1Ga_1/HZSM-5 shows almost identical selectivity to that of Ga/HZSM-5. Additionally, all of the bimetal NiGa modified HZSM-5 catalysts show higher BTX selectivity than the Ni/HZSM-5, which suggested the synergistic effect between the Ni and Ga species. The early-stage and "steady-state" catalytic behavior suggested that the metal function significantly affects the reactivity of the catalyst in ethane aromatization. We expect that the Ni^0 nanoparticles are extremely active in ethane cracking, leading to the formation of methane and coke. The presence of Ni^0 might be the reason for the long induction period over the Ni/HZSM-5 and $Ni_1Ga_{1/3}$/HZSM-5 catalysts because such delay was not observed over the Ni-exchanged HZSM-5 catalyst (see Figure 4.15). Within the $Ni_1Ga_{1/3}$/HZSM-5 catalyst, the presence of a small amount of Ga does not lead to the formation of alloys (see XRD); therefore, Ni^0 represents the majority of Ni species in the catalyst. However, the presence of Ga (in close proximity with Ni, see Figure 4.6) reduced the activity of surface reconstruction, as a result leading to a longer delay time than the Ni/HZSM-5. Additionally, the exchanged Ni^{2+} Lewis acid site in the Ni/HZSM-5 sample should also be active for ethane dehydrogenation and aromatization; however, such kind of active sites produces large amounts of CH_4 and deactivate significantly faster than the Ga/HZSM-5 and Ni_1Ga_1/HZSM-5 catalysts (see Figure 4.15 (right bottom) for the catalytic performance of Ni exchanged HZSM-5 catalyst).

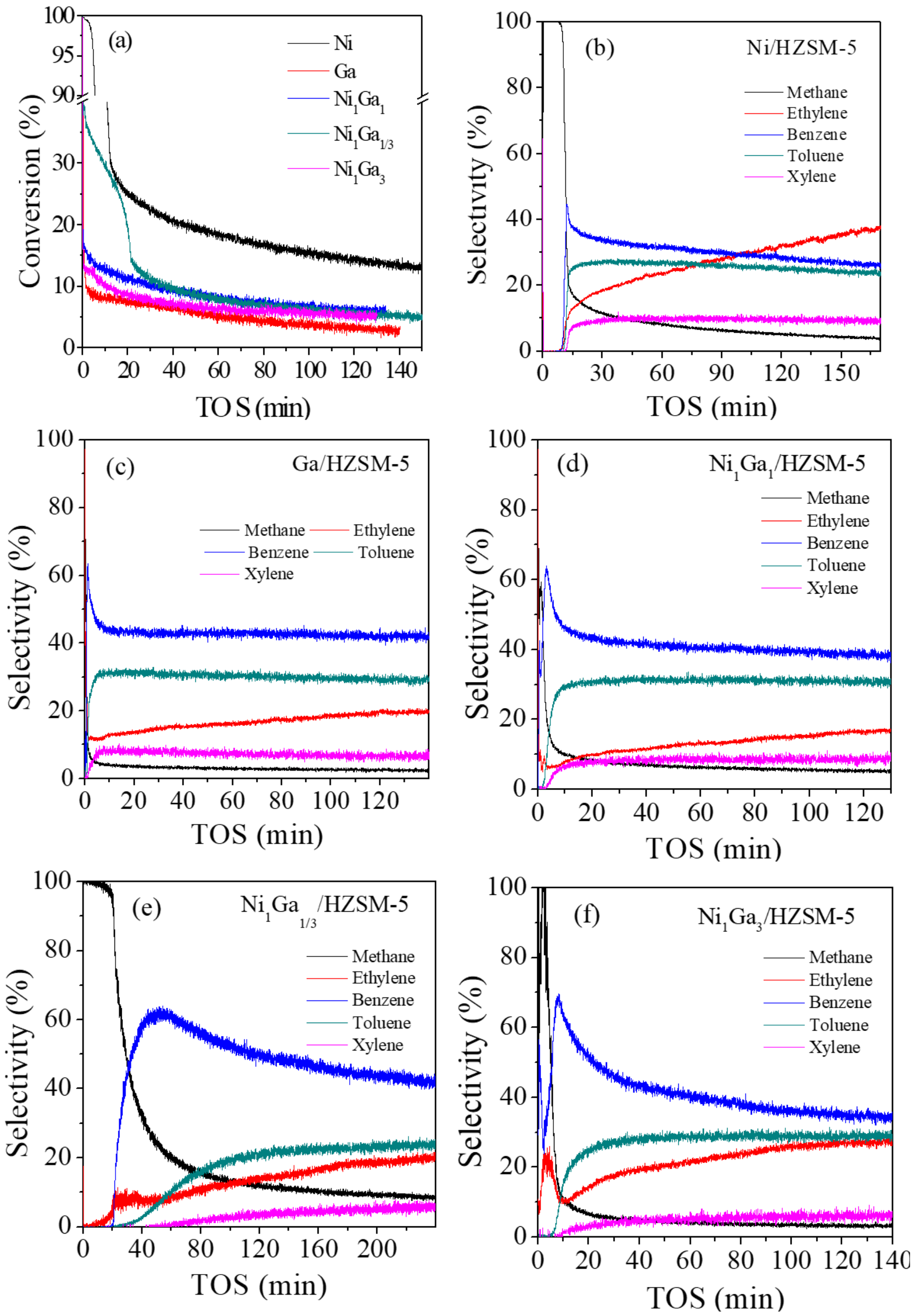

Figure 4.14 Time-resolved (a) conversion and (b-f) selectivity of methane, ethylene, benzene, toluene, and xylene for various catalysts.

The reaction condition is the same as in Figure 4.13.

For the bimetal Ni and Ga co-functionalized HZSM-5 catalysts (with Ga/Ni ≥ 1), the Ni nanoparticle most probably was absent due to the formation of new catalytically active sites, namely Ni_3Ga intermetallic alloy. Consequently, the long induction period was not observed. Recently, the Ni_3Ga intermetallic alloy was also identified as the catalytically active site for ethane and propane dehydrogenation by Laursen and coworkers [59, 60]. It might be important to mention that the long induction period was also found by Laursen et al. during both ethane and propane dehydrogenation over the $Ni_1Ga_{1/3}/Al_2O_3$ catalyst. The same as we have observed, during the early-stage, up to 100% selectivity to methane was observed during propane dehydrogenation [59]. That's probably the reason for treating the catalyst, before catalytic testing, under 10% propane at 600 °C for 6 h (the long induction period will be removed) [60]. Although the same bulk Ni_3Ga alloy was formed at different Ni/Ga actual loading, the "off-stoichiometric" 1/1 ratio of Ni and Ga was found to be optimal for ethane and propane dehydrogenation. Laursen et al. suggested that the Ga rich surface (forming core-shell type structure) is important for dehydrogenation. Within the present catalytic system, the Ga rich surface was also identified by the XPS. Since the HZSM-5 zeolite was used as the support for the Ni and Ga species, additional Ni and Ga species not incorporating into the intermetallic alloys could exchange with the proton of the zeolite, forming metal cations (Ni^{2+} and GaO^+, etc.) as the Lewis acid sites for the aromatization of both ethane and ethylene. We anticipate that the present Ni/Ga/HZSM-5 catalytic system for ethane aromatization might involve a tandem mechanism. Specifically, part of ethane was first dehydrogenated to ethylene on the Ni_3Ga particles. Then the mixture of ethane and ethylene was transformed into BTX over the exchanged Ni^{2+} and GaO^+ cations. The presence of ethylene could promote ethane aromatization over the galloaluminosilicate [11]. Therefore, the bimetallic Ni_1Ga_1/HZSM-5 catalyst shows higher activity (at similar BTX selectivity) than the monometallic Ga/HZSM-5 catalyst.

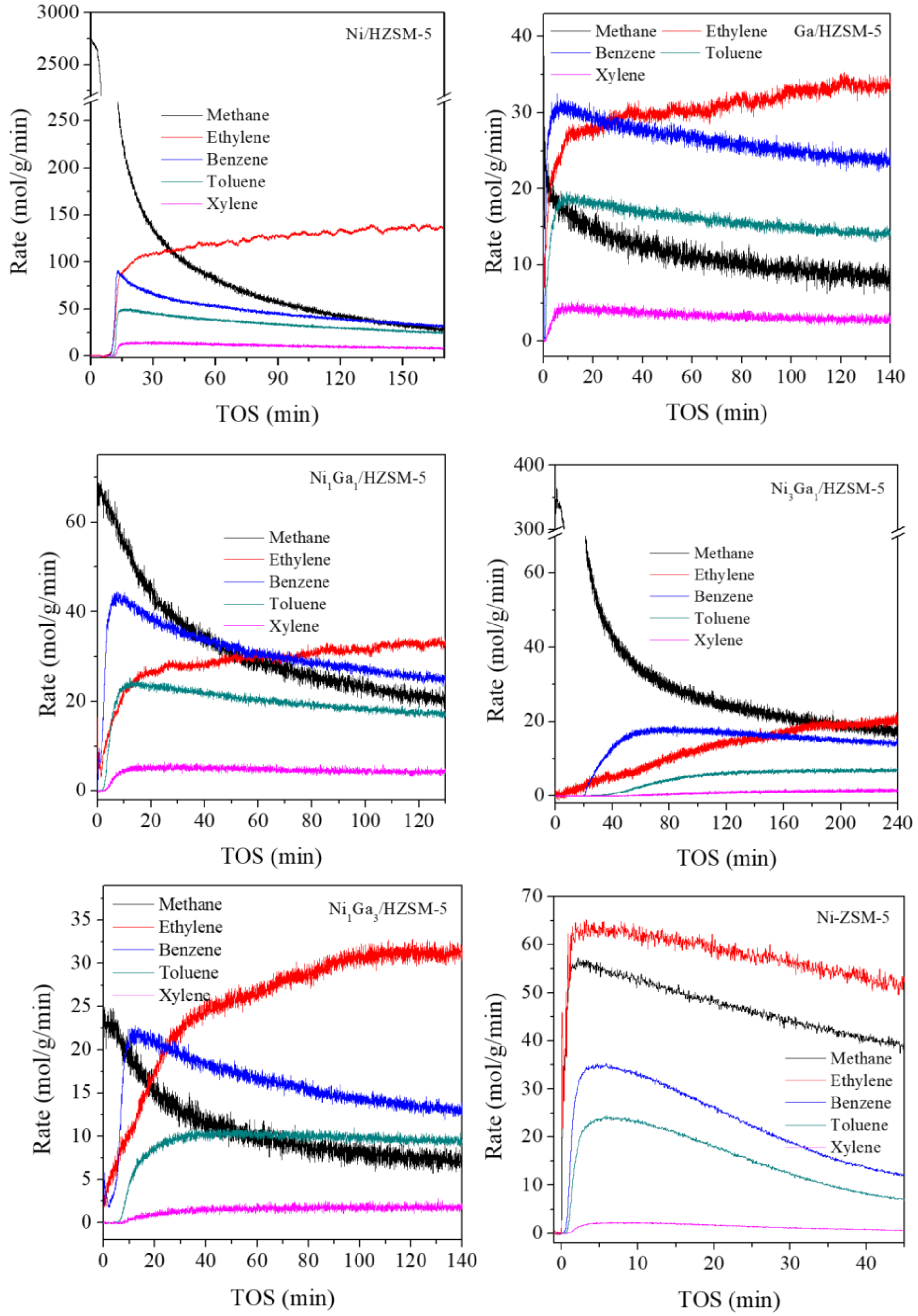

Figure 4.15 Time-resolved production rates of methane, ethylene, benzene, toluene and, xylene for the various metal-modified HZSM-5 catalysts.

The reaction was performed over 0.2 g of the catalyst (GHSV = 4000 h^{-1}) at 550 °C under atmospheric pressure.

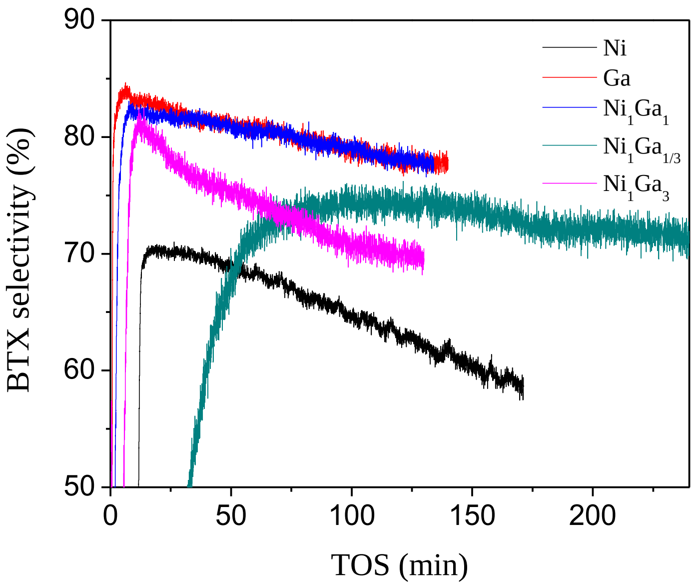

Figure 4.16 Time-resolved aromatic selectivity of ethane aromatization over the various metal-modified HZSM-5 catalysts.

The reaction was performed over 0.2 g of the catalyst (GHSV = 4000 h^{-1}) at 550 °C under atmospheric pressure.

4.4.2 Stability/Deactivation Kinetics

Deactivation of the zeolites-based catalysts is a common problem during hydrocarbon processing at high-temperature. As already mentioned, the rate of BTX formation attenuates with TOS. Both ethane conversion and BTX selectivity decrease due to coking (the selectivity of ethylene was increased). Figure 4.17 (a-c) shows the reactivity-time data of methane, benzene, and toluene over the Ni/HZSM-5, Ga/HZSM-5, and Ni_1Ga_1/HZSM-5 catalysts, respectively. It is clearly seen that the reactivity of all three products over the Ni_1Ga_1/HZSM-5 decreased slower than the Ni/HZSM-5 but faster than the Ga/HZSM-5. While the reactivity of methane over the Ni_1Ga_1/HZSM-5 is closer to the Ni/HZSM-5 than the Ga/HZSM-5, the reactivity of toluene over the same catalyst is similar to the Ga/HZSM-5 rather than the Ni/HZSM-5. We also noticed that the degree of reactivity attenuation varied for different products. It seems the reactivity of methane attenuates (with TOS) significantly faster than the benzene and toluene over the same catalyst, which suggested that different catalytic active sites and mechanisms might be involved. Different from methane and aromatics, the reactivity coefficient for ethylene (results not shown) increased with TOS during the investigated time period, which also indicated that ethylene is the intermediate product in such a tandem catalytic system.

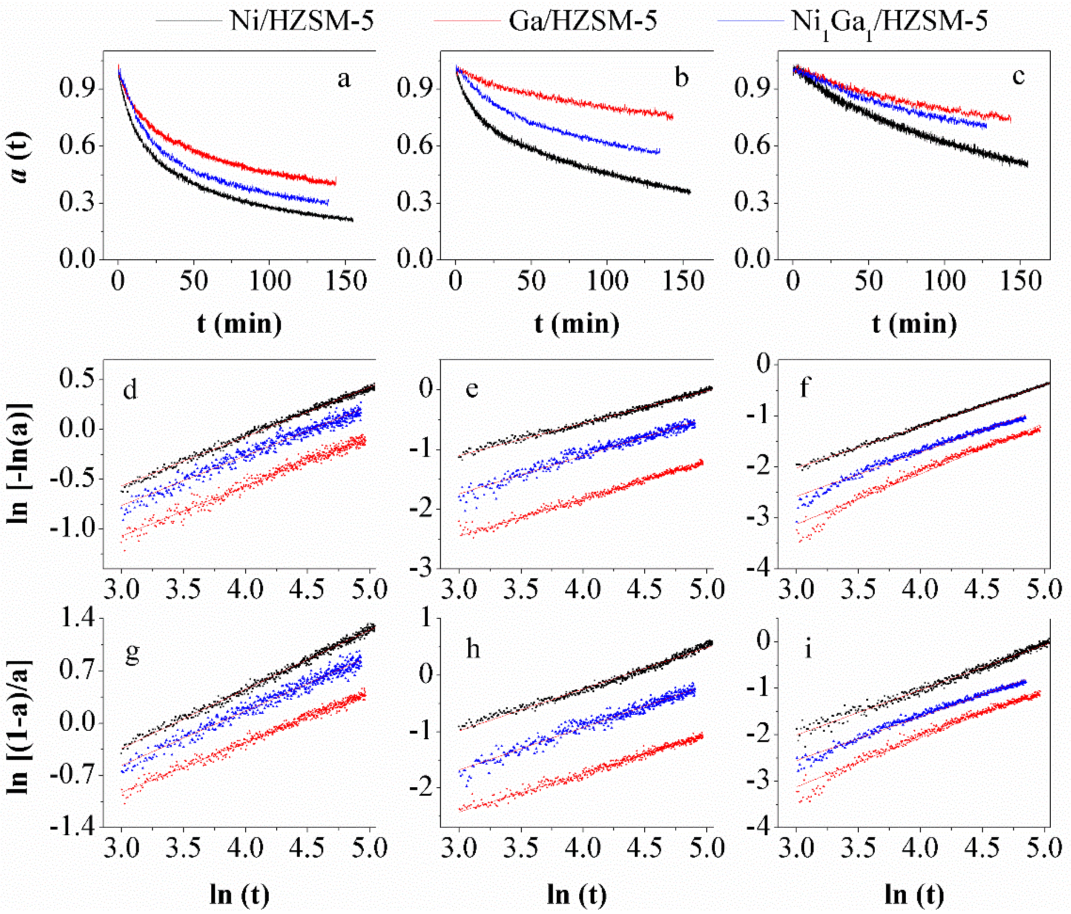

Figure 4.17 Deactivation kinetics of ethane aromatization.

(a), (b), and (c) changes of reactivity coefficient a(t) with time, for methane, benzene, and toluene, respectively. (d), (e), and (f) linear regression for the modified first order deactivation for (d) methane, (e) benzene, and (f) toluene. (g), (h), and (i) linear regression for the modified second order deactivation for (g) methane, (h) benzene, and (i) toluene

To better understand the influence of metal function on stability, the kinetics of deactivation were evaluated for the rate of methane, benzene, and toluene formation over the Ni, Ga, and Ni_1Ga_1 modified HZSM-5 catalysts, respectively. Xylene (due to its low selectivity) and ethylene (rate increased with TOS during the investigated time period) were not evaluated for the deactivation kinetics. We start with the generalized power-law equation (GPLE) model demonstrated in the experimental part. However, significant deviations were found for both first (see Figure 4.18) and second order (see Figure 4.19) deactivation for methane and benzene (deviation of toluene seems to be less significant). Therefore, the first and second order GPLE kinetic models were modified by adding a power α to the time t. As already mentioned in the experimental part, the parameter $\alpha \leq 1$, which indicates that the concentration of carbon on the surface of the catalyst was not increased linearly with TOS since the rate of coking was decreased. To identify the parameters α and k, the linear form of the modified first and second order deactivation models are shown in equations (4.11) and (4.12).

$$\ln[-\ln a(t)] = \ln k_1 + \alpha_1 \ln t \tag{4.11}$$

$$\ln[\left(\frac{1-a}{a}\right) = \ln k_2 + \alpha_2 \ln t \tag{4.12}$$

Figure 14.7 (d-f) shows the linear relation for the methane, benzene, and toluene, respectively, based on the first order modified deactivation kinetics (eq. 4.11), and such linear relation for the second order modified deactivation kinetics (eq. 4.12) is shown in Figure 4.17 (g-i).

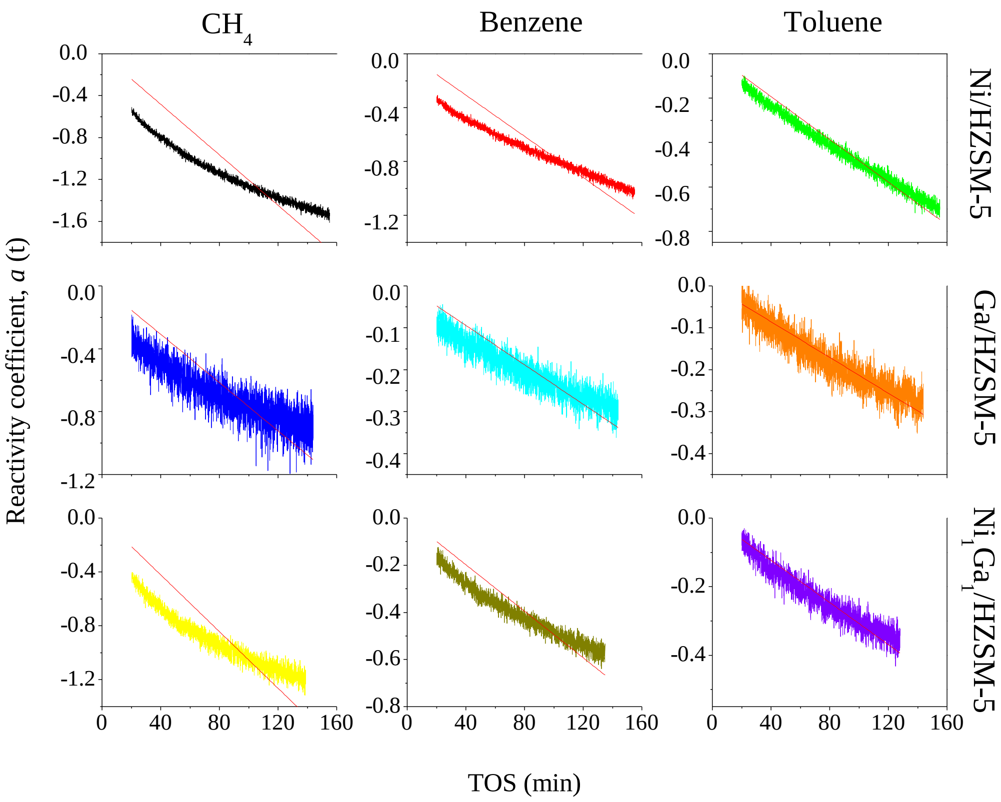

Figure 4.18 First order deactivation kinetics of ethane aromatization over Ni-HZSM-5, Ga-HZSM-5, and Ni_1Ga_1-HZSM-5.

Changes of reactivity coefficient a(t) with time for methane, benzene, and toluene. The reaction was performed over 0.2 g of the catalyst (GHSV = 4000 h^{-1}) at 550 °C under atmospheric pressure. The results show dramatic deviation for methane and benzene; however, deviation of toluene sounds to be less significant, comparatively.

It is seen that both 1st and 2nd order modified GPLE models fit well with the experimental data. It is clearly seen from the linearized relation that the metal function has a significant effect on the intercept (lnk) rather than the slop (α). The deactivation kinetic parameters for both 1st and 2nd order modified GPLE models are shown in Table 4.3. The 1st order model shows higher k and lower α than the 2nd order deactivation model for all investigated products and catalysts. In terms of the $t_{1/2}$ (time for a(t) = 0.5), the 2nd order model is longer than the 1st order for benzene and toluene over the Ga/HZSM-5 and Ni_1Ga_1/HZSM-5 catalysts, but they are similar over the

Ni/HZSM-5 and for methane. Based on the kinetic parameters, the recalculated reactivity coefficients for both 1st and 2nd order models are shown in Figure 4.20. It seems the 1st order model shows a higher deviation during the initial 20 min TOS. Therefore, the 2nd order modified GPLE deactivation model is likely a better fit for data extrapolation.

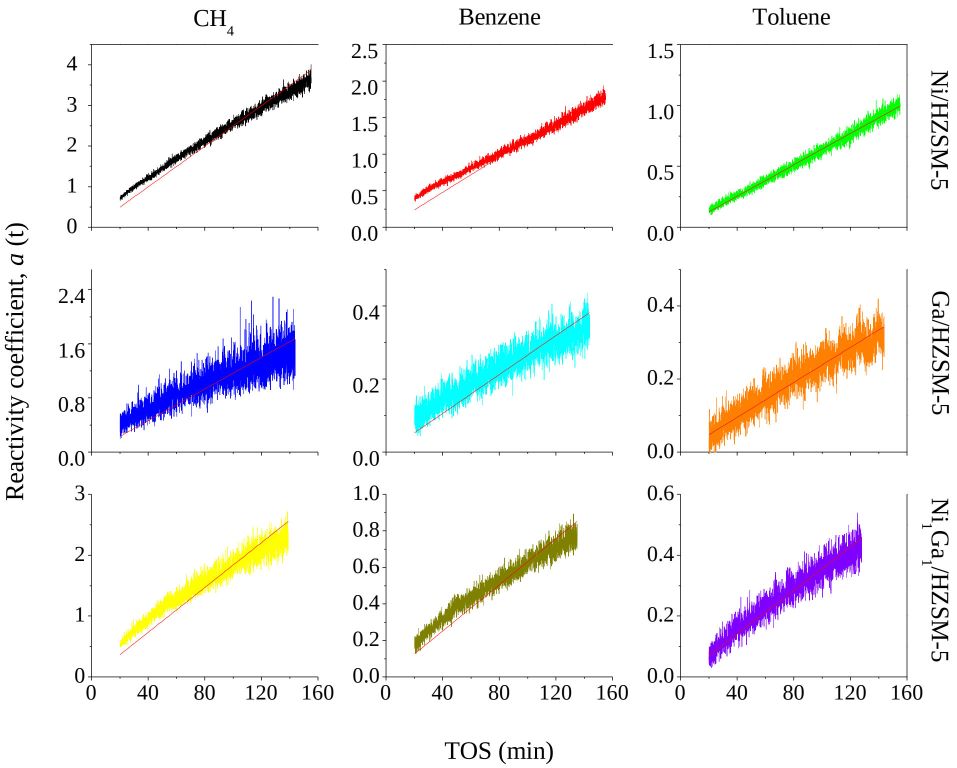

Figure 4.19 Second order deactivation kinetics of ethane aromatization over Ni-HZSM-5, Ga-ZHSM-5, and Ni_1Ga_1-HZSM-5.

Changes of reactivity coefficient a(t) with time for methane, benzene, and toluene. The reaction was performed over 0.2 g of the catalyst (GHSV= 4000 h^{-1}) at 550 °C under atmospheric pressure. The results show dramatic deviation for methane and benzene; however, deviation of toluene sounds to be less significant, comparatively.

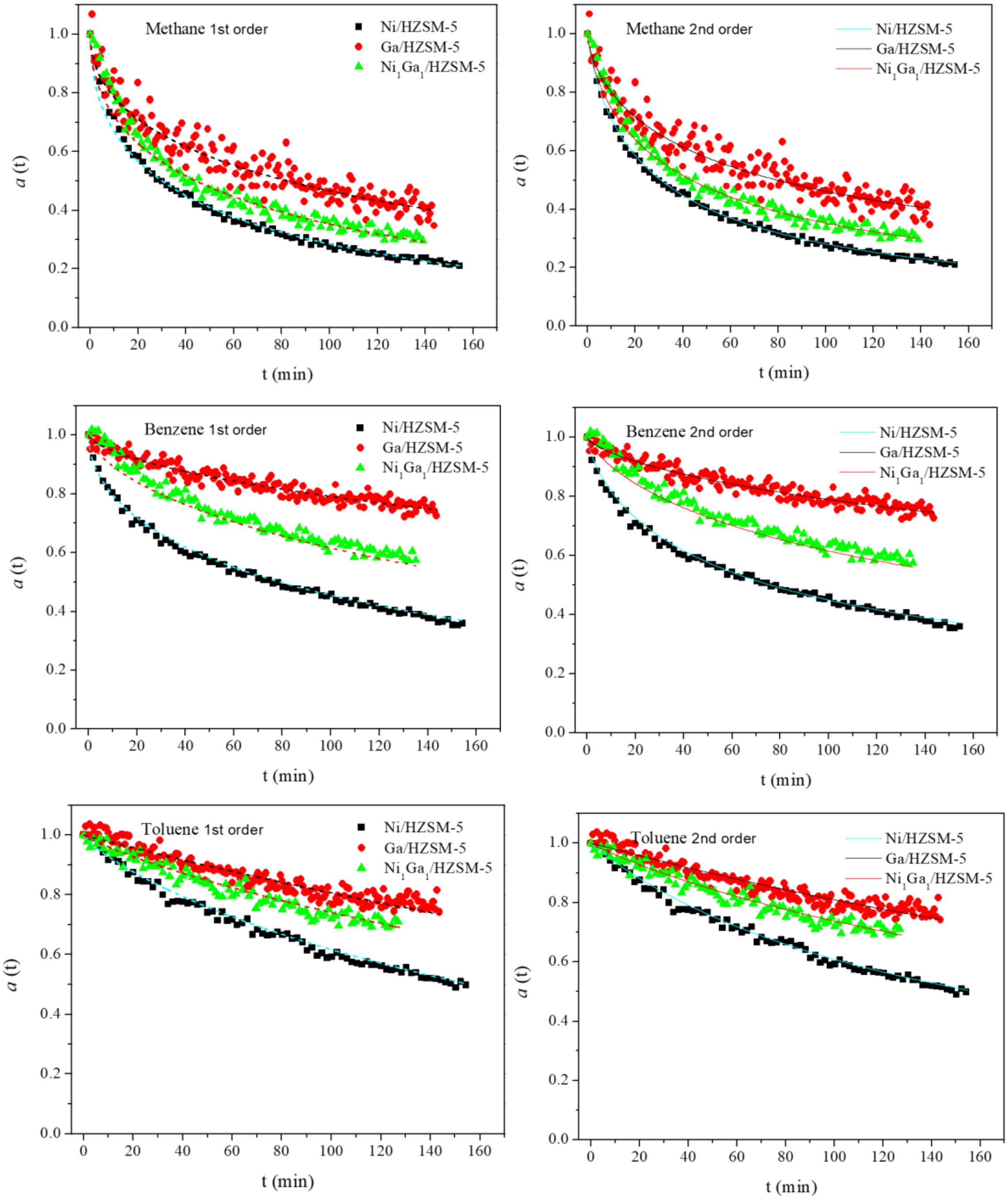

Figure 4.20 Experimental versus calculated values of changes of reactivity coefficient a(t) with time for methane, benzene, and toluene over Ni-HZSM-5, Ga-ZHSM-5, and Ni_1Ga_1-HZSM-5 based on modified first and second order deactivation rate.

The reaction was performed over 0.2 g of the catalyst (GHSV = 4000 h^{-1}) at 550 °C under atmospheric pressure. The 2nd order deactivation model seems to correlate better to experimental data, especially during the first 20 min TOS.

Table 4.3 Deactivation kinetic parameters for 1st and 2nd order modified GPLE model.

		First order: $a(t) = exp(-k_1 t^{\alpha_1})$			Second order: $a(t) = (1 + k_2 t^{\alpha_2})^{-1}$		
		Ni	Ga	Ni_1Ga_1	Ni	Ga	Ni_1Ga_1
M	α	0.5	0.5	0.5	0.79	0.67	0.73
	k	0.129	0.077	0.104	0.066	0.053	0.064
	R2	0.993	0.974	0.966	0.995	0.985	0.969
	t1/2	29	81	44	31	79	43
B	α	0.54	0.62	0.64	0.74	0.68	0.75
	k	0.066	0.013	0.026	0.041	0.012	0.019
	R2	0.991	0.988	0.963	0.987	0.982	0.967
	t1/2	78	561	174	75	685	185
T	α	0.81	0.99	0.86	0.97	1	0.95
	k	0.012	0.002	0.006	0.007	0.002	0.005
	R2	0.998	0.972	0.982	0.986	0.973	0.987
	t1/2	154	324	262	158	395	296

4.5 Conclusion

We have demonstrated that Ni/Ga co-functionalized HZSM-5 catalysts show enhanced selectivity + stability and activity than the monometallic counterparts, i.e., Ni/HZSM-5 and Ga/HZSM-5, respectively, during ethane aromatization. Specifically, with Ni/Ga atomic ratio of 1/1, the selectivity to total BTX is up to 80% (identical to that over the Ga/HZSM-5), which is higher than Ni/HZSM-5 catalyst, as well as the other catalysts reported in the literature. In terms of the activity, the rate of total BTX formation over the Ni_1Ga_1/HZSM-5 (~60 μmol/g/min) is higher than that over the Ga/HZSM-5 (~40 μmol/g/min). Although the Ni/HZSM-5 catalyst shows the highest initial rate of BTX (up to 120 μmol/g/min), such a catalyst deactivates significantly with TOS due to coking. Based on the modified GPLE deactivation kinetic models, the rate constant of deactivation k over the Ni/HZSM-5 is larger than that over Ga and Ni_1Ga_1 modified HZSM-5 catalysts. It seems the metal functions significantly affect the rate constant of deactivation k rather than the power correlation α to time t. Additionally, the metal compositions of the catalysts also show a significant effect on early-stage catalytic behavior. While the Ga and Ni_1Ga_1/HZSM-5 catalysts show an induction period of a few minutes, over the Ni/HZSM-5 and $Ni_1Ga_{1/3}$/HZSM-5 catalyst, it increased to >10 min and >30 min, respectively. Such an induction period is highly undesired since only methane and coke were produced with up to 100% ethane conversion over the Ni/HZSM-5 catalyst.

Detailed characterization of the catalysts suggested that various Ni and Ga related species are presenting in the same catalyst. Specifically, the formation of Ni_3Ga intermetallic alloy particles was identified by both XRD (also evidenced by the XPS, XAS, and STEM-EDS mapping). We suggested that a tandem dehydrogenation (over the Ni_3Ga intermetallic alloy) and aromatization (over the Ga^+ or $[GaO]^+$ exchanged HZSM-5) mechanism was involved in the ethane aromatization. The presence of other Ni species, especially the nanosized Ni particles, which is likely responsible for the long induction period, high rate of coking (fast deactivation), and high selectivity to methane, is not desired.

4.6 References

1. Global Benzene Market Forecast and Opportunities. https://www.techsciresearch.com/report/global-benzenemarket-forecast-and-opportunities-2020/198.html .

2. Future of chemicals. Rebalancing global feedstock disruptions with “on-purpose” technologies. https://www.strategyand.pwc.com/gx/en/reports/future-of-chemicals-viii.pdf .

3. Xiang, Y.; Wang, H.; Cheng, J.; Matsubu, J. Progress and prospects in catalytic ethane aromatization. *Catal. Sci. Technol.* 2018, 8 (6), 1500-1516.

4. Sattler, J. J.; Ruiz-Martinez, J.; Santillan-Jimenez, E.; Weckhuysen, B. M. Catalytic dehydrogenation of light alkanes on metals and metal oxides. *Chem. Rev.* 2014, 114 (20), 10613-53.

5. Chen, N. Y.; Yan, T. Y. M2 forming - a process for aromatization of light hydrocarbons. *Ind. Eng. Chem. Process Des. Dev.* 1986, 25 (1), 151-155.

6. CYCLAR™ Process Produces High-Quality Aromatic Products. https://www.uop.com/cyclar-process-produces-high-quality-aromatic-products/.

7. Guisnet, M.; Gnep, N. S. Mechanism of short-chain alkane transformation over protonic zeolites. Alkylation, disproportionation and aromatization. *Appl. Catal., A* 1996, 146 (1), 33-64.

8. Wakai, T.; Hirabayashi, K.; Kondoh, T.; Inoue, S. On Advanced Catalytic Science and Technology, Proceedings of the Second Tokyo Conference, Tokyo, Japan, 1995.

9. Ono, Y. Transformation of Lower Alkanes into Aromatic Hydrocarbons over ZSM-5 Zeolites. *Catal. Rev.* 1992, 34 (3), 179-226.

10. Kitagawa, H.; Sendoda, Y.; Ono, Y. Transformation of propane into aromatic hydrocarbons over ZSM-5 zeolites. *J. Catal*. 1986, 101 (1), 12-18.

11. Choudhary, V. R.; Kinage, A. K.; Choudhary, T. V. Effective Low-Temperature Aromatization of Ethane over H-Galloaluminosilicate(MFI) Zeolites in the Presence of Higher Alkanes or Olefins. *Angew. Chem., Int. Ed.* 1997, 36 (12), 1305-1308.

12. Ono, Y.; Nakatani, H.; Kitagawa, H.; Suzuki, E. The Role of Metal Cations in the Transformation of Lower Alkanes into Aromatic Hydrocarbons. *Stud. Surf. Sci. Catal.* 1989, 44, 279-290.

13. Bragin, O. V.; Vasina, T. V.; Isakov, Y. I.; Palishkina, N. V.; Preobrazhensky, A. V.; Nefedov, B. K.; Minachev, K. M. Aromatization of Ethane on Metal - Zeolite Catalysts. *Stud. Surf. Sci. Catal.* 1984, 18, 273-278.

14. Bragin, O. V.; Shpiro, E. S.; Preobrazhensky, A. V.; Isaev, S. A.; Vasina, T. V.; Dyusenbina, B. B.; Antoshin, G. V.; Minachev, K. M. The state of platinum in high-silica zeolites and its catalytic activity in ethane and propane aromatization. *Appl. Catal.* 1986, 27 (2), 219-231.

15. Yakerson, V. I.; Vasina, T. V.; Lafer, L. I.; Sytnyk, V. P.; Dykh, G. L.; Mokhov, A. V.; Bragin, O. V.; Minachev, K. M. The properties of zinc and gallium containing pentasils — The catalysts for the aromatization of lower alkanes. *Catal. Lett.* 1989, 3 (4), 339-345.

16. Steinberg, K.-H.; Mroczek, U.; Roessner, F. Aromatization of ethane on platinum containing ZSM-5 zeolites. *Appl. Catal.* 1990, 66 (1), 37-44.

17. Mroczek, U.; Reschetilowski, W.; Pietzsch, K.; Steinberg, K. H. Aromatization of ethane on Pt and Pd supported Zn- and Mn-ZSM-5 zeolites. *React. Kinet. Catal. Lett.* 1991, 43 (2), 539-544.

18. Reschetilowski, W.; Mroczek, U.; Steinberg, K. H.; Wendlandt, K. P. Influence of platinum dispersion on the ethane aromatization on Pt/H-ZSM-5 zeolites. *Appl. Catal.* 1991, 78 (2), 257-264.

19. Schulz, P.; Baerns, M. Aromatization of ethane over gallium-promoted H-ZSM-5 catalysts. *Appl. Catal.* 1991, 78 (1), 15-29.

20. Chetina, O. V.; Vasina, T. V.; Lunin, V. V.; Bragin, O. V. Aromatization of ethane over modified pentasils. *Catal. Today* 1992, 13 (4), 639-643.

21. Roessner, F.; Hagen, A.; Mroczek, U.; Karge, H. G.; Steinberg, K. H. Conversion of Ethane into Aromatic Compounds on Zsm-5 Zeolites Modified by Zinc. *Stud. Surf. Sci. Catal.* 1993, 75, 1707-1710.

22. Chetina, O. V.; Vasina, T. V.; Lunin, V. V. Aromatization of ethane over Pt,Ga/HZSM-5 catalyst and the effect of intermetallic hydrogen acceptor on the reaction. *Appl. Catal., A* 1995, 131 (1), 7-14.

23. Keipert, O. P.; Wolf, D.; Schulz, P.; Baerns, M. Kinetics of ethane aromatization over a gallium-doped H-ZSM-5 catalyst. *Appl. Catal., A* 1995, 131 (2), 347-365.

24. Pierella, L. B.; Eimer, G. A.; Anunziata, O. A. Selective ethane conversion into aromatic hydrocarbons over Zn-ZSM-11 zeolite. *React. Kinet. Catal. Lett.* 1998, 63 (2), 271-278.

25. Solymosi, F.; Szo˝ke, A. Conversion of ethane into benzene on Mo_2C/ZSM-5 catalyst. *Appl. Catal., A* 1998, 166 (1), 225-235.

26. Anunziata, O. A.; Eimer, G. A.; Pierella, L. B. Ethane conversion into aromatic hydrocarbons over molybdenum-containing MEL zeolites. *Appl. Catal., A* 1999, 182 (2), 267-274.

27. Roessner, F.; Hagen, A.; Heemsoth, J. Aromatization of ethane on modified zeolites in the presence of co-reactants. *Stud. Surf. Sci. Catal.* 2000, 130, 2519-2524.

28. Hagen, A.; Roessner, F. Ethane to Aromatic Hydrocarbons: Past, Present, Future. *Catal. Rev.* 2000, 42 (4), 403-437.

29. Krogh, A.; Hagen, A.; Hansen, T. W.; Hviid Christensen, C.; Schmidt, I. Re/HZSM-5: a new catalyst for ethane aromatization with improved stability. *Catal. Commun.* 2003, 4 (12), 627-630.

30. Vosmerikova, L. N.; Barbashin, Y. E.; Vosmerikov, A. V. Catalytic aromatization of ethane on zinc-modified zeolites of various framework types. *Pet. Chem.* 2014, 54 (6), 420-425.

31. Samanta, A.; Bai, X.; Robinson, B.; Chen, H.; Hu, J. Conversion of Light Alkane to Value-Added Chemicals over ZSM-5/Metal Promoted Catalysts. *Ind. Eng. Chem. Res.* 2017, 56 (39), 11006-11012.

32. Bai, X.; Samanta, A.; Robinson, B.; Li, L.; Hu, J. Deactivation Mechanism and Regeneration Study of Ga–Pt Promoted HZSM-5 Catalyst in Ethane Dehydroaromatization. *Ind. Eng. Chem. Res.* 2018, 57 (13), 4505-4513.

33. Mehdad, A.; Lobo, R. F. Ethane and ethylene aromatization on zinc-containing zeolites. *Catal. Sci. Technol.* 2017, 7 (16), 3562-3572.

34. Liang, T.; Toghiani, H.; Xiang, Y. Transient Kinetic Study of Ethane and Ethylene Aromatization over Zinc-Exchanged HZSM-5 Catalyst. *Ind. Eng. Chem. Res.* 2018, 57 (45), 15301-15309.

35. Liang, T.; Fadaeerayeni, S.; Shan, J.; Li, T.; Wang, H.; Cheng, J.; Toghiani, H.; Xiang, Y. Ethane Aromatization over Zn-HZSM-5: Early-Stage Acidity/Performance Relationships and Deactivation Kinetics. *Ind. Eng. Chem. Res.* 2019, 58 (38), 17699-17708.

36. Liu, H.; Wang, H.; Xing, A.-H.; Cheng, J.-H. Effect of Al Distribution in MFI Framework Channels on the Catalytic Performance of Ethane and Ethylene Aromatization. The *J. Phys. Chem. C* 2019, 123 (25), 15637-15647.

37. Ma, L.; Zou, X. Cooperative catalysis of metal and acid functions in Re-HZSM-5 catalysts for ethane dehydroaromatization. *Appl. Catal., B* 2019, 243, 703-710.

38. Anunziata, O. A.; Pierella, L. B. Nature of the active sites in H-ZSM-11 zeolite modified with Zn(2^+) and Ga(3^+). *Catal. Lett.* 1993, 19 (2), 143-151.

39. Shen, W.; Wang, Y.; Shi, X.; Shah, N.; Huggins, F.; Bollineni, S.; Seehra, M.; Huffman, G. Catalytic Nonoxidative Dehydrogenation of Ethane over Fe–Ni and Ni Catalysts Supported on Mg(Al)O to Produce Hydrogen and Easily Purified Carbon Nanotubes. *Energy Fuels* 2007, 21 (6), 3520-3529.

40. Hoang, D.; Berndt, H.; Miessner, H.; Schreier, E.; Völter, J.; Lieske, H. Nickel modified H-ZSM-5 catalysts. *Appl. Catal., A* 1994, 114 (2), 295-311.

41. Kumar, N.; Byggningsbacka, R.; Lindfors, L. E. Aromatization of n-butane over Ni-ZSM-5 and Cu-ZSM-5 zeolite catalysts prepared by using Ni and Cu impregnated silica, fiber. *React. Kinet. Catal. Lett.* 1997, 61 (2), 297-305.

42. Ihm, S. K.; Yi, K. H.; Park, Y. K. Aromatization of n-pentane over Ni-ZSM-5 catalysts. *Stud. Surf. Sci. Catal.* 1994, 84, 1765-1772.

43. Kumar, N.; Byggningsbacka, R.; Lindfors, L. E. Aromatization of n-butane over Ni-ZSM-5 and Cu-ZSM-5 zeolite catalysts prepared by using Ni and Cu impregnated silica, fiber. *React. Kinet. Catal. Lett.* 1997, 61 (2), 297-305.

44. Inui, T.; Makino, Y.; Okazumi, F.; Nagano, S.; Miyamoto, A. Selective aromatization of light paraffins on platinum-ion-exchanged gallium-silicate bifunctional catalysts. *Ind. Eng. Chem. Res.* 1987, 26 (4), 647-652.

45. Fuentes, G. A. Catalyst deactivation and steady-state activity: A generalized power-law equation model. *Appl. Catal.* 1985, 15 (1), 33-40.

46. Levenspiel, O. Experimental search for a simple rate equation to describe deactivating porous catalyst particles. *J. Catal.* 1972, 25 (2), 265-272.

47. Lee, B. J.; Hur, Y. G.; Kim, D. H.; Lee, S. H.; Lee, K. Y. Non-oxidative aromatization and ethylene formation over Ga/HZSM-5 catalysts using a mixed feed of methane and ethane. *Fuel* 2019, 253, 449-459.

48. Liu R. L.; Zhu H. Q.; Wu Zh. V.; Qin Zh. F.; Fan W. B. Wang J. G. Aromatization of propane over Ga-modified ZSM-5 catalysts. *J. Fuel Chem. Technol.* 2015, 43 (8), 961-969.

49. Studt, F.; Sharafutdinov, I.; Abild-Pedersen, F.; Elkjær, C. F.; Hummelshøj, J. S.; Dahl, S.; Chorkendorff, I.; Nørskov, J. K. Discovery of a Ni-Ga catalyst for carbon dioxide reduction to methanol. *Nat. Chem.* 2014, 6, 320.

50. Torelli, D. A.; Francis, S. A.; Crompton, J. C.; Javier, A.; Thompson, J. R.; Brunschwig, B. S.; Soriaga, M. P.; Lewis, N. S. Nickel–Gallium-Catalyzed Electrochemical Reduction of CO_2 to Highly Reduced Products at Low Overpotentials. *ACS Catal.* 2016, 6 (3), 2100-2104.

51. Zhang, D.; Zhao, Y-P; Fan, X.; Liu, Z.; Wang, R-Y; Wei, X-Y. Catalytic Hydrogenation of Levulinic Acid into Gamma-Valerolactone Over Ni/HZSM-5 Catalysts. Catal. Surv. Asia, 22 (2018) 129-135.

52. Xiao, H.; Zhang, J.; Wang, P.; Zhang, Z.; Zhang, Q.; Xie, H.; Yang, G.; Han, Y.; Tan, Y. Mechanistic insight to acidity effects of Ga/HZSM-5 on its activity for propane aromatization. *Rsc Adv.* 2015, 5 (112), 92222-92233.

53. Badrinarayanan, S.; Hegde, R. I.; Balakrishnan, I.; Kulkarni, S. B.; Ratnasamy, P. XPS study of nickel in NiHZSM5 catalysts. *J. Catal.* 1981, 71 (2), 439-442.

54. Xiao, H.; Zhang, J.; Wang, X.; Zhang, Q.; Xie, H.; Han, Y.; Tan, Y. A highly efficient Ga/ZSM-5 catalyst prepared by formic acid impregnation and in situ treatment for propane aromatization. *Catal. Sci. Technol.* 2015, 5 (8), 4081-4090.

55. Kazansky, V. B.; Subbotina, I. R.; van Santen, R. A.; Hensen, E. J. M. DRIFTS study of the chemical state of modifying gallium ions in reduced Ga/ZSM-5 prepared by impregnation. I. Observation of gallium hydrides and application of CO adsorption as a molecular probe for reduced gallium ions. *J. Catal.* 2004, 227 (2), 263-269.

56. Schreiber, M. W.; Plaisance, C. P.; Baumgartl, M.; Reuter, K.; Jentys, A.; Bermejo-Deval, R.; Lercher, J. A. Lewis-Bronsted Acid Pairs in Ga/H-ZSM-5 To Catalyze Dehydrogenation of Light Alkanes. *J. Am. Chem. Soc.* 2018, 140 (14), 4849-4859.

57. Yang, X.; Liu, J.; Fan, K.; Rong, L. Hydrocracking of Jatropha Oil over non-sulfided PTA-NiMo/ZSM-5 Catalyst. *Sci. Rep.* 2017, 7, 41654.

58. Bykova, M. V.; Ermakov, D. Y.; Kaichev, V. V.; Bulavchenko, O. A.; Saraev, A. A.; Lebedev, M. Y.; Yakovlev, V. A. Ni-based sol–gel catalysts as promising systems for crude bio-oil upgrading: Guaiacol hydrodeoxygenation study. *Appl. Catal., B* 2012, 113-114, 296-307.

59. He, Y.; Song, Y.; Cullen, D. A.; Laursen, S. Selective and Stable Non-Noble-Metal Intermetallic Compound Catalyst for the Direct Dehydrogenation of Propane to Propylene. *J Am. Chem. Soc.* 2018, 140 (43), 14010-14014.

60. He, Y.; Song, Y.; Laursen, S. The Origin of the Special Surface and Catalytic Chemistry of Ga-Rich Ni_3Ga in the Direct Dehydrogenation of Ethane. *ACS Catal.* 2019, 10464-10468.

CHAPTER V

MECHANISM AND KINETICS OF ETHANE AROMATIZATION

This chapter is adopted from a published article: Siavash Fadaeerayeni, Genwei Chen, Hossein Toghiani, Yizhi Xiang, Mechanism and Kinetics of Ethane Aromatization According to the Chemical Transient Analysis, Topics in Catalysis 63: (2020) 1463–1473.

5.1 Introduction

Hydrocarbons trapped in impermeable rocks can now be extracted with horizontal drilling and hydraulic fracturing [1], which provide cheap and abundant light alkanes. The production of C_2-C_5 light alkanes (known as natural gas liquids, NGLs) alone in the US has increased to 5145 thousand barrels/day in January 2020 [2]. The unprecedented increase in NGLs production benefits the global chemical sector by shifting the raw materials from naphtha to the cheaper light alkanes. Consequently, the production of aromatic BTX (benzene, toluene, and xylene) is reduced, which requires the development of "on-purpose" techniques for light alkanes aromatization [3,4].

The catalytic process of C_3-C_5 alkanes aromatization was observed in 1970 over a Pt/Al_2O_3 catalyst [5,6]. Until the late 1990s, several industrial processes such as Cyclar, Aroforming, Z-forming, M2 forming, which use C_3-C_6 alkanes as the reactant, have been developed [7]. However, an efficient catalyst for ethane aromatization remains a formidable challenge, which is most probably due to the lack of understanding about the mechanism and kinetics, as well as the catalytically active sites. Because ethane has been used exclusively for steam cracking in the industry, the catalytic processes of ethane conversion have been less concerned during the past several decades.

There is a general consensus that ethane aromatization requires a dual-functional catalyst consisting of metal species for the initial C-H bond activation and dehydrogenation, and HZSM-5 zeolite acidic sites for oligomerization and cyclization [3,8]. The MFI framework structure of the HZSM-5 also provides shape selectivity, prohibiting the formation of polyaromatic species. Unlike C_{3+} alkanes aromatization, in which the zeolite Brønsted acid sites are active for alkane activation, negligible ethane activation on parent HZSM-5 reveals the critical role of the metal species. Pt [9-11], Zn [12-14], Ga [15,16], Re [17], and Mo [18,19] modified HZSM-5 catalysts have been widely studied for ethane aromatization, among which Zn and Pt were most concerned. Zinc species in HZSM-5 inclined to replace the proton, forming Zn (II) cations as the Lewis acid site [20]. The activity of the Zn/HZSM-5 catalyst in ethane aromatization highly depends on the ratio between Zn (II) Lewis and H^+ Brønsted acid sites [13]. Zinc (II) species were also anticipated to facilitate the recombination of the H radicals to H_2 [21-23]. Different from zinc, platinum species in HZSM-5 form Pt^0 nanoparticles or clusters [24]. The Pt^0 shows a high affinity for the paraffinic C-H bond, which renders its exceptional performance in catalyzing the C-H bond activation. However, the Pt^0 clusters also show higher activity for the C-C bond scission, which not only resulted in CH_4 formation through hydrogenolysis but also led to coke deposition via cracking [25]. Nonetheless, the C-C bond scission might be reduced through PtM alloy formation [26]. While the Pt and Zn modified HZSM-5 catalysts were frequently studied for ethane aromatization, further information about the mechanism and kinetics has been less involved.

Transient method consists of analyzing the composition of the reactor outlet after a step or pulse perturbation of reactant partial pressures could provide extensive catalyst surface information about the abundancy of surface chemisorbed species (θ_i) and their kinetic reactivity (k or τ) [27-29]. As pointed out by Kruse and coworkers, "an analysis of the steady-state kinetics will most probably be corroborative rather than conclusive and that a detailed kinetic analysis along with the identification of "bottlenecks" or "spectators" can only be provided by applying transient methods" [30], which was previously also mentioned by M. Boudart [31,27]. Various heterogeneous catalytic systems, such as methane dry reforming [32,33], CO oxidation [34], water gas shift reaction [35], and CO hydrogenation [30,36-42], have been frequently studied by the transient method. Based on the molar balance of the reactor system, Kruse and coworkers developed a method for surface atoms "counting", which provided substantial mechanistic information (CO insertion mechanism) of the chain-lengthening during CO hydrogenation [37,39]. However, the application of transient methods to light alkanes conversion has been less involved, which mainly focused on the isotopic (D_2) exchanges to probe the kinetics of C-H bond activation [43-45].

The transient methods have been recently studied for ethane aromatization [46-48] and ammoxidation [49] in our group. Here we are focusing on the kinetics and mechanism of ethane aromatization based on the transient method. Specifically, the build-up and back-transient behavior of ethane aromatization over the representative Zn-HZSM-5 and Pt/HZSM-5 catalysts will be extensively discussed. Additionally, the reaction transient between propane and ethane aromatization over the Zn-HZSM-5 catalyst, as well as the chemical transient kinetics of ethylene oligomerization over the Pt/HZSM-5 catalyst will also be investigated.

5.2 Experimental

5.2.1 Catalyst Preparation

The NH_4-ZSM-5 zeolite (specific area 400 m^2/g, $SiO_2/Al_2O_3=30$) was purchased from Alfa Aesar. The Zn modified HZSM-5 catalyst was prepared through ion exchange. Typically, a calculated amount of 0.05 M aqueous solution of zinc nitrate was added to 2.5 g of NH_4-ZSM-5 zeolite and kept at 80°C under the reflux condition for 7 h before being centrifuged and washed with water for several times. This process was repeated three times to make sure that the majority of protonic sites of zeolite were exchanged with zinc (II) cations. Finally, the obtained catalyst was dried at 120 °C overnight and calcined in air at 550 °C for 6 h. The Pt modified HZSM-5 catalyst was prepared through incipient wetness impregnation. The same zeolite (2 g) was dried under vacuum at 100^oC for 6 h, then impregnated with an aqueous solution of tetraammineplatinum nitrate solution (2 ml) at room temperature to obtain 0.05 wt% nominal Pt loading. The obtained sample was kept in a vacuum oven at 60 ^oC for 12 h for drying and calcined under air at 560 ^oC for 6 h. The powder sample was then formed through tablet press, crushed, and sieved to obtain a size fraction between 125 and 250 µm for the chemical transient analysis. The obtained powder samples were subjected to electron microscopy (TEM) characterization using JEOL 2100TEM (accelerating voltage of 200 kV) equipped with a Gatan camera.

5.2.2 Chemical Transient Tests

The chemical transient tests of ethane aromatization over the Zn-HZSM-5 and Pt/HZSM-5 catalysts (or ethylene oligomerization over the Pt/HZSM-5) were performed in a home-built setup, allowing step perturbation of reactant partial pressures. Typically, 0.1 g of the catalyst was loaded into the quartz reactor (ID, Φ = ¼ inches) and activated in 20 ml/min Ar (for Zn-HZSM-5) and 10% H_2 (for Pt/HZSM-5) at 600 °C (10 °C/min) for 30 min. After activation, the temperature of the reactor was decreased to 550 °C (260 ^oC for ethylene oligomerization) for the transient tests. Prior to each test, Ar and reactant by-pass spectra were recorded for mass spectrometer calibration and used as a reference for the calculation of the partial pressure of products. Then the reaction was initiated by abruptly switching of the influent gas from inert (Ar or N_2) to C_2H_6 or C_2H_4/Ar at the same total flow of 20 ml/min (GHSV=8000 h^{-1}). During such a process, the clean catalyst surface runs through an induction period (hydrocarbon pool build-up) and finally reaches the steady-state. The reaction was kept at steady-state for a short time-on-stream, then stopped by switching the influent gas back to inert (known as back-transient or hydrocarbon-pool clean up). The composition of the reactor outlet during both build-up and back-transient was measured by an online mass spectrometer (Agilent MS 5973 (EI source, Mass Range 2-800 amu) equipped with MS Sensor 2.0 software (Diablo Analytical, Inc.)). A more detailed quantification method for analyzing the components with the mass spectrometer as well as theoretical background behinds the back-transient kinetic data evaluation has been explained elsewhere [46].

The reaction transient between ethane and propane aromatization was performed in the same setup mentioned above. Instead of switching between inert and ethane, the reactor influent was switched forth and back between propane and ethane aromatization after the steady-state was reached. The reaction transient was performed over the Zn-HZSM-5 catalyst under the same reaction conditions mentioned above.

5.3 Results and Discussion

5.3.1 Characterization and Steady-State Performance

The Zn and Pt modified HZSM-5 catalysts are well known for ethane aromatization, as well as the other reactions for hydrocarbon processing. The chemical properties of the Zn-HZSM-5 catalyst have been extensively studied during our previous study by N_2 physisorption, ammonia temperature-programmed desorption (NH_3-TPD), n-propylamine temperature-programmed decomposition ($C_3H_7NH_2$-TPDec), scanning transmission electron microscopy (STEM-EDS), and X-ray absorption near-edge structure (XANES) [46, 47]. The TEM image of the Zn-HZSM-5 catalyst shown in Figure 5.1 (a) suggested the absence of ZnO nanoparticles when prepared by ion exchange. The presence of Zn was confirmed by the STEM-EDS mapping (see Figure 5.1 (b)), where the homogeneous distribution of the Zn species (~1.3 wt% according to EDS) was observed over the entire range of the zeolite. The chemical state of the Zn species, according to the XANES spectra, suggested the formation of Zn (II) cation (balanced by the negatively charged framework AlO_4^- tetrahedra) for both fresh and used catalysts. Further discussion about the properties of the Zn-HZSM-5 can be found in our previous study [46, 47]. Unlike the Zn-HZSM-5 catalyst, the 0.05 wt% Pt/HZSM-5 prepared by impregnation shows the formation of Pt nanoparticles, ~2 nm (see Figure 5.1 (c)). However, further characterization of the Pt/HZSM-5 catalyst was largely limited due to the low Pt loading. Nonetheless, characterization of the 0.5 wt% Pt/HZSM-5 by XANES and EXAFS (results are not shown here) suggested the presence of metallic Pt and the absence of Pt-O bond that represents the single atom/cluster bound to the zeolite framework.

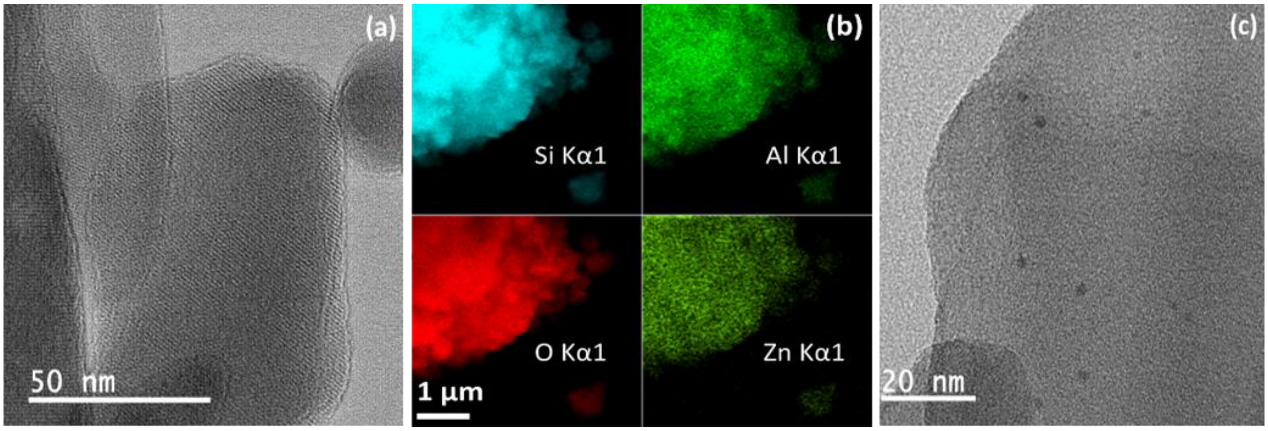

Figure 5.1 Electron microscopy characterization of the Zn and Pt modified HZSM-5 catalysts. (a) TEM image of Zn-ZSM-5, (b) STEM-EDS mapping of Zn-HZSM-5, and (c) TEM image of 0.05 wt% Pt/HZSM-5.

The catalytic performance under steady-state for the involved transient studies is shown in Table 5.1. For ethane aromatization, the activity of the Pt/HZSM-5 is higher (more than 20 times if the normalize the rate by the mass of the active species) than the Zn-HZSM-5. Specifically, the Pt/HZSM-5 shows the formation of quite a lot of C_3-C_6 alkanes and alkene (3.16 μmol/g_{Cat}/s), which was almost absent from the Zn-HZSM-5 catalyst. For ethylene oligomerization over the Pt/HZSM-5 at 260 °C, the formation of aromatics was negligible (~0.29 μmol/g_{Cat}/s); however, the overall rate of ethylene to higher C_3-C_6 alkanes and alkene was up to 60.6 μmol/g_{Cat}/s. Additionally, propane aromatization over the Zn-HZSM-5 shows significantly higher activity than that for ethane aromatization. The rates of benzene, toluene, and xylene are 3.41, 8.66, and 9.76 μmol/g_{Cat}/s, respectively. The obtained rates for different products at steady-state were subjected to the intracrystalline diffusion [50] analysis by the Weisz-Prater criterion. Assume the effective diffusivities of light hydrocarbons and aromatics are in the range of 1E-11 m^2/s, and 1E-13 m^2/s, respectively, the Weisz-Prater numbers calculated based on the first-order reaction kinetics are all well below 1 for ethane aromatization and ethylene oligomerization. However, a slight diffusion influence is expected for propane aromatization due to the higher rate of aromatics. The detailed process of the intracrystalline diffusion analysis by the Weisz-Prater criterion can be found in our previous work [51].

Table 5.1 The rate for the formation of different products under steady-state (TOS 10 min) for the involved transient studies.

Feed	Cat.	T (ºC)	Rate (μmol/g_{Cat}/s)						
			CH_4	C_2H_4	C_3H_6	Benzene	Toluene	Xylene	Others
C_2H_6	Pt/HZSM-5	550	0.86	3.44	1.20	0.34	1.63	0.66	1.96
C_2H_6	Zn-HZSM-5	550	0.35	1.91	/	0.48	1.0	0.22	/
C_2H_4	Pt/HZSM-5	260	/	/	10.69	0.054	0.066	0.17	49.91
C_3H_8	Zn-HZSM-5	550	6.85	6.41	7.15	3.41	8.66	9.76	3.92

5.3.2 Build-up: Formation of Catalyst-Bound Intermediates

The build-up refers to a transient state/induction period during which active intermediates were formed on the catalytically active sites, i.e., from the clean catalyst surface to adsorption/desorption/surface reaction of intermediates at equilibrium. The reconstruction of the active phase might be involved depending upon the phase stability of the active sites towards changing chemical ambient. Quantitative analysis based on the time-dependent molar balance could provide significant mechanistic aspects regarding the abundancy of various surface intermediate [37,39]

The catalytic behavior during the build-up for ethane aromatization over the Zn-HZSM-5 catalyst has been discussed in our previous study [46]. The difference between the Zn-HZSM-5 and Pt/HZM-5 will be discussed herein, and the normalized build-up signals are depicted in Figure 5.2, panels (a), (b), (d), and (e). As we can see, over both catalysts, ethylene appears immediately in the gas phase and reaches the maximum within 5 s after exposing the clean catalyst surface to ethane, indicating that dehydrogenation is the first step of ethane aromatization. Methane also appears in the gas phase without delay over both catalysts. However, it takes a slightly longer time to reach the maximum over the Zn-HZSM-5 (10 s) than that over the Pt/HZSM-5 (5 s) since Pt particles/clusters show higher activity in hydrogenolysis ($C_2H_4 + 2H_2 \rightarrow 2CH_4$ or $C_2H_6 + H_2 \rightarrow 2CH_4$) than the Zn (II) cations. Cracking of ethylene ($C_2H_4 \rightarrow C + CH_4$) might be another route for methane formation and coke deposition over the Zn-HZSM-5 catalyst [46]. Quite similar to ethane, the C_{3+}-hydrocarbons appear in the gas phase with only a slight delay (5 s) over the Pt/HZSM-5 catalyst, but the latter takes a slightly longer time to reach steady-state probably due to the intercrystalline configurational diffusion [50]. Additionally, simultaneous observation of C_{3+} alkanes and alkenes in the gas phase suggested that the oligomerization/cracking, hydrogenation/dehydrogenation, and hydride transfer involved in the hydrocarbon-pool build up are very fast surface-reaction steps. Desorption and internal diffusion most probably is the rate-limiting step for oligomerization [51]. It must be noted that the C_{3+}-hydrocarbons are almost absent over the Zn-HZSM-5 catalyst. A plausible reaction network of ethane aromatization has been shown in our previous study [46]

Unlike the light hydrocarbons, in which quite similar build-up behaviors were observed over the Pt/HZSM-5 and Zn-HZSM-5 catalysts, the delay of aromatics over the two catalysts is different. Over the Pt/HZSM-5 catalyst (as shown in Figure 5.2 (b)), while benzene appears in the gas phase immediately like the light hydrocarbons (almost identical to ethane), a slightly delay (5 s) of toluene and xylene was observed, indicating different mechanisms might be involved for the formation of benzene and toluene/xylene. We suggested that the formation of benzene from C_6 carbocations originated from ethylene oligomerization, but the formation of toluene and xylene from C_7 and C_8 intermediates requires the co-oligomerization between ethylene and propylene

[46]. Additionally, the production of benzene, toluene, and xylene reach steady-state after 10, 50, and 70 s, respectively, which are significantly longer than that for light hydrocarbons most probably due to the intracrystalline diffusion mentioned above [50].

The build-up behavior of aromatics over the Zn-HZSM-5 catalyst (see Figure 5.2 (e)) shows a longer delay time than that over the Pt/HZSM-5. The delay times for benzene, toluene, and xylene are 5, 8, and 10 s, respectively, and they reach steady-state or maximum after 20, 50, and 80 s, respectively. Benzene shows a significant decay from 20 to 80 s, indicating fast deactivation or significant changes in the compositions of the hydrocarbon-pool species. Nonetheless, considering the overall similar build-up features except for a shift of abscissa, we suggest the same reaction mechanism/network be involved for both catalysts regardless of the different delays of aromatics. The Pt^0 clusters/particles in the Pt/HZSM-5, in contrast to the Zn(II) Lewis acid site in the Zn-HZSM-5, own a higher activity on the C-H bond activation/dehydrogenation. In addition, a higher population of the Brønsted acid site was retained over the Pt/HZSM-5, ensuring high activity on the oligomerization/cracking of olefins. Therefore, the Pt/HZSM-5 shows a shorter build-up than the Zn-HZSM-5.

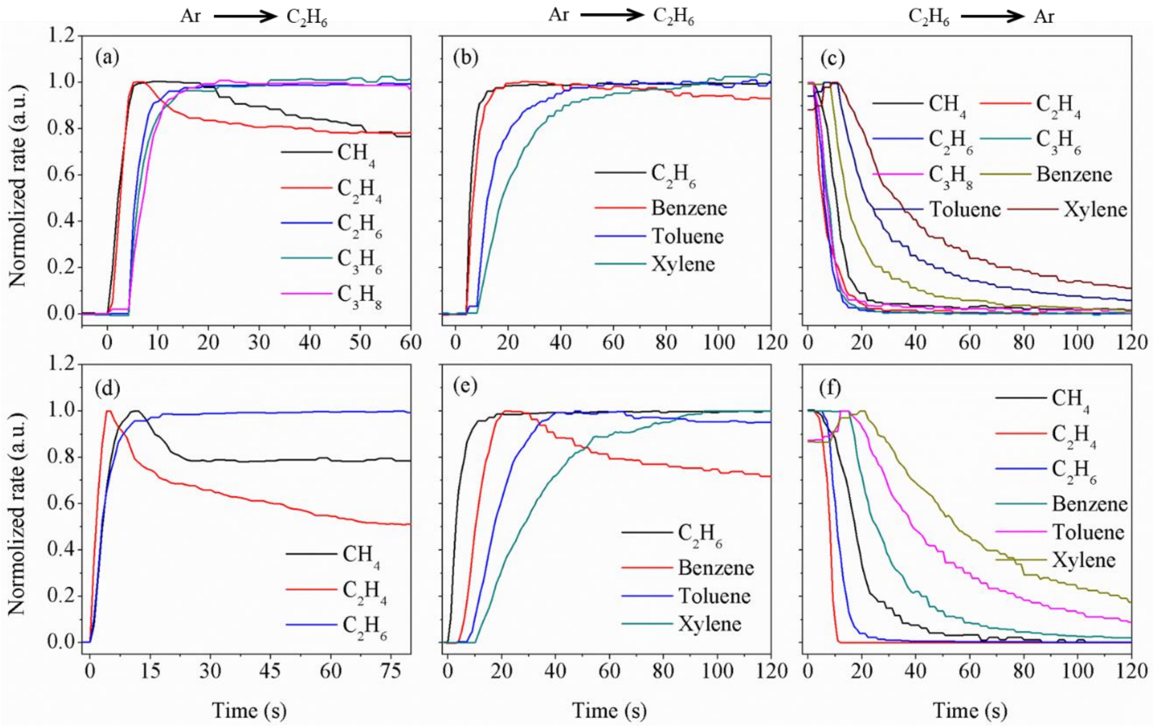

Figure 5.2 Chemical transient of ethane aromatization over the Pt/HZSM-5 (a-c) and Zn-HZSM-5 (d-f) catalysts.

The tests were performed at 550 ˚C over 0.1 g of the catalyst under atmospheric pressure. At t = 0, the reactor influent was abruptly switched from Ar to C_2H_6 for the build-up (a, b, d, e), and switched from C_2H_6 back to Ar for the back-transient (c, f).

5.3.3 Back-Transient: Activate Intermediates Clean up

The back-transient represents the transition from steady-state to clean catalyst surface. The active intermediates are being cleaned up through desorption and surface reaction after abruptly replacing the reactant with an inert. Assume first-order reaction/desorption kinetics, the observed rate (r_i) during the back-transient can be correlated to the rate during steady-state (r_{i0}) and time (t) through the following equation [46].

$$r_i = r_{i0}e^{-\frac{t}{\tau}} \tag{5.1}$$

where τ is the time constant and τ=1/k.

The back-transient results over the Pt/HZSM-5 and Zn-HZSM-5 catalysts are shown in Figure 5.2 (c) and (f), respectively, and the rate constants for BTX formation calculated based on the linear relationship, $\ln(r_i) = \ln(r_{i0}) - kt$, are shown in Table 5.2. As shown in Figure 5.2 (c), significantly different time constants τ were observed among the products. While the decay of the light hydrocarbons is almost identical, the τ for benzene, toluene, and xylene was much larger. The rate constants k for benzene, toluene, and xylene are 0.065, 0.047, and 0.031 s^{-1}, respectively, over the Pt/HZSM-5 catalyst. The time constants τ for different products over the Zn-HZSM-5 are larger than the same product over the Pt/HZSM-5 catalyst. The rate constants k for benzene, toluene, and xylene are 0.054, 0.026, and 0.017 s^{-1}, respectively, over the Zn-HZSM-5 catalyst. Therefore, it again suggests that the Pt^0 clusters/particles in the Pt/HZSM-5 are more active than the Zn(II) Lewis acid site in the Zn-HZSM-5 for aromatics formation from the hydrocarbon-pool species. Additionally, over the Zn-HZSM-5 catalyst, the τ of methane is also much larger than that over the Pt/HZSM-5, which might suggest different mechanisms as indicated by the build-up behavior. It is also worth mentioning that the observed rate constants from the back transient represent the global rate constant from the chemisorbed intermediates, which including surface reaction, desorption and diffusion, therefore could be influenced by the intracrystalline diffusion. Since the diffusion limitation could be negligible according to the Weisz-Prater criterion, the k value could be the rate constant of surface reaction or the desorption constant depending on which is the limiting step. Therefore, the intrinsic rate constants for aromatics must be lower than the value observed from the back-transient. Specifically, we do not expect such a big difference in the k among benzene, toluene, and xylene should the intracrystalline diffusion is absent.

Table 5.2 Kinetic parameters of the back-transients of ethane/propane aromatization over the Zn-HZSM-5 and Pt/HZSM-5 catalyst

Catalyst	Transient	Benzene			Toluene			Xylene		
		τ (s)	k (s^{-1})	σ^2	τ (s)	k (s^{-1})	σ^2	τ (s)	k (s^{-1})	σ^2
Zn-HZSM-5	C_2H_6 to Ar	18	0.054	0.95	38	0.026	0.98	58	0.017	0.99
	C_3H_8 to C_2H_6	35	/		149	/		89	/	
	C_3H_8 to Ar	29	0.035	0.98	116	0.0086	0.99	65	0.015	0.99
Pt/HZSM-5	C_2H_6 to Ar	15	0.065	0.95	21	0.047	0.98	32	0.031	0.97

5.3.4 Reaction Transient of Ethane/Propane Aromatization

While the transient between steady-state and inert provides a global rate constant for the formation of BTX from the “lumped hydrocarbon-pool”, further information can be obtained from the reaction transient between ethane and propane aromatization. Figure 5.3 (a) shows the reaction transient from steady-state propane to ethane aromatization over the Zn-HZSM-5 catalyst, and the normalized signals for different species are shown in Figure 5.3 (d). Quite similar to the back-transient from steady-state ethane aromatization to clean catalyst surface, all of the product’s decay after switching from propane to ethane. The “time constants” τ (see Table 5.2) for the decay of benzene, toluene, and xylene are 35, 149, and 89 s, respectively. However, the other light hydrocarbons (methane, ethylene, and propylene) decreased to the level of steady-state ethane aromatization immediately. Although the “τ” values for aromatics were still obtained from the linear relationship, $\ln(r_i) = \ln(r_{i0}) - kt$, it doesn’t truly represent the kinetic behavior since the switching from propane to ethane resulted in a kinetic model different from equation (1), which cannot be evaluated quantitatively. Indeed, such a reaction transient can be considered as a combination of the back-transient of propane aromatization and the build-up of ethane aromatization, which cannot be deconvoluted quantitatively.

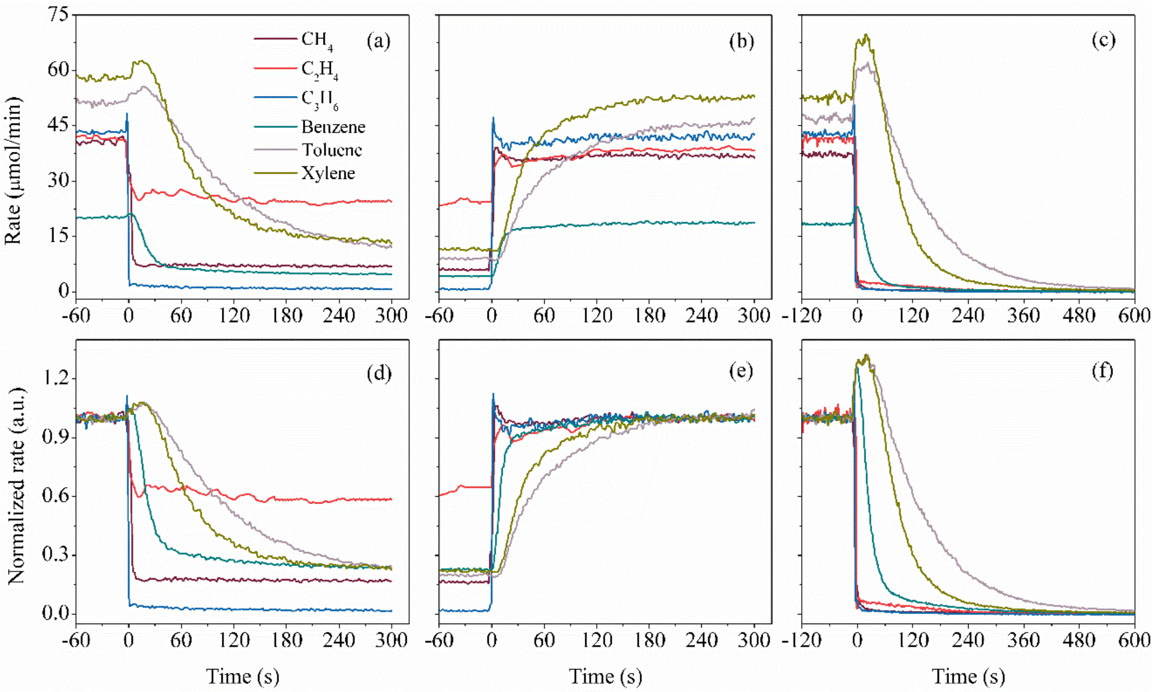

Figure 5.3 Reaction transient between ethane and propane aromatization over the Zn-HZSM-5 catalyst.

The tests were performed at 550 ˚C over 0.1 g of the Zn-HZSM-5 under atmospheric pressure.

The decay of the product was observed due to the change of concentration and reactivity of the surface adsorbed hydrocarbon species after replacing the C_3-derived surface intermediates by that C_2-derived. Propane is more active than ethane in dehydrogenation, which can also be activated through cracking over the Brønsted acid sites of zeolites ($C_3H_8 \rightarrow CH_4 + C_2H_4$) [22,52-54,55]. Therefore, the concentration of the “lumped hydrocarbon-pool”, which leads to the formation of BTX, is likely lower during ethane aromatization than that for propane. The types of hydrocarbon species are different, which also resulted in different product selectivity and reactivity between ethane and propane aromatization. The normalized signals in Figure 5.3 (d) show that the rates of BTX, ethylene, and methane during the steady-state ethane aromatization are 23%, 58%, and 17%, respectively, of that during propane aromatization.

The reaction transient from steady-state ethane back to propane aromatization resulted in the recovery of the products. As shown in Figures 5.3 (b) and (e), methane, ethylene, and propylene reach the steady-state of propane aromatization after about 20 s. Before the steady-state, they all run into maximum immediately after switching from ethane to propane, which is most probably due to the fact that such a transient can be considered as a combination of the back-transient of ethane aromatization and the build-up of propane aromatization. While the rate of benzene starts to increase immediately, toluene and xylene were both delayed for 8 s, which is quite similar to the build-up of ethane aromatization. The aromatics reach the steady-state propane aromatization after about 180 s, significantly longer than the build-up of ethane aromatization.

The back-transient of propane aromatization was shown in Figure 5.3 (c) and (f), in contrast to the reaction transient from steady-state propane to ethane aromatization. The overall feature of the back-transient to inert is quite similar to the reaction transient to ethane. However, the time constants τ of the BTX for the back-transient are smaller (by ~20-30%) than the reaction transient (see Table 5.2). The rate constants for benzene, toluene, and xylene from the back-transient are 0.035, 0.0086, and 0.015 s^{-1}, respectively, which are lower than that for ethane aromatization. Notably, the rate constant of toluene from the "lumped hydrocarbon pool" during ethane aromatization is ~3 times that during propane aromatization. Therefore, the catalytic mechanisms for aromatics formation during ethane and propane aromatization might be different. For example, aromatics might be produced from either dehydrogenation or hydride transfer of the cycloalkanes precursor. Additionally, disproportionation and alkylation/de-alkylation of the aromatics must also be involved. During propane aromatization, the higher activity of the initial dehydrogenation (to propylene) and cracking (to ethylene and methane) resulted in a high partial pressure of olefins. Consequently, the concentration of various hydrocarbon species confined in the micropore of the catalyst must be higher during propane aromatization than that for ethane, which not only decreased the population of the vacancy metal-sites for the final dehydrogenation/hydride transfer but also might increase the influence of the intracrystalline diffusion.

5.3.5 C_2H_4 Oligomerization Over The Pt/HZSM-5

Ethylene was the first intermediate produced from ethane aromatization based on the build-up transient. Oligomerization/cracking and dehydrogenation/hydride transfer of olefins derived from ethylene provided the “lumped hydrocarbon-pool” as the intermediates for aromatics. Therefore, ethylene oligomerization over the Pt/HZSM-5 catalyst has been studied with the transient method at relatively low temperature (260 ^{o}C), where the formation of aromatics at steady-state was negligible. Our recent study suggested a dual-cycle hydrocarbon-pool mechanism to be involved in ethylene oligomerization over the Brønsted acid sites of the HZSM-5 zeolite [51]. The mechanism is most probably the same as the Pt/HZSM-5 catalyst for ethylene oligomerization and ethane aromatization, although the Pt^0 clusters/particles may favor the dehydrogenation rather than hydride transfer. Figure 5.4 (a) shows the build-up of ethylene oligomerization (from clean catalyst surface to steady-state). All of the products run at a maximum during the build-up, which is significantly higher than the corresponding rates at steady-state. The higher reaction rate during the build-up might be explained by the higher availability of the catalytically active sites, i.e., corresponding to a smaller value in the denominator of the common rate expression “$1+\Sigma K_i P_i$”, or in another word, the concentration of the chemisorbed hydrocarbon species remains small. Additionally, the rising surface temperature of the catalyst resulted from the strong chemisorption of ethylene could also contribute to the enhanced activity during the build-up. This assumption was further supported by the absence of such “overshoot” during the build-up of ethane aromatization since the initial ethane dehydrogenation is an endothermic reaction.

Moreover, the maximum rates of alkanes (propane and butane) during the build-up are higher than the corresponding olefins. The alkanes were decreased significantly with time and nearly absent after reaching the steady-state, indicating the mechanism during the build-up is different from the steady-state. During the build-up, the chemisorbed ethylene went through oligomerization/cracking, cyclization, and dehydrogenation/hydride transfer on the “clean” catalyst surface, during which the “hydrocarbon-pool” containing various olefins, monocyclic and bicyclic alkyl-arenes in equilibrium was established. Delay of ethylene with respect to Ar inert standard is also a strong indication for the “hydrocarbon-pool” formation with the consumption of ethylene. Additionally, all of the alkanes and olefins appear in the gas phase simultaneously as Ar, indicating the oligomerization, cyclization, and hydride transfer are very fast reaction steps. However, olefins take a longer time to reach the maximum and steady-state, and aromatics were absent from the build-up, which further suggested that desorption could be the rate-limiting step and the intracrystalline diffusion might be the reason for the extended build-up.

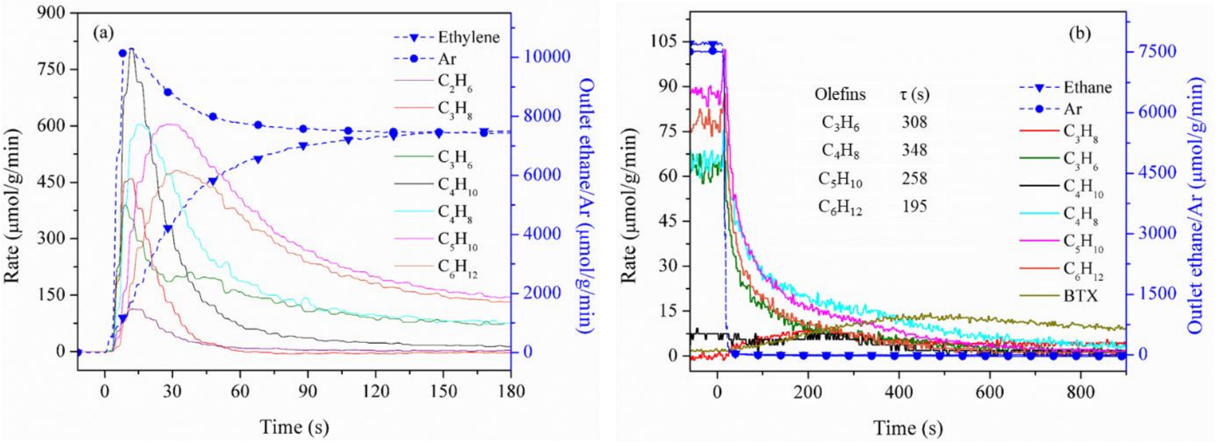

Figure 5.4 Chemical transient of ethylene oligomerization over the Pt/HZSM-5 catalyst.

At t = 0, the reactor influent was abruptly switched from N_2 to C_2H_4 for the build-up (a) and switched from C_2H_4 back to N_2 for the back-transient (b). The tests were performed at 260 ˚C over 0.1 g of the catalyst under atmospheric pressure.

Further information about the desorption/surface reaction of the “hydrocarbon-pool” species can be obtained from back-transient behavior. As depicted in Figure 5.4 (b), C_3-C_6 olefins, aromatics (mainly xylene), and a very small amount of alkanes were desorbed after ethylene was absent from the gas phase. While the decay of olefins follows the first-order kinetic shown in equation (1), both alkanes and aromatics were run into a maximum after ~3 and 7 min, respectively. Since aromatics and alkanes were almost absent during the steady-state, the back-transient might favor the hydride transfer due to the absence of ethylene. The time constants τ for the C_3-C_6 olefins formation from the “lumped hydrocarbon-pool” are ranging from 195-349 s. The τ values for the C_3 and C_4 olefins are larger than that for the C_5 and C_6, indicating the presence of secondary reactions, such as higher olefins cracking and de-alkylation of the monocyclic and bicyclic alkyl-arenes.

5.4 Conclusions and prospects

The above transient analysis based on the step-perturbation for ethane/propane aromatization and ethylene oligomerization provided important information about the kinetics and mechanism of the light alkanes aromatization over the Pt and Zn modified HZSM-5 catalyst. The proposed reaction networks are shown in Figure 4.5. Based on the build-up of ethane aromatization over the Pt/HZSM-5 and Zn-HZSM-5 catalyst, ethylene is the first product that appears in the gas phase, indicating activation of the C-H bond through dehydrogenation (over the Pt^0 or Zn (II) metal sites) is the first reaction step. The produced ethylene was then oligomerized to form $C_4H_9^+ \cdot AlO_4^-$ dimer via the reaction of the protonated (with the Brønsted acid sites of the zeolites) $C_2H_5^+ \cdot AlO_4^-$ with another ethylene molecular from the gas phase [56]. Based on the transient study of ethylene oligomerization, a hydrocarbon-pool containing mixed olefins, monocyclic and bicyclic alkyl-arenes or carbocations was formed during the build-up through cyclization and dehydrogenation/hydride transfer [51]. The formation of hydrocarbon-pool species from ethylene is very fast in contrast to the initial ethane dehydrogenation and the formation of aromatics through hydride transfer or dehydrogenation. The global rate constants for the formation of benzene, toluene, and xylene from the "lumped hydrocarbon-pool" species can be obtained from the first-order kinetic model of the back-transient. Such rate constants might be influenced by the intracrystalline diffusion of aromatics as well as the desorption/re-adsorption of the hydrocarbon species (the dual-cycle hydrocarbon-pool mechanism involves autocatalytic steps; the chemisorbed precursors of aromatics were replenished by the hydrocarbons from the autocatalytic steps). Therefore, the global rate constants from the back-transient should be lower than the rate constants for the dehydrogenation/hydride transfer of the aromatics' precursors. Consequently, the back-transient signals deviated from the linear kinetic model, $\ln(r_i) = \ln(r_{i0}) - kt$, during the "early-stage" of the back-transient.

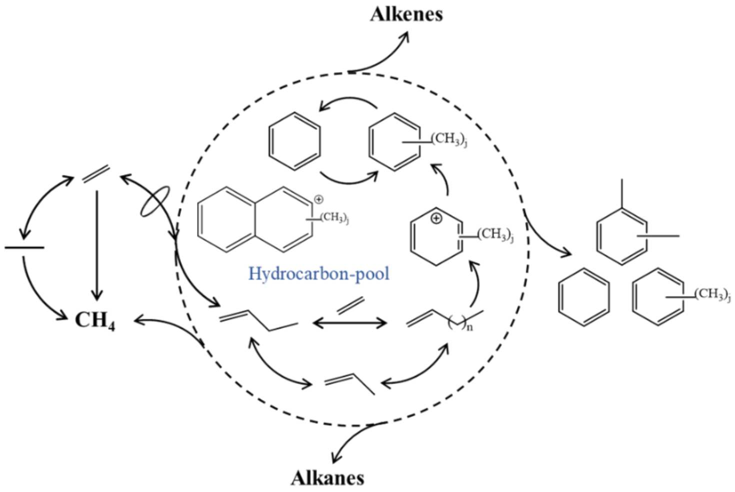

Figure 5.5 Suggested reaction pathways and hydrocarbon-pool mechanism.

The rate constants from the back-transient represent the activity for the formation of products from the "lumped hydrocarbon pool". Oligomerization/cracking, cyclization, alkylation/de-alkylation, and dehydrogenation/hydride transfer could be involved among the hydrocarbon-pool species.

The rate constant and reaction order with respect to ethane for the initial dehydrogenation, or in other words, for the formation of hydrocarbon-pool from ethane, remain to be evaluated. A more precise evaluation of the build-up based on the time-dependent molar balance of the reactor system needs to be developed. Examples of "counting" the surface chemisorbed atoms during the build-up of the chemical transient have been reported by Kruse and coworkers [37,39]. However, with the present catalytic system, such a quantification method needs to be revisited during future work. Once the dynamic changes (with time) of the hydrocarbon species during the build-up are available, the rate constant and reaction order with respect to ethane for building the hydrocarbon-pool can be obtained. Additionally, the qualification of the hydrocarbon-pool species is also vital to the catalytic mechanism, although the reaction transient between ethane/propane aromatization has already provided some hints on this. Further transient studies about the adsorption/desorption of the reactants, products, and intermediates, as well as the chemical/reaction transient of the possible hydrocarbon-pool species, could provide more precise kinetics (eliminate the influence of intracrystalline diffusion) and mechanisms related to the aromatization of light alkanes.

5.5 References

1. Howarth RW, Ingraffea A, Engelder T (2011) Should fracking stop? Nat 477:271-275

2. https://www.eia.gov/dnav/pet/hist/LeafHandler.ashx?n=PET&s=M_EPL2_FPF_NUS_MBBLD&f=M.

3. Xiang Y, Wang H, Cheng J, Matsubu J (2018) Progress and prospects in catalytic ethane aromatization. Catal Sci Technol 8 (6):1500-1516

4. Sattler JJ, Ruiz-Martinez J, Santillan-Jimenez E, Weckhuysen BM (2014) Catalytic dehydrogenation of light alkanes on metals and metal oxides. Chem Rev 114 (20):10613-10653

5. Csicsery SM (1970) Dehydrocyclodimerization: II. Dehydrocyclodimerization of propane and pentane over supported platinum catalyst. J Catal 17 (2):216-218

6. Csicsery SM (1970) Dehydrocyclodimerization: I. Dehydrocyclodimerization of butanes over supported platinum catalysts. J Catal 17 (2):207-215

7. National Academies of Sciences E, and Medicine (2016) The Changing Landscape of Hydrocarbon Feedstocks for Chemical Production: Implications for Catalysis: Proceedings of a Workshop. Washington, DC: The National Academies Press. doi: 10.17226/23555.

8. Hagen A, Roessner F (2000) Ethane to Aromatic Hydrocarbons: Past, Present, Future. Catal Rev 42 (4):403

9. Bragin OV, Shpiro ES, Preobrazhensky AV, Isaev SA, Vasina TV, Dyusenbina BB, Antoshin GV, Minachev KM (1986) The state of platinum in high-silica zeolites and its catalytic activity in ethane and propane aromatization. Appl Catal 27 (2):219-231

10. Steinberg K-H, Mroczek U, Roessner F (1990) Aromatization of ethane on platinum containing ZSM-5 zeolites. Appl Catal 66 (1):37-44

11. Lauritzen AM, Madgavkar AM (2015) Process for the conversion of ethane to aromatic hydrocarbons 11. Google Patents, US20140256536A1

12. Vosmerikova LN, Barbashin YE, Vosmerikov AV (2014) Catalytic aromatization of ethane on zinc-modified zeolites of various framework types. Petrol Chem 54 (6):420-425

13. Mehdad A, Lobo RF (2017) Ethane and ethylene aromatization on zinc-containing zeolites. Catal Sci Technol 7 (16):3562-3572

14. Mehdad A, Gould NS, Xu B, Lobo RF (2018) Effect of steam and CO_2 on ethane activation over Zn-ZSM-5. Catal Sci Technol 8 (1): 358-366

15. Choudhary VR, Kinage AK, Choudhary TV (1997) Effective Low-Temperature Aromatization of Ethane over H-Galloaluminosilicate(MFI) Zeolites in the Presence of Higher Alkanes or Olefins. Angew Chem Int Ed 36 (12):1305-1308

16. Samanta A, Bai X, Robinson B, Chen H, Hu J (2017) Conversion of Light Alkane to Value-Added Chemicals over ZSM-5/Metal Promoted Catalysts. Ind Eng Chem Res 56 (39):11006-11012

17. Ma L, Zou X (2019) Cooperative catalysis of metal and acid functions in Re-HZSM-5 catalysts for ethane dehydroaromatization. Appl Catal B 243:703-710

18. Anunziata OA, Eimer GA, Pierella LB (1999) Ethane conversion into aromatic hydrocarbons over molybdenum-containing MEL zeolites. Appl Catal A 182 (2):267-274

19. Ye J, Bai L, Liu B, Tian H, Hu J, Polo-Garzon F, Mayes RT, Wu Z, Fang Y (2019) Fabrication of a Pillared ZSM-5 Framework for Shape Selectivity of Ethane Dehydroaromatization. Ind Eng Chem Res 58 (17):7094-7106

20. Biscardi JA, Meitzner GD, Iglesia E (1998) Structure and Density of Active Zn Species in Zn/H-ZSM5 Propane Aromatization Catalysts. J Catal 179 (1):192-202

21. Li Z, Lepore AW, Salazar MF, Foo GS, Davison BH, Wu Z, Narula CK (2017) Selective conversion of bio-derived ethanol to renewable BTX over Ga-ZSM-5. Green Chem 19 (18):4344-4352

22. Yu SY, Yu GJ, Li W, Iglesia E (2002) Kinetics and Reaction Pathways for Propane Dehydrogenation and Aromatization on Co/H-ZSM5 and H-ZSM5. J Phys Chem B 106 (18):4714-4720

23. Paál Z (2002) Dehydrocyclization—Heterogeneous. In: Encyclopedia of Catalysis. John Wiley & Sons, Inc. New york

24. Zecevic J, Vanbutsele G, de Jong KP, Martens JA (2015) Nanoscale intimacy in bifunctional catalysts for selective conversion of hydrocarbons. Nat 528 (7581): 245–248

25. Liu H, Wang H, Xing A-H, Cheng J-H (2019) Effect of Al Distribution in MFI Framework Channels on the Catalytic Performance of Ethane and Ethylene Aromatization. J Phys Chem C 123 (25):15637-15647

26. MÉRiaudeau P, Naccache C (1997) Dehydrocyclization of Alkanes Over Zeolite-Supported Metal Catalysts: Monofunctional or Bifunctional Route. Catal Rev 39 (1-2):5-48

27. Biloen P (1983) Transient kinetic methods. J Mol Catal 21 (1):17-24

28. Bennett CO (1999) Experiments and Processes in the Transient Regime for Heterogeneous Catalysis. Adv Catal 44 :329-416

29. Frennet A, Hubert C (2000) Transient kinetics in heterogeneous catalysis by metals. J Mol Catal A-Chem 163 (1-2):163-188

30. Frennet A, Visart de Bocarme T, Bastin JM, Kruse N (2005) Mechanism and kinetics of the catalytic CO-H2 reaction: An approach by chemical transients and surface relaxation spectroscopy. J phys chem B 109 (6):2350-2359

31. Boudart M, Djega-Mariadassou G (1984) Kinetics of Heterogeneous Catalytic Reactions. Princeton University Press, Princeton, NJ

32. Schuurman Y, Kroll VCH, Ferreira-Aparicio P, Mirodatos C (1997) Use of transient kinetics techniques for studying the methane reforming by carbon dioxide. Catal Today 38 (1):129-135

33. Sadykov VA, Gubanova EL, Sazonova NN, Pokrovskaya SA, Chumakova NA, Mezentseva NV, Bobin AS, Gulyaev RV, Ishchenko AV, Krieger TA, Mirodatos C (2011) Dry reforming of methane over Pt/PrCeZrO catalyst: Kinetic and mechanistic features by transient studies and their modeling. Catal Today 171 (1):140-149

34. Matveev AV, Sadovskaya EM, Bryliakova AA, Gorodetskii VV (2016) Isotopic transient kinetic study of CO oxidation on Pd(1 1 0). J Mol Catal A-Chem 420:18-25

35. Pinaeva LG, Sadovskaya EM, Ivanova YA, Kuznetsova TG, Prosvirin IP, Sadykov VA, Schuurman Y, van Veen AC, Mirodatos C (2014) Water gas shift and partial oxidation of CH4 over CeO_2–ZrO_2(–La_2O_3) and Pt/CeO_2–ZrO_2(–La_2O_3): Performance under transient conditions. Chem Eng J 257 :281-291

36. Kruse N, Bundhoo A, Schweicher J, Frennet A (2009) Chemical Transient Kinetics Applied to CO Hydrogenation over a Pure Nickel Catalyst. J Phys Chem C 113 (24):10731-10739

37. Schweicher J, Bundhoo A, Kruse N (2012) Hydrocarbon Chain Lengthening in Catalytic CO Hydrogenation: Evidence for a CO-Insertion Mechanism. J Am Chem Soc 134 (39):16135-16138

38. Melaet G, Ralston WT, Liu W-C, Somorjai GA (2016) Product distribution change in the early stages of carbon monoxide hydrogenation over cobalt magnesium Fischer-Tropsch catalyst. Catal Today 272:69-73

39. Athariboroujeny M, Raub A, Iablokov V, Chenakin S, kovarik L, Kruse N (2019) Competing mechanisms in CO hydrogenation over Co-MnOx catalysts. ACS Catal 9:5603–5612

40. Ralston WT, Melaet G, Saephan T, Somorjai GA (2017) Evidence of Structure Sensitivity in the Fischer-Tropsch Reaction on Model Cobalt Nanoparticles by Time-Resolved Chemical Transient Kinetics. Angew Chem Int Ed 56 (26):7415-7419

41. Schweicher J, Bundhoo A, Frennet A, Kruse N, Daly H, Meunier FdrC (2010) DRIFTS/MS Studies during Chemical Transients and SSITKA of the CO/H2Reaction over Co-MgO Catalysts. J Phys Chem C 114 (5):2248-2255

42. Carvalho A, Ordomsky VV, Luo Y, Marinova M, Muniz AR, Marcilio NR, Khodakov AY (2016) Elucidation of deactivation phenomena in cobalt catalyst for Fischer-Tropsch synthesis using SSITKA. J Catal 344:669-679

43. Frennet A, Lienard G, Crucq A, Degols L (1978) Effect of multiple sites and competition in adsorption on the kinetics of reactions catalyzed by metals. J Catal 53 (1):150-163

44. Sattler A (2018) Hydrogen/Deuterium (H/D) Exchange Catalysis in Alkanes. ACS Catal 8 (3):2296-2312

45. Sattler A, Paccagnini M, Lanci MP, Miseo S, Kliewer CE (2020) Platinum Catalyzed C–H Activation and the Effect of Metal–Support Interactions. ACS Catal 10 (1):710-720

46. Liang T, Toghiani H, Xiang Y (2018) Transient Kinetic Study of Ethane and Ethylene Aromatization over Zinc-Exchanged HZSM-5 Catalyst. Ind Eng Chem Res 57 (45):15301-15309

47. Liang T, Fadaeerayeni S, Shan J, Li T, Wang H, Cheng J, Toghiani H, Xiang Y (2019) Ethane Aromatization over Zn-HZSM-5: Early-Stage Acidity/Performance Relationships and Deactivation Kinetics. Ind Eng Chem Res 58 (38):17699-17708

48. Fadaeerayeni S, Shan J, Sarnello E, Xu H, Wang H, Cheng J, Li T, Toghiani H, Xiang Y (2020) Nickel/gallium modified HZSM-5 for ethane aromatization: Influence of metal function on reactivity and stability. Appl Catal A. 601: 117629

49. Liu X, Liang T, Barbosa R, Chen G, Toghiani H, Xiang Y (2020) Ammoxidation of Ethane to Acetonitrile and Ethylene: Reaction Transient Analysis for the Co/HZSM-5 Catalyst. ACS Omega 5 (3):1669-1678

50. Ruthven DM, Post MFM (2001) Chapter 12 Diffusion in zeolite molecular sieves. Stud Surf Sci Catal 137:525-577

51. Chen G, Liu H, Fadaeerayeni S, Shan J, Xing A, cheng j, Wang H, Xiang Y (2020) Tuning the Reactivity of Ethylene Oligomerization by HZSM-5 Framework Alf Proximity. Catal Sci Technol. 10: 4019-4029

52. Kwak BS, Sachtler WMH (1996) Aromatization of propane over Zn/HZSM-5 catalysts prepared by chemical vapor deposition. Korean J Chem Eng 13 (4):356-363

53. Rodrigues VdO, Vasconcellos Jr FJ, Faro Júnior AdC (2016) Mechanistic studies through H–D exchange reactions: Propane aromatization in HZSM5 and Ga/HZSM5 catalysts. J Catal 344:252-262

54. Xiao H, Zhang J, Wang P, Zhang Z, Zhang Q, Xie H, Yang G, Han Y, Tan Y (2015) Mechanistic insight to acidity effects of Ga/HZSM-5 on its activity for propane aromatization. Rsc Adv 5 (112):92222-92233

55. Giannetto G, Montes A, Gnep NS, Florentino A, Cartraud P, Guisnet M (1994) Conversion of Light Alkanes into Aromatic Hydrocarbons .VII. Aromatization of Propane on Gallosilicates: Effect of Calcination in Dry Air. J Catal 145 (1):86-95

56. Lukyanov DB, Gnep NS, Guisnet MR (1994) Kinetic modeling of ethene and propene aromatization over HZSM-5 and GaHZSM-5. Ind Eng Chem Res 33 (2):223-234